Tomography of the ionosphere

Tomography of the ionosphere

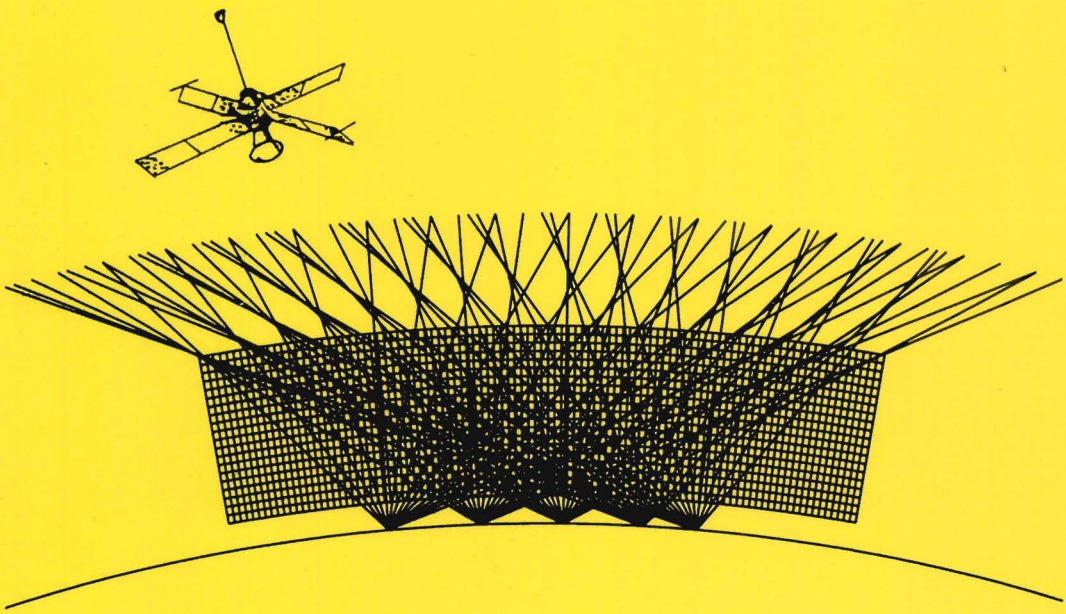

Gijs Fehmers

Tomography of the ionosphere

PROEFSCHRIFT

ter verkrijging van de graad van doctor aan de Technische Universiteit Eindhoven, op gezag van Rector Magnificus, prof. dr. M. Rem, voor een commissie aangewezen door het College van Dekanen in het openbaar te verdedigen op maandag 16 september 1996 om 16.00 uur

door

Gijsbert Christiaan Fehmers

geboren te Amsterdam

Dit proefschrift is goedgekeurd
door de promotoren
prof. dr. F.W. Sluijter
en
prof. dr. D.C. Schram

Copromotor is
dr. T.A.Th. Spoelstra

Druk: Universiteitsdrukkerij, T.U. Eindhoven

Tomography of the ionosphere
by Gijsbert Christiaan Fehmers
Thesis Technische Universiteit Eindhoven
with a summary in Dutch and English
ISBN 90-386-0438-6

Af en toe de vraag
schoon we haar graag vermijden
waartoe wij toch gestaag
ons vluchtig leven leiden.

In de ionosfeer
ligt een antwoord niet besloten
maar 't helpt om telkens weer
je blikveld te vergroten.

In de herinnering
aan mijn lieve ouders

Gijs Fehmers
Blauwkapelseweg 107
3572 KD Utrecht

Faculteit der Toegapaste Natuurkunde
Technische Universiteit Eindhoven
Postbus 513
5600 MB Eindhoven
The Netherlands

The work described in this thesis was carried out at the Physics Department of the Eindhoven University of Technology. It was financially supported by the Netherlands Foundation for Scientific Research (NWO - Nederlandse Organisatie voor Wetenschappelijk Onderzoek).

Contents

Samenvatting

Door de zwaartekracht van de aarde heeft onze atmosfeer een gelaagde structuur. Met wat goede wil is het mogelijk om afzonderlijke lagen te onderscheiden. De ionosfeer is gedefinieerd als die laag, waar de voortplanting van radiogolven merkbaar wordt beïnvloed door vrije elektronen en ionen. Deze laag strekt zich uit van ongeveer 80 tot 1000 km hoogte. De invloed van de ionosfeer op de voortplanting van radiogolven verklaart het belang van deze laag en van het onderzoek ernaar. De ionosfeer kan het radioverkeer zowel van nut als tot last zijn. Aan de ene kant fungeert zij als een soort spiegel voor radiostralen op de kortegolf (golflengte tussen 10 en 100 meter) en maakt zo een radioverbinding mogelijk tussen twee punten op aarde die zich onder elkaars horizon bevinden. Aan de andere kant bemoeilijkt de ionosfeer het radiocontact tussen de aarde en objecten buiten de dampkring. Als de ionosfeer door verstoringen haar nette gelaagde structuur verliest, leidt dit tot een verslechterde ontvangst bij beide typen radioverbindingen. Van de meeste verstoringen is het gedrag maar matig begrepen. Veel onderzoek is dan ook gericht op een beter begrip van deze verstoringen. Zulk onderzoek is gebaseerd, of wordt uiteindelijk getoetst, aan waarnemingen. Tomografie van de ionosfeer is een methode om zulke waarnemingen te verwerken en heeft tot doel om tweedimensionale doorsneden te maken van de elektronendichtheid van de ionosfeer.

In het algemeen is tomografie een techniek om een ruimtelijke verdeling te reconstrueren aan de hand van haar lijnintegralen, of projecties, zo men wil. In de ionosfeer worden de lijnintegralen gemeten met behulp van de zogenaamde differentiële-Dopplertechniek. Met deze techniek meet men de lijnintegraal van de elektronendichtheid langs een gezichtslijn (eigenlijk fasepad) van een radiozender aan boord van een satelliet naar een ontvanger op aarde. De satellieten van het Amerikaanse *Navy Navigation Satellite System* lenen zich zeer goed voor deze metingen. Deze satellieten bewegen in een polaire baan. Om de metingen voor tomografie te kunnen gebruiken, worden een aantal ontvangers geplaatst langs een lengtegraad, opdat ze ongeveer in een vlak liggen met een passerende satelliet. De gezichtslijnen tussen satelliet en ontvanger liggen ook in dit vlak en zo wordt dit het vlak van doorsnede (zie figuur op de omslag).

Hoofdstuk 1 van het proefschrift bevat een beknopte inleiding tot de ionosfeer. Het geeft ook een kort overzicht van de belangrijkste methoden om de elektronendichtheid in de ionosfeer te meten. Hoofdstuk 2 is geheel aan bovengenoemde differentiële-Dopplertechniek gewijd, en beschrijft haar principe, geschiedenis, theorie en toepassingen. Het geeft ook de karakteristieken van de apparatuur waarmee de metingen voor dit proefschrift zijn gedaan. Hoofdstuk 3 gaat uitvoerig in op inverse problemen, een klasse problemen waarvan tomografie deel uitmaakt. Een veel voorkomend kenmerk van inverse problemen is de extreme gevoeligheid van hun oplossing voor kleine veranderingen in de metingen. Deze instabiliteit kan worden gezien als een gevolg van de poging een reconstructie te maken op basis van onvolledige

informatie.

De toepassing van tomografie in ionosfeer-onderzoek komt aan de orde in hoofdstuk 4. Hier gebruiken we de verworvenheden van hoofdstuk 3 en stuiten we inderdaad op het probleem van de instabiliteit. Deze is het gevolg van het ontbreken van horizontale gezichtslijnen, of lijnintegralen, zoals te zien in de figuur op de omslag. Een verzameling van zulke lijnintegralen zou informatie over het profiel van de elektronendichtheid als functie van de hoogte bevatten. Het ontbreken hiervan maakt het inverse probleem slecht gesteld. Er zit namelijk niet genoeg informatie in de metingen om een natuurgetrouwe reconstructie te maken: de verticale structuur zal niet volledig gereconstrueerd kunnen worden. Nadat ook wat andere problemen van de ionosferische toepassing van tomografie de revue hebben gepasseerd, bespreken we enige bestaande algoritmen die de metingen omzetten naar een doorsnede van de elektronendichtheid. Door gebruik te maken van ionosfeer-modellen, compenseren deze algoritmen het gebrek aan informatie over de verticale structuur. Voor veel toepassingen is dit niet bezwaarlijk. Maar als we de reconstructies willen gebruiken om het gedrag van de ionosfeer beter te begrijpen en betere modellen te maken, is het niet zo verstandig om deze te baseren op bestaande modellen.

Om deze patstelling te doorbreken, wordt aan het eind van hoofdstuk 4 een nieuw algoritme gepresenteerd dat slechts minimaal gebruik maakt van modellen. Tests tonen aan dat het algoritme onder realistische omstandigheden in staat is een gedeelte van de oorspronkelijke verticale structuur te reconstrueren. Zo bepaalt het de hoogte van de laag van maximale elektronendichtheid met een nauwkeurigheid van 90 km. Dit algoritme is zo algemeen geformuleerd dat het ook toepassing heeft gevonden buiten de ionosfeer, zoals in de tomografie van tokamak plasma's. Hoofdstuk 5 behandelt de wiskundige finesses van het algoritme.

Hoofdstuk 6 beschrijft het experiment waarvoor we in het voorjaar van 1995 vijf ontvangers hebben opgesteld langs de lijn van Harlingen naar Marseille. Het blijkt dat de maximale elektronendichtheid boven Nederland, zoals die volgt uit tomografie, in goede overeenstemming is met onafhankelijke metingen van de Koninklijke Landmacht. Interessanter is de dagelijkse variatie die we ontwaren in de hoogte van de laag van maximale elektronendichtheid. Deze variatie is in overeenstemming met de theorie. Dat zij zichtbaar is, bewijst dat tomografie inderdaad uitspraken kan doen over de verticale structuur, ondanks het probleem van de ontbrekende horizontale lijnintegralen. Tenslotte bespreken we enige verstoringen van de gelaagde structuur van de ionosfeer. Deze zijn de ionosferische trog, de zogenaamde *medium scale travelling ionospheric disturbances* en (nachtelijke) verstoringen die niet in een bestaande categorie vallen.

De eerste helft van het proefschrift, tot en met de tweede paragraaf van hoofdstuk 4, beschrijft de stand van zaken voorafgaand aan dit onderzoek. Uitgezonderd het werk aan de ontvangers en enige nieuwe invalshoeken, draagt dit gedeelte dus niet bij aan de Vooruitgang. De rest van het proefschrift bevat oorspronkelijk en nieuw werk.

Dit proefschrift is zo geschreven dat het leesbaar zou moeten zijn voor gevorderde studenten in de natuurkunde. Sommige gedeelten, en dan met name hoofdstuk 1 en deze samenvatting, zijn ook voor een breder publiek bedoeld.

Summary

Due to the earth's gravity, our atmosphere is stratified. Without much simplification, one can discern distinct layers. The ionosphere is defined as the layer where the propagation of radio waves is noticeably affected by electrons and ions. The ionosphere extends roughly from 80 to 1000 kilometers altitude. Its influence on radio wave propagation explains the layer's importance and research interest. The ionosphere is both a blessing and a nuisance to radio communication. On the one hand, the layer can act as a mirror to radio rays, facilitating a short wave (10-100 meters wavelength) radio contact over the horizon. On the other hand, it troubles radio links between the earth and extraterrestrial objects. When disturbances disrupt the ionosphere's stratified structure, both types of radio links are affected. Yet, the understanding of the behaviour of most kinds of disturbances is not very advanced. Therefore, a great part of the research effort focusses on these irregularities. Such research is based upon, or will eventually be tested against, observations. Tomography of the ionosphere is a method to process these observations; it aims to produce twodimensional cross-sections of the ionosphere's electron density.

In a general way, tomography is the technique to reconstruct a spatial distribution from its line integrals, or, if you like, projections. In the ionosphere, these line integrals are measured by the so-called differential Doppler technique. By this technique, one can determine the line integral of electron density along a line of sight (phase path, in fact) from a radio transmitter carried by a satellite to a receiver on earth. The satellites of the U.S. *Navy Navigation Satellite System* are very well suited to this kind of measurement. These spacecrafts move in polar orbits. To make these measurements fit for tomography, the receivers should be placed along a meridian, so as to lie in the same plane as the passing satellite. As the lines of sight lie in the same surface, it forms the cross-section's plane (see cover illustration).

Chapter 1 of the thesis contains a concise introduction to the ionosphere. In addition, it gives a short review of the most important methods to measure ionospheric electron density. Chapter 2 is dedicated to the differential Doppler technique and describes its history, its theory, and its applications. The chapter concludes with the characteristics of the equipment used for this research. Chapter 3 dwells upon inverse problems, a class of problems tomography is part of. An frequent feature of inverse problems is their extreme sensitivity to small variations in the data. This instability can be seen as a consequence of the attempt to make a reconstruction based on incomplete information.

The application of tomography to ionospheric research is discussed in chapter 4. Here, we will make good use of the results of chapter 3 and we will indeed encounter the instability problem. This problem results from the lack of horizontal line integrals, or dito lines of sight, as the cover illustration shows. A set of such line integrals would contain information on the vertical profile of the ionosphere's electron density. Its absence makes that the inverse problem

is ill-posed. There is not enough information in the data to make a reliable reconstruction: the vertical structure will not be recovered completely. After some other problems of tomograpy's ionospheric application have been passed in review, we will discuss some existing algorithms that transform the measurements to cross-sections of electron density. By the inclusion of model ionospheres, these algorithms compensate for the missing information on the vertical structure. In many applications, this is perfectly sound. If, by contrast, the reconstructions are used to enhance our understanding of the ionosphere or to develop better models, it is not advisable to start with existing models in the first place.

To break out of this deadlock, a new algorithm is presented at the end of chapter 4. This algorithm uses a minimum of model information. Tests under realistic conditions demonstrate that this algorithm can partially reconstruct the original vertical structure. The height of the layer of maximum electron density, for instance, is estimated to within an accuracy of 90 km. This algorithm is formulated in such general terms that it has found an application beyond the ionosphere: the tomography of tokamak plasmas. Chapter 5 tackles the mathematical subtleties of the algorithm.

Chapter 6 describes the experiment, for which five receivers were installed along a line from Harlingen to Marseille. It turns out that the maximum electron density over the Netherlands, as determined by tomography, agrees well with independent soundings by the Royal Netherlands Army. More interesting is the appearance of a daily variation in the height of maximum electron density. This variation is consistent with theory. The discernibility of the variation proofs the claim that tomography can indeed pronounce upon the vertical structure, despite the problem of the missing horizontal line integrals. In the final sections, we discuss examples of disturbed stratified structure. These are the ionospheric trough, the *medium scale travelling ionospheric disturbances* and (nocturnal) disturbances that do not fall in any existing category.

The first half of this thesis, up to the second section of chapter 4, describes the state of affairs at the outset of this research. Therefore, this part does not contribute to Progress, with the exception of the work on the receivers and some new viewpoints. The remainder contains original and novel work.

This thesis is written at such a level that advanced physics students should not encounter too many difficulties. Some parts, particularly chapter 1 and this summary, are intended for a broader audience.

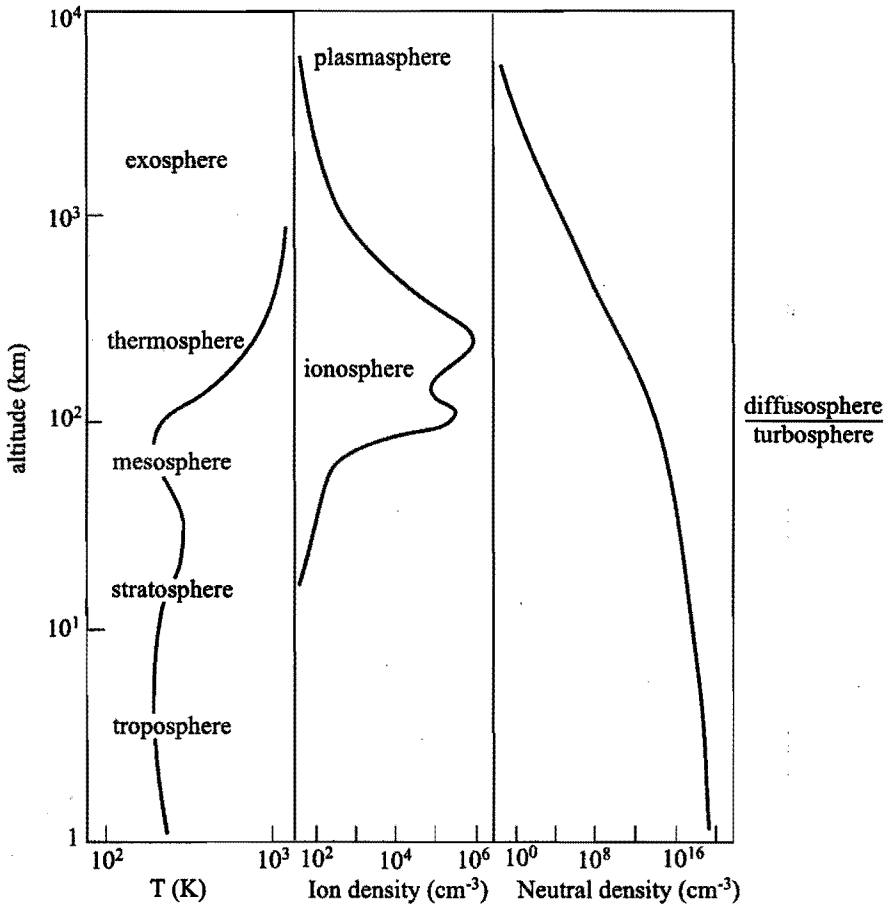

Figure 1.1: Schematic representation of the thermal structure, the ion density and the neutral density of the earth's atmosphere. The approximate altitude regimes of various named regions are indicated. From Rees 1989.

Chapter 1

The ionosphere

This chapter contains a concise introduction to the ionosphere and justifies it as an object of research. It continues with a review of the most important techniques to measure ionospheric electron density. It culminates in tomography.

1.1 The atmospheric layers

Due to the gravity of the earth, our atmosphere is stratified. As we all know, atmospheric density decreases with height and this vertical gradient is much larger than the horizontal gradient. Without much simplification, one can discern distinct layers. The best-known criterion for such discrimination is the temperature. This defines the troposphere, stratosphere, mesosphere and thermosphere, where the temperature alternately decreases or increases with altitude (see figure 1.1). The transition zone between two spheres is called a pause. A pause adopts its prefix from the lower sphere. The tropopause, for instance, separates the troposphere and stratosphere.

Another discriminating criterion is based on the process that dictates atmospheric composition. In the lower 100 kilometers, the atmospheric gases are well mixed and composition is homogeneous. Turbulence is the process that mixes the air. Hence the name turbosphere. At greater heights, in the diffusosphere, diffusion is stronger than turbulence. Here, every particle has its own distribution, which explains why the lightest particles dominate at the highest altitudes.

Yet another criterion is based on the extent to which electrons, ions and the magnetic field determine the atmosphere's physical behaviour. The ionosphere is defined as the part of the atmosphere where the propagation of radio waves is noticeably affected by electrons and ions. These charged particles make the index of refraction for radio waves differ from unity. Electrons and singly ionized positive ions are by far the most abundant and important charged particles. They are created from the atmospheric gases by photoionozation by extreme ultraviolet radiation. The sun is the source of the ionizing radiation. An additional minor process is ionization by energetic particles, either from the solar wind or from cosmic sources, the cosmic rays. The temperature rise in the thermosphere (figure 1.1) is caused by the excess energy of the ionizing photons, which is released as kinetic energy of the liberated electrons. The same mechanism explains stratospheric heating, the other temperature surge in figure 1.1. Here, solar UV photons dissociate ozone and their excess energy is converted into kinetic energy of the resulting molecular and atomic oxygen.

The ionosphere extends roughly from 80 to 1000 kilometers altitude. At a height of about 300 km, electron density reaches its maximum. At this peak, only a tiny fraction ($< 0.1\%$) of the particles is ionized. Above the peak, neutral density decreases faster than electron density (see figure 1.1), thus the degree of ionization increases with height.

Above the ionosphere extends the plasmasphere, where the degree of ionization approaches unity. In the plasmasphere, hydrogen is the most abundant element. For this reason, the plasmasphere is also called the protonosphere. The upper boundary of the plasmasphere follows the geomagnetic field lines. In quiet magnetic conditions, this plasmapause occurs at an altitude of about 6 earth radii above the equator. The neutral atmosphere at plasmaspheric heights is often referred to as the exosphere. Here, the density is so low that the mean free path of a particle is longer than its ballistic height gain. When a neutral particle's velocity is larger than the escape velocity, it may escape from the exosphere and thereby from the atmosphere. While the exosphere is the outermost layer of the neutral atmosphere, the earth's influence on charged particles continues beyond the plasmasphere. Here lies the magnetosphere, where the earth's magnetic field determines the trajectory of a charged particle. The magnetosphere is not spherical. Instead, it is elongated and more or less blown away from the earth by the magnetic field carried by the solar wind. Above the magnetosphere, the earth has run out of means to retain a particle. Here, our atmosphere is no more. Interplanetary space begins and the sun rules.

1.2 Importance of the ionosphere

At great heights, the air is thin: only about one millionth of all atmospheric particles is located above 100 km altitude. Of these, only a small fraction is ionized. Still, the ionosphere is of some importance to mankind. When I tell about my work, people always ask what motivates ionospheric research. My personal motivation is curiosity. To the general public, the following arguments may sound more convincing.

1.2.1 Protection

The first and foremost result of the presence of the ionosphere, or rather the upper atmosphere, is the protection of life on earth from the dangerous ionizing radiation from the sun and the rest of the universe. The radiation is absorbed by the process of photoionozation. This pertains to the high energy end of the solar spectrum, from roughly hydrogen's Lyman-α line, at a wavelength of $\lambda = 122$ nm, to shorter wavelengths. Outside the earth's atmosphere, the flux in this part of the solar spectrum is about 8 mW m^{-2}, on a total bolometric flux of 1.4 kW m^{-2}. The high energy end of the solar spectrum strongly varies and the more so in periods of high solar activity. It is interesting to compare the ionosphere's protective working to that of the stratospheric ozone layer. O_2 and especially O_3 absorb solar radiation in the range from Lyman-α to $\lambda \approx 300$ nm, by the process of photodissociation. One might therefore state that the ionosphere is equally important to life on earth as the ozone layer. This is only partially true, however, because the total power absorbed in the ozone layer is a few hundred times larger than the power absorbed in the ionosphere. More reassuring in this respect is the fact that we will never see the appearance of a hole in the ionosphere, because the outermost part of the atmosphere is always ionized. Therefore, the ionosphere can only

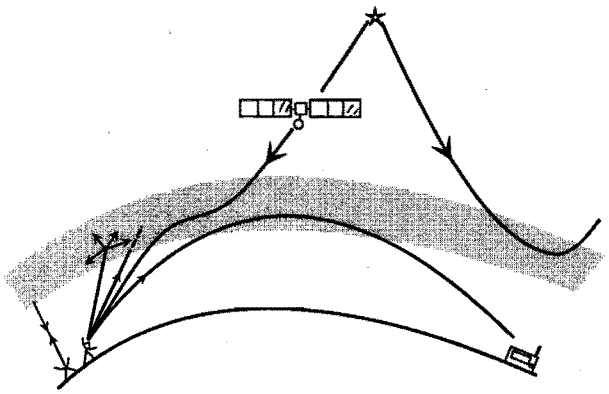

Figure 1.2: Schematic picture of the ionosphere's influence on radio propagation. From left to right: reflection, scattering, absorption, refraction, and reflection by refractive bending (twice).

disappear when the whole atmosphere vanishes. Although of vital importance, it is obvious that the protective aspect of the ionosphere does not generate much enthousiasm for research.

1.2.2 Radio propagation

There is more room for ionospheric research at the other end of the electromagnetic spectrum: the ionosphere affects radio propagation. This can either be a blessing or a nuisance, depending on the type of radio connection we want to make. Radio propagation and the index of refraction are subjected to a detailed study in chapter 2. Here, we focus on the main consequences of altered radio propagation. See figure 1.2 for the general picture.

Nuisance

When we want to establish a radio link between two points on either side of the ionosphere, the ionosphere is a nuisance. All kinds of earth-satellite connections are hindered by the ionosphere. Scintillation causes noise in transionospheric communication links. Refraction limits the accuracy of satellite based navigation systems; if not corrected for ionospheric refraction, positions determined with the help of the Navy Navigation Satellite System, may be 300 meters off. Ionospheric refraction also troubles radio astronomers (Spoelstra and Kelder 1984). If not corrected for ionospheric effects, the error in the position of a point source is in the order of a minute of arc (Erickson 1984). Another effect that hinders radio astronomers is the fact that the ionosphere reflects radiowaves at frequencies below the plasmafrequency (section 2.3). This makes the ionosphere effectively opaque at frequencies below ~ 30 MHz.

Blessing

When, by contrast, we want a radio connection between two points on the same side of the ionosphere, the ionosphere is a blessing. The reflective properties of the ionosphere at

frequencies below 10 MHz, permit radio connection between a transmitter and a receiver that cannot see each other directly. From figure 1.2, it follows that the over the horizon connection is actually established by reflection by refractive bending. This is the principle of short wave communication, at frequencies between 2 and 20 MHz (wavelength between 15 and 150 meters, which, today, would not be called short waves). Short wave transmissions by Radio Moscow, for instance, give the Kremlin the opportunity to convince people all over the world of its political opinions, even if those people are far below Moscow's horizon.

The choice of the right frequency in short wave broadcasts is quite delicate. First, there is the risk of multipath propagation. Radio waves may travel different routes from transmitter to receiver: the ground (direct) path, via one reflection at the F layer, or via multiple reflections at the E and F layers (see next section for nomenclature). At the receiver these waves interfere, which deteriorates reception. This phenomenon is frequency dependent, although it depends on the circumstances whether a frequency-increase or rather a decrease would improve communication. There are two other competing effects that affect the choice of the frequency channel: reflection and absorption. When electron density is low, during the night, the ionospheric plasma frequency drops and waves that would be reflected during daytime are not reflected. Use of lower frequencies reduces this risk.

At low frequencies, however, absorption in the lower ionospheric layers may become important (see section 2.3). Absorption is caused by collisions of charged particles that oscillate along with the passing electromagnetic wave. When these particles collide with neutral particles, the energy of the radiation is dissipated. Where charged particles exist in the relatively dense environment of the lower ionosphere (D-layer), collisions are frequent and absorption is strong. After sunset, the D-layer disappears and absorption decreases. This explains why medium wave radio transmissions can be received at much greater distances at night than during the day.

1.2.3 Objects of research

A glance at broadcasting tables of short wave stations, shows that they transmit at high frequencies during daytime and at low frequencies during the night. This is explained by the combined effects of reflection and absorption. It is clear that good ionospheric models can help planners to improve the broadcasting schedules. The creation of such models for the unperturbed ionosphere is one of the objects of ionospheric research. The models would also be very useful to astronomers, geodesists, and, sorry to say, the military. The army uses the ionosphere to communicate and to spy on the enemy via remote sensing, such as the 'over the horizon radar'.

Another object of ionospheric research, and at least as important, is the study of irregularities. Radio propagation can be severely affected by these deviations from stratification. The irregularities are not as well understood as the unperturbed ionosphere. Among the irregularities, we mention scintillation and Travelling Ionospheric Disturbances, or TIDs.

The research at the Technische Universiteit Eindhoven is aimed at a better understanding of the TID phenomenon and especially the medium scale TID, or MSTID (PhD theses by Miessen 1990 and Van Velthoven 1990). An understanding of TIDs starts with good observations. Images of their spatial structure are particularly welcome. Tomography of the ionosphere is a cheap technique to make such pictures. This thesis must be seen as part of the effort to better observe and understand ionospheric disturbances. Before we focus on tomography, we discuss the ionosphere in some detail in the next section.

Now is the time to put ionospheric research in perspective relativization. In 1901, Marconi transmitted a radio signal over the Atlantic. This feat could not be explained by diffraction of electromagnetic waves by the earth's surface, the so-called ground waves. This lead to Heaviside's conjecture of a conductive layer in the upper atmosphere, which came to be known as the ionosphere. Interest in the ionosphere grew and research reached its apex in the second world war. Throughout the cold war, military interest remained but civil research declined. Two trends explain this decline. First, short wave communication is losing ground to satellite links. Second, satellite transmissions are shifted to ever higher frequencies, where ionospheric refraction is less important. Today, the cold war being over, military funding is decreasing as well.

1.3 Ionospheric facts and figures

To fully appreciate the present study, a basic knowledge of the ionosphere is needed. This section presents the facts and the jargon that will be encountered later. For a more comprehensive introduction there exists a wide range of books, such as Ratcliffe 1972, Giraud and Petit 1978 and Hargreaves 1979.

1.3.1 The stratified ionosphere

It is clear form the definition of the ionosphere that the electron density, N_e, is the most important quantity. Because practically all ions in the ionosphere are singly ionized and because the ionosphere is essentially neutral everywhere (in the conducting ionosphere, currents quickly cancel charge separation), the electron density equals the ion density. Electron density varies with place and time. Because the ionosphere is stratified, the variation of electron density is stronger in the vertical direction than it is in the horizontal direction. The ionospheric electron density as a function of height is called the ionosphere's vertical profile. Because electron density is negligible at low and high altitudes, the profile has at least one maximum somewhere. Such a maximum is $N_{e,\max}$ and it is reached at a certain height $H_{\max}$. Integration of the vertical profile gives the electron column density. In the jargon, the electron column density is called (vertical) Total Electron Content, or (vertical) TEC. Its dimension is number of electrons per square meter. There is a distinction between vertical TEC and slant TEC. Slant TEC is defined as the electron column density along an (oblique) line of sight, and slant TEC equals vertical TEC only if the line of sight goes through the zenith. In this thesis, slant TEC is understood where TEC is written. An artificial measure of the ionosphere's thickness is the slab thickness τ. It is defined as $\tau = \mathrm{TEC}/N_{e,\max}$. If the ionosphere were a layer of uniform electron density, the slab thickness would equal this layer's thickness. The mean ionospheric height h_i is the height where the electron content is divided into two equal parts. In the same uniform ionosphere, h_i is the height of the middle of the layer.

The Chapman layer

As a rough guide to ionospheric modelling and understanding, the Chapman model has proved of invaluable importance. The Chapman model estimates the rate of electron production as a function of height. It is based on the following assumptions:

1. The degree of ionization is low.

2. The only ionization process is photoionization by monochromatic radiation of obliquity χ, which means that the source of the radiation (the sun) has zenith angle χ.

3. The neutral atmosphere has only one constituent particle. Its effective photoionozation cross section at the considered wavelength is σ.

4. The atmosphere is stratified and the temperature does not vary with height. In this approximation, the (neutral) density is given by the isothermal barometric equation:

$$N = N(h) = N(0)e^{-h/H_{\text{scale}}} . \tag{1.1}$$

Here $N(h)$ is the density at height h. H_{scale} is the scale height, given by $H_{\text{scale}} = kT/mg$. T is the temperature in Kelvin, k is Boltzman's constant, m is the mean mass of the particles (though there's only one species now) and g is the gravitational acceleration.

After some algebra, these assumptions lead to an ionization rate q:

$$q(h) = q_{\text{max}} \exp\left\{1 - z - \sec\chi\, e^{-z}\right\} , \tag{1.2}$$

where we understand

$$q_{\text{max}} = \frac{\Phi \cos\chi}{eH_{\text{scale}}} , \quad H_{\text{max}}^{\chi=0} = H_{\text{scale}} \ln(\sigma N(0) H_{\text{scale}}) , \quad z = \frac{h - H_{\text{max}}^{\chi=0}}{H_{\text{scale}}} . \tag{1.3}$$

Φ is the incoming flux in photons per second per square meter, $e = 2.718..$ and q_{max} is the maximum ionization rate. The height where this maximum occurs, follows after differentiation of (1.2): $h = H_{\text{max}}^{\chi=0} + H_{\text{scale}} \ln(\sec\chi)$. $H_{\text{max}}^{\chi=0}$ is the height of maximum ionization rate when $\chi = 0°$, i.e. when the sun is in the zenith. The dimensionless variable z is called the reduced height. In the left half of figure 1.3, we see profiles of Chapman model ionization rate for different values of χ. Although the peaks of these curves are shifted in place and value, the curves have the same form. When we take atomic oxygen as the constituent species, assume a thermospheric temperature of $T = 800\ K$ and fill in the numbers, we get $H_{\text{scale}} = 41$ km and $H_{\text{max}}^{\chi=0} = 175$ km. These results must be treated with caution, because assumption 3. and 4. in Chapman theory are not very realistic.

We now have a model of electron production. Only after the inclusion of a model of electron loss, we obtain a model of electron density. And electron density is what we are really interested in. Free electrons disappear via two processes, attachment or recombination. Electron attachment, where an electron and a neutral particle form a negative ion, is unimportant. Recombination comes in two flavours, radiative and dissociative recombination. In the first reaction, energy and momentum are conserved by emission of a photon:

$$\mathrm{e^- + X^+ \rightarrow X + \gamma} \quad \text{(radiative recombination)}$$

In the second, the conservation laws are satisfied by the different directions and velocities of the separated atoms:

$$\mathrm{e^- + XY^+ \rightarrow X + Y} \quad \text{(dissociative recombination)}$$

The rate of either reaction scales with the product of ion and electron density. Because these densities are equal, total loss rate goes with N_e^2. Dissociative recombination goes much faster than radiative recombination, because the conservation laws are much easier satisfied in the

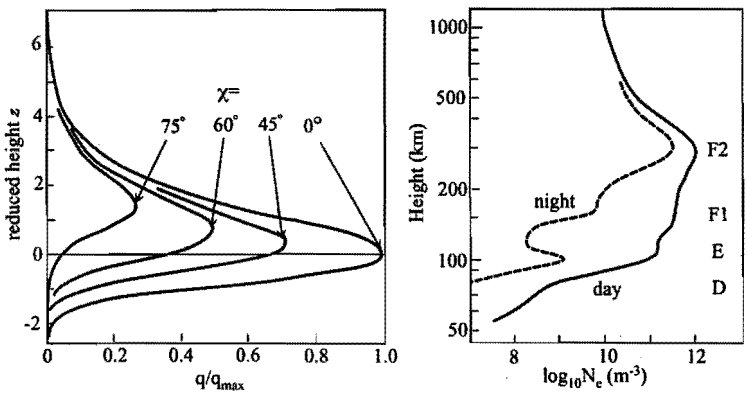

Figure 1.3: Left half (from Ratcliffe 1972): profile from Chapman model of ionization rate. Right half (from Davies 1990): Schematic profiles of the day- and nighttime ionosphere. The approximate heights of the D, E, F_1 and F_2 layers are indicated.

former. In the lower ionosphere, most ions are composite and (dissociative) recombination is a rapid process. In the upper ionosphere, where O^+ dominates, recombination is much slower. After atom-ion transfer or charge-exchange, where the ion reacts with a neutral particle to form a composite ion, dissociative recombination prevails even in the upper ionosphere. Although this enhances loss rates in this region, recombination remains slow, because neutral particle concentration decreases with altitude.

Although atom-ion transfer and charge-exchange partly invalidate the assumption, we may assume that the recombination rate scales with the square of the electron density. Equilibrium requires that recombination equals production. This gives $q = \alpha N_e^2$, where α is the recombination rate. From equation (1.2), we obtain

$$N_e(h) = \sqrt{\frac{q_{\max}}{\alpha}} \exp \frac{1}{2} \{1 - z - \sec\chi \; e^{-z}\} \; . \tag{1.4}$$

This model is known as the Chapman α layer. It follows that the height of maximum electron density should coincide with the height of maximum electron production. In reality, the layer of maximum electron density lies significantly higher: rather 275 km than the 175 km mentioned above. This is the result of transport, and mainly that of diffusion.

Whatever its shortcomings may be, the Chapman model is very useful when $N_{e,\max}$, $H_{\max}$ and H_{scale} are used as adjustable parameters. For the model tests in section 4.4, we use the following model Chapman layer:

$$N_e(h) = N_{e,\max} \exp \frac{1}{2} \{1 - z - e^{-z}\} \; , \tag{1.5}$$

Real layers

The right part of figure 1.3, shows profiles that are more realistic than the Chapman layer. When we interpret them, we must realize that they remain idealizations. We see a marked

layer	altitude	radiation at	ionizes
D	<90 km	Ly-α	NO
		X-rays, cosmic rays	
E	90-130 km	$\lambda < 14$ nm,	N_2,
		$80 < \lambda < 102.7$ nm	O_2, O
F_1	130-200 km	$14 < \lambda < 80$ nm	O, N_2
F_2	>200 km	$14 < \lambda < 80$ nm	O, N_2

Table 1.1: Classification of ionospheric layers. (Ly-α is at $\lambda = 121.6$ nm. The ionization threshold of O_2 is at $\lambda = 102.7$ nm and on longer wavelengths the major atmospheric gases cannot be ionized.)

difference between the day- and nighttime ionosphere. No wonder, because electron density and ionospheric morphology strongly depend on the solar ionizing flux. This explains why the electron density varies with latitude, with the daily cycle, with the seasons and with the solar cycle. In figure 1.3, the individual ionospheric layers are indicated by capitals. Their main characteristics are summarized in table 1.1. The D-layer disappears immediately after sunset. The peak in ionization rate occurs in the F_1-layer, or ledge. It also disappears after sunset. The overall peak in electron density is located in the F_2-layer; at around 300 km altitude it reaches $N_e \approx 10^6 \text{cm}^{-3}$. At this altitude, atomic oxygen O is the most abundant particle, and O^+ the most abundant ion.

1.3.2 Deviation from stratification

So far we have discussed the stratified ionosphere, now we come to deviations from stratification. There exist two important deviations from stratification that occur daily and cannot be called irregularities. These are the so-called trough and the equatorial anomaly. The trough is a nighttime depletion of the ionosphere around geomagnetic latitude 60^o (north and south), over a latitudinal extent of around 5^o. The equatorial anomaly is an electron density enhancement around 20^o geomagnetic latitude, that peaks in the evening. It is caused by the so-called fountain at the magnetic equator. Here, the combined effect of magnetic and electric fields (the $E \times B$ drift) thrusts free charges upwards. On either side of the magnetic equator, the free charges fall downwards along the magnetic field lines to fill the anomaly.

Among the deviations from stratification that can really be called irregularities and that profoundly affect radio propagation, we mention the Travelling Ionospheric Disturbances and the small scale irregularities that cause scintillation. Scintillation is an observational phenomenon, defined as a rapid variation in phase or amplitude (and also in polarization and angle of arrival) in the reception of radio waves. It can be especially severe in tropical regions during the evening and in the auroral regions. Scintillation is caused by scattering on irregularities in electron density with sizes between a few meters and a few kilometers.

The Travelling Ionospheric Disturbance, or TID, is a propagating oscillation in electron density. A TID is usually associated with a density oscillation in the background neutral atmosphere, a so-called acoustic-gravity wave. The TID is therefore a tracer of such a wave.

TIDs can be classified into three classes (Georges 1968): large scale (phase speed: 300-1000 m/s, period 30 min-3 hr), medium scale (phase speed: 100-300 m/s, period 12 min-1 hr) and small scale (period of several minutes and wavelength of tens of kilometers).

The large scale TIDs are thought to originate in the auroral oval, from which they are supposed to propagate equatorwards. (The auroral oval is the region more or less in the vicinity of the polar circles where the northern and southern lights (aurora) can be seen.) There is much speculation on the excitation mechanisms of medium and small scale TIDs, but little is certain.

1.4 Observational techniques, imaging and tomography

As we have seen, (free) electron density N_e is the most important quantity of the ionosphere, both for theoretical understanding and for practical applications. It is also a quantity that changes with time and position. This section discusses methods to measure ionospheric electron density.

1.4.1 Observational methods

Basically, there are two approaches to measure ionospheric electron density: either by local (in situ) measurements or by remote sensing. Local measurements require probes being sent into the ionosphere. These can be carried by low orbiting satellites into the upper ionosphere or by rockets into the lower ionosphere, where the drag is so large that satellites quickly go spiralling downwards. Rockets and satellites can be at one place at the time only, therefore they give very limited information. Besides, these devices are very costly. It is for these reasons that most of our knowledge of the ionosphere comes from remote sensing.

Remote sensing techniques enable the determination of ionospheric electron density via radio propagation experiments. The single frequency techniques use information from amplitude, phase delay, polarization angle or angle of arrival. Some techniques employ a whole range of frequencies to obtain additional information. The radio propagation experiments are based on the fact that the index of refraction in the ionosphere depends on electron density, magnetic field, density of neutral particles, frequency, etc. (The index of refraction for radio waves is discussed in section 2.3). Now follows a description of the three most important observational techniques: the ionosonde, the incoherent scatter radar and radio beacon observation.

The ionosonde

An ionosonde determines the ionospheric vertical profile from the ground up to the height of maximum electron density. Its workings are based on the reflection of radio waves by the conducting ionospheric plasma. This reflection occurs when the plasma frequency is higher than the sounding radio frequency (see section 2.3). Because the plasma frequency is a function of electron density, these reflections can be used to sound the electron density. The ionosonde transmits signals of different frequencies upwards and it registers the time by which every signal is delayed at return. This time delay contains information on the height of the layer with that specific plasma frequency. The accurate determination of height is somewhat tricky, because the phase and group velocities below the layer of reflection depend on the electron density as well. The highest frequency reflected by the ionosphere is the plasma

frequency of the layer with maximum electron density, this frequency is called f_oF_2. Only radio waves with higher frequency can penetrate beyond this layer and these waves escape the earth. Consequently, ionosondes give information about the bottomside profile only.

Because the beamwidth of an ionosonde antenna is quite large, typically 40°-60°, the interpretation of ionosonde data depends quite strongly on the assumption that the ionosphere is stratified. Deviation from stratification, the so-called spread F, prompts unreliable results. When ionograms are used to reconstruct the bottomside profile, further model input is required. Ionosondes are inexpensive instruments and over a hundred are installed worldwide. The greater part of our knowledge of the ionosphere is based on ionosonde measurements and do not regard the topside. Yet, most of the electron content is located above the layer of maximum density. That is precisely the reason why the topside region is of great importance for transionospheric radio propagation. Our knowledge of the topside ionosphere comes mainly from topside sounders carried by spacecraft (Alouette, in the sixties), from incoherent scatter radars and from radio beacon observation.

The incoherent scatter radar

The principle behind the incoherent scatter radar is Thomson scattering: the scattering of electromagnetic waves by free electrons. It works much the same as normal radar. There is a transmitter and one or more receivers to record the echoes. The total echo power is a measure of electron density. In addition, the frequency shift of the echo gives the bulk motion of the plasma and its spectral width is a measure of the temperature. In imaging mode, the radar can make vertical cross sections of the ionosphere. The reach is about 1000 km. The instrument is very expensive and just about seven are operated over the world.

TEC from radio beacon observation

By observing certain propagation parameters of radio waves from sources beyond the ionosphere, it is possible to determine the integrated electron density along the line of sight, or TEC. TEC measurements can be made in many different ways. There is always a line of sight involved, or more precisely a phase or group path. This path is the line along which electron density is integrated. The line of sight begins in a radio beacon and ends in a receiver. The beacon is either a beacon satellite or a celestial point source of radio waves. The receiver measures phase shift, group delay or Faraday rotation. Each of these observables is a measure of TEC.

It is clear that there are many methods to determine TEC. Chapter 2 will discuss some of the techniques and measurement systems. The most widely used among them is the differential Doppler technique, which uses phase shift measurements. As the present study uses data collected by this technique, it will get most attention.

1.4.2 Imaging

For the study of the regular and stratified ionosphere, single station ionosonde and TEC records are sufficient. For better understanding of irregularities, imaging is most welcome. How can we produce such images? For obvious reasons, the data collection cannot be done by local measurements: very expensive and very impractical. Remote sensing, by contrast, gives a variety of possibilities. The first, of course, is the incoherent scatter radar. Another

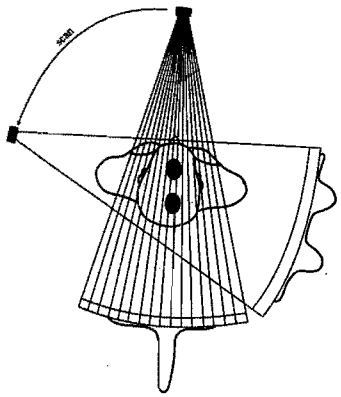

Figure 1.4: Principle of the computerized tomography scanner. The CT scanner measures the line integrals along the straight lines. A bundle of these forms a projection, of which two are drawn (the curves). The positions of the eggs can be reconstructed from these projections. Tomography is the technique to reconstruct, or compute, distributions (pictures) from a set of its line integrals.

kind of image can be compiled from a grid of ionosondes. Due to the fact that the ionosonde's antenna beam is so wide, and that there are not so many ionosondes installed, this kind of image can only be used to study very large scale structure. An example is a map of global f_0F_2 distribution. A grid of ionosondes cannot be used to image irregularities smaller than about 500 km.

Secondly, there is the possibility of holographic imaging of ionospheric scatterers. This technique requires phase and amplitude registration of a scattered wavefield, (Rogers and Ireland 1980, Tauriainen 1982). Backpropagation of the recorded wavefield gives the structure of the scatterer. This is essentially the same as ionospheric diffraction tomography (Kunitsyn et al 1994). Both techniques give images of small scale ionospheric structure at a certain height. Typically, such images have sizes of 10 by 10 km. The problem with these techniques is that the height to which the recorded wavefield must be backpropagated, i.e. the scatterer's height, must be known in advance. Furthermore, the experiment requires many receivers that register both phase and amplitude of radiation from a source of coherent radiation (a beacon satellite). For these reasons, these techniques cannot be considered a great success. From the same drawbacks suffers another technique: statistical tomography (Kunitsyn et al 1994). This technique must be applied when there are too many scatterers to generate meaningful images. In that case, statistical tomography can be used to derive the statistical properties of the scatterers.

1.4.3 Tomography

Above, we discussed two forms of tomography that can be used to study scatterers: diffraction tomography and statistical tomography. In the absence of scattering and diffraction, however, the classical form of tomography can be applied: straight ray tomography. In ionospheric research, it is the kind of tomography with the greatest promises. Unless otherwise

stated, this thesis understands straight ray tomography were tomography is written.

In straight ray tomography, the (radio) waves travel along straight paths and thus allow the measurement of total electron content (TEC). Of course, TEC is integrated electron density and therefore not the same as (local) electron density. The process to transform a set of many line integrals of a distribution into the distribution itself is called tomography. In other words, we need tomography to transform a set of TEC measurements into an image of electron density.

Tomography is best known from its application in medical imaging: the CT (computerized tomography) scanner. In figure 1.4, we see the set-up of such a machine. The profile of a single projection of X-rays cannot fix the position of two eggs in the patient's head. A position fix becomes possible with an additional projection from a different angle. With views from all directions, i.e. when all line integrals are measured, it is possible to reconstruct all possible distributions. Chapter 3 will focus on tomography.

Austin (1986) proposed to use differential Doppler data from NNSS satellites for tomographic inversion. This gives the measurement geometry embellishing the cover of this book and recurring in figure 4.3. It shows a NNSS satellite in orbit and an array of five receivers on the satellite's ground-path. The NNSS satellites move in a polar orbit at around 1100 km altitude, completing a revolution every 108 minutes. This means that they pass an observer in a quarter of an hour and that their ground-path is approximately a meridian. A set of at least three receivers should be spreaded over a fair distance, say 1000 km, to ensure sufficient angular coverage. The figure also shows the lines of sight, they criss-cross the surface of reconstruction, indicated by the pixel grid. Every line of sight is associated with a TEC measurement (electron density integrated along the line). The grand total of TEC data along all lines, crossing each other and spanning the field of view, can be converted into an image of electron density. This gives a vertical cross section of the ionosphere, where the electron density is given as a function of altitude and latitude.

Chapter 4 describes the application of tomography to ionospheric imaging. It will be shown that the main problem is the incompleteness of the set of line integrals (there are no horizontal lines in the cover figure). This has severe consequences for the reconstruction techniques. The methods from the CT scanner cannot be used and must be replaced by methods that somehow make up for the missing information. Chapter 4 reviews such reconstruction algorithms. In many applications, the use of models is perfectly sound. If, however, the reconstructions are used for better understanding of the ionosphere or to develop better models, it is not so smart to start with existing models in the first place. Therefore we present a new algorithm that depends very little on model input. The new algorithm is formulated in sufficiently general terms to be applicable in other areas than the ionosphere. Many industrial or scientific diagnostic systems get insufficient input information. Here, the new algorithm can help. The mathematical details of the algorithm follow in chapter 5. Chapter 6 continues with practice. It presents the results of an experiment in tomography of the ionosphere.

Chapter 2

Differential Doppler

The differential Doppler technique is a method to determine total electron content. It is used to measure the line integrals for tomography of the ionosphere. The chapter describes the history, the theory, and the applications of differential Doppler. It concludes with the characteristics of the equipment used for this research.

2.1 The principle

As we have anticipated in 1.4, the differential Doppler technique is based on phase- or frequency shift measurements. Frequency is the time derivative of phase and a frequency shift is often called a Doppler shift. In the early days of the technique, frequency shifts rather than phase shifts were measured and the differential Doppler technique's name stems from that time. The word 'differential' indicates that the technique uses two frequencies, whose Doppler shifts are scaled and subtracted.

The phase or frequency shifts are the result of changes in the optical path length, which is the index of refraction integrated over the phase path. In its turn, the index of refraction is a measure of electron density. Therefore, the differential Doppler measurements give information on electron density. That is the technique in a nutshell.

Let f be the frequency of the carrier wave, then ω is the angular frequency and $\omega = 2\pi f$. The phase, ϕ_t, of the carrier wave at the transmitter is given by $\phi_t = \omega t$, where t is the time and at $t = 0$, the phase is assumed zero. The phase ϕ_r and the angular frequency ω_r, both at the receiver, are given by

$$\phi_r = \phi_t - \omega\frac{L}{c} = \omega t - \omega\frac{L}{c}\,, \tag{2.1}$$

$$\omega_r = \frac{d\phi_r}{dt} = \omega - \underbrace{\frac{\omega}{c}\frac{dL}{dt}}_{\text{Doppler shift}}\,. \tag{2.2}$$

Here c is the speed of light in vacuum and L is the optical path length. L is defined indirectly, L/c is namely the time that phase, say a wave-crest, takes to go from transmitter to receiver. This travel-time depends on the phase path and the phase speed. It follows that the optical path length is given by

$$L = \int_t^r n ds \tag{2.3}$$

where ds is an element on the phase path between transmitter t and receiver r. The phase slowness is represented by the index of refraction n. The real part of the index of refraction is namely the speed of light divided by the phase speed.

Section 2.3 will elaborate on the relation between electron density and the index of refraction. In section 2.4 we show that, in many cases, the phase path is well approximated by a straight line. It will also be argued that, in general, the optical path length differs not much from the geometrical distance between transmitter and receiver, which is rationale behind the following division:

$$L = L_0 + \Delta L \ . \tag{2.4}$$

Here L_0 is the geometrical distance between transmitter and receiver and ΔL is the range error, and $L_0 \gg \Delta L$. Because L_0 dominates the optical path length, its time derivative, the the motion parallel to the line of sight, $v_{||} = dL_0/dt$, rules the Doppler shift, as can be seen from (2.2).

The subtle contributions to L, due to the characteristics of the medium, are embodied in ΔL. This includes information on the electron density. To extract this information from phase shift measurements, L_0 must be known and corrected for. As $L_0 \gg \Delta L$, a small error in L_0 destroys the useful information. This problem can be solved by differential measurements. In the differential Doppler technique, frequency or phase shifts at two harmonically related (or coherent) frequencies are measured. These measurements are scaled to a reference frequency and subtracted. In this way, all effects that are independent of frequency are cancelled. L_0 is independent of frequency, and so is the tropospheric index of refraction. Luckily, the ionospheric index of refraction does depend on the frequency, it is said to be dispersive. Because the differential procedure cancels the non dispersive effects (geometrical distance and tropospheric refraction), the dispersive effects of ionospheric refraction are highlighted. These effects can be manifest in three ways:

1. The rocket

   Consider a rocket in the ionosphere, propagating away from a receiver on earth with a motion basically parallel to the line of sight. In this set-up, the differential Doppler shift scales with the radial velocity $v_{||}$ times the dispersive part of the index of refraction at the transmitter. In these experiments, the electron density around the rocket can be derived from the differential Doppler shift and from knowledge of the radial motion of the rocket.

2. The orbiting satellite

   Replace the rocket by a satellite that passes a ground based observer. The satellite moves in an orbit that is over most of the ionospheric electron content. The phase path connecting transmitter and receiver sweeps through the ionosphere. As the phase path moves, the integrated index of refraction along the phase path changes. This is observed as a Doppler shift. As long as the satellite passes quickly and ionospheric fluctuations are negligible, the differential Doppler shift is a measure of the gradient of the integrated electron density. This is the method applied in this thesis.

3. The geostationary satellite

   When a geostationary satellite is observed from the earth, there is no relative motion beyond a few degrees, and the phase path is almost stationary. Due to fluctuations over

time in the index of refraction along the fixed phase path, however, the optical path length can change. In this case, the differential Doppler shift records are a measure of the time derivative of the integrated electron density.

Remark that the first method gives local (in situ) electron density. The other two yield electron density integrated over a line between transmitter and receiver. This quantity is the total electron content, or TEC. In these latter two, differential phase measurements will do equally well as differential frequency measurements. In phase measurements, and in phase difference measurements, the phase counting starts when the receiver gets a phase lock on the signal. At this moment, the phase count starts at an arbitrary number. This implies that TEC is known only to an unknown offset, or bias. As a consequence, there are three ways to represent TEC: differential TEC, relative TEC and absolute TEC. Differential TEC is the change in TEC over a certain period (the integration interval), it corresponds to the raw output of the receiver: the increase in the differential phase count. Mind that the 'differential' in TEC does not refer to the two frequencies as in differential Doppler or phase, but rather to the change in TEC over the integration interval. When differential TEC is integrated, we get relative TEC. The data are relative to the unknown TEC at phase lock. This unknown offset is of course the constant of integration. When the unknown offset is estimated some way or another, and added to the relative TEC, we speak of absolute TEC. Absolute TEC is the proper line integral of electron density.

When we measure frequency instead of phase, the unknown offset appears via a different route. Frequency is the time derivative of phase, and to extract the range error information, we must integrate frequency over time, as can also be seen from equation (2.2). The integration will result in an unknown constant of integration, which corresponds to the same offset in TEC as above.

2.2 Historical perspective

The three differential Doppler set-ups that were discussed in the previous sections have all been applied. In this section, we will sketch the historical importance of these applications. We see that, in the course of time, both the transmission frequency and the transmitter altitude increase: from 4 MHz transmitters on V-2 rockets to geostationary satellites transmitting at frequencies beyond 10 GHz.

1. The rocket

   Since the fifties the Doppler shift of radio signals has been used as a means to measure ionospheric electron density. Seddon (1953) used two harmonically related frequencies radiated from V-2 rockets to measure local electron density. These frequencies were 4.3 MHz and its sixth harmonic.

   For imaging by tomography, we need integrated electron density or TEC, therefore we do not further consider this technique.

2. The orbiting satellite

   Another technique uses the Doppler shift of a carrier wave from a transmitter that moves in an orbit above most of the ionospheric electron content. Navigation satellites in circular orbits at an altitude higher than 1000 km, are commonly used for this purpose. As the satellite moves, the phase path shifts and therefore the integrated electron density

along the phase path changes. This is registered as a phase or frequency shift, as we saw in the previous section.

Work in this area began shortly after the launch of the first artificial satellites (Weekes 1958). As we have already mentioned, two harmonically related beacon frequencies are needed. For a single frequency beacon, frequency stability is too poor, and knowledge of orbital parameters too imprecise, to separate ionospheric from kinematic effects, that are much stronger. The differential use of two harmonic frequencies eliminates this problem, it separates non-dispersive (geometrical and tropospheric) effects from the dispersive ionospheric effects. Ross (1960) used the 20 MHz and 40 MHz signals from satellite 1957δ2, or Sputnik III, to determine total electron content. Improvements came when Garriot and Nichols (1961) showed that it is easier to derive electron content from phase rather than frequency registration.

Further improvements were made when the experimental navigation satellite Transit 2a was launched. This satellite had a higher and more circular orbit and transmitted at higher frequencies (54 MHz and 324 MHz), so as to better justify the linearizations in sections 2.3 and 2.4 of this chapter (De Mendonça 1962). Later on, the Navy Navigation Satellite System (NNSS , or TRANSIT, see section 2.6) and its Russian equivalent CICADA (Daly 1984), became available for ionospheric research; both systems transmit at 150 MHz and 400 MHz. Since then, most efforts were directed at improving the methods that estimate the unknown phase offset from the phase shift measurements themselves. Leitinger (1975) proposed a method to determine this offset from differential Doppler measurements of two receivers, the so-called two station method.

Austen (1986) gave new impulses to the differential Doppler field, when he proposed to use the data from an array of receivers for ionospheric imaging by computerized tomography. It is by these impulses that the present study was initiated.

At present, the Global Positioning System (GPS, or NAVSTAR) replaces NNSS as asatellite based navigation system and the future of the NNSS satellites looks dim. For this reason, people are switching to GPS for differential Doppler measurements. GPS is in a 20,000 km, 12 hours orbit and transmits at 1.227 GHz and 1.575 GHz. In principle, it should possible to get offset free TEC data from GPS by measuring the differential group delay instead of phase shift (or phase delay). In practice, TEC data from group delay are very unreliable, due to measures the US army has taken to prevent misuse of the system by the enemy. These measures are known as anti spoofing and selective availability. Rumours are, however, that these measures will be lifted in 1997.

Just as NNSS has its Russian equivalent in CICADA, so does GPS: GLONASS. In fact, the Russian GLONASS system came before GPS. These are all navigation satellites conceived by the military. In their original function, the satellites use the second frequency to correct for ionospheric refraction, thus enhancing navigational precision. Almost all applications of the differential Doppler technique use these navigation satellites with their two-frequency beacon. The technique can therefore be seen as a spin-off of military precision positioning.

3. The geostationary satellite

Radio beacons have been installed on geostationary satellites as well. A fine example is the ATS-6 satellite, that could be used both for differential phase and Faraday rotation

measurements (Davies et al., 1975). As these satellites hardly move with respect to a ground based receiver, researchers call the technique 'differential phase' rather than 'differential Doppler'. There are some important differences associated with beacons on geostationary satellites, compared to those on passing satellites.

(a) As the path between satellite and receiver does not change, the technique gives the time evolution of TEC rather than its spatial structure.

(b) When the geostationary satellite's signals remain phase locked all the time, the unknown constant of integration needs to be estimated only once. It is not possible though, to estimate the offset from the differential phase record, as can be done from an orbiting satellite's record.

(c) As geostationary satellites are in an orbit at 36,000 km altitude, they really allow monitoring of *total* electron content. By contrast, the TEC record of a NNSS satellite pass at 1100 km altitude, misses everything overhead: the upper ionosphere and the plasmasphere. This may amount to a few percent in TEC.

(d) The more recent geostationary satellite Olympus had its beacons in the GHz range: at 12.5, 20 and 30 GHz. At these frequencies, the dispersive characteristics of heavy rainfall can influence the differential phase registration and thereby obscure the ionospheric effects (Mawira 1990).

2.3 The index of refraction

To interpret radio signals transmitted through the ionosphere, it is necessary to have some understanding of radio propagation through the atmosphere. This understanding starts with the index of refraction. In this section we will give an expression for the index of refraction. The relation between electron density and the ionospheric index of refraction will be linearized, so that it can be used for TEC measurements. We will show that this linearization is justified for frequencies higher than the lowest NNSS or CICADA frequency, which is 150 MHz (corresponding to a wavelength of $\lambda = 2$ m).

The index of refraction n is a complex quantity. The real part scales with the inverse of the phase speed, v_p, of the radio waves: $\Re(n) = c/v_p$, where c is the speed of light. As the differential Doppler technique measures phase (or frequency), we are only interested in the real part of the index of refraction. The imaginary part is a measure of the absorption. In the radio window, there is practically no absorption and the atmosphere is transparent to radio waves. This radio window roughly extends from 10 MHz ($\lambda = 30$ m) to 37 GHz ($\lambda = 0.8$ cm). The lower frequency limit is set by the ionospheric plasma frequency and the upper limit is the result of absorption by water and oxygen molecules. Because the NNSS and CICADA frequencies (150 MHz and 400 MHz) lie in the radio window, the index of refraction can be considered real-valued at these frequencies.

We can make a distinction between the tropospheric index of refraction, which is non dispersive, and the dispersive ionospheric index of refraction. In the ionosphere, free electrons and the magnetic field affect radio wave propagation. Tropospheric propagation effects are caused by neutral particles, whose density has a non-negligible effect in the troposphere only.

In the neutral part of the atmosphere, the index of refraction at radio wavelengths is

independent of frequency. It is given by (Crane 1976, page 187):

$$n_{trop} = 1 + 7.76 \times 10^{-7} \frac{p}{T} + 3.73 \times 10^{-3} \frac{p_w}{T^2} \,. \tag{2.5}$$

Here T is the absolute temperature, p is the atmospheric pressure in Pascal and p_w is the partial pressure of water vapor. Under the conditions we consider, this expression is estimated to be within 0.5 % of the true value. At normal ground level conditions, $p = 10^5$ Pa and $T = 290$ K, n_{trop} may vary from 1.00027 at zero humidity to 1.00036 at 100 % humidity. With increasing altitude, n_{trop} decreases to 1.

In the ionosphere, the complex index of refraction is given by the Appleton-Lassen formula. This formula is based on a simplified description of the plasma. One considers electron motions only. By their large mass, the positive ions are almost motionless, while their presence neutralizes the negative electron charge. This assumption is justified below. The thermal motions of the electrons are considered unimportant, such a medium is called a cold plasma. The third assumption is that the disturbances in the plasma induced by the electromagnetic wave are small and do not affect the propagation itself, i.e. the problem is linearized. The Appleton-Lassen formula for the complex index of refraction is given by (e.g. Budden 1985, Rawer 1993)

$$n_{ion}^2 = 1 - \frac{\tilde{X}}{1 - \frac{\tilde{Y}^2 \sin^2\theta}{2(1-\tilde{X})} \pm \sqrt{\tilde{Y}^2 \cos^2\theta + \frac{\tilde{Y}^4 \sin^4\theta}{4(1-\tilde{X})^2}}} \tag{2.6}$$

Here θ is the angle between the wave vector and the geomagnetic field. The tilde implies division by the absorption factor $(1+iZ)$. X, Y and Z are the ratios between the characteristic frequencies of the medium and the angular frequency of the signal ω:

$$X = \frac{\omega_p^2}{\omega^2} \qquad Y = \frac{\omega_c}{\omega} \qquad Z = \frac{\nu_e}{\omega} \tag{2.7}$$

These ratios are very small, as we will see. This will allow simplification of the Appleton-Lassen formula. Here follows a short discussion of the characteristic frequencies:

- The effective collision frequency

  In the definition of Z, ν_e is the effective collision frequency. Charged particles oscillate along with the passing electromagnetic waves. When these particles collide with other (mainly neutral) particles, the energy of the radiation is dissipated. Where charged particles exist in the relatively dense environment of the lower ionosphere, collisions are frequent and absorption is relatively strong. A nonzero collision frequency makes the index of refraction a complex number and its imaginary part corresponds to the absorption coefficient. At mid-latitudes, the effective collision frequency is smaller than about 10^4 Hz, and $Z < 10^{-5}$ at the lower NNSS frequency of 150 MHz.

- The plasma frequency

  The angular electron plasma frequency ω_p is given by

  $$\omega_p^2 = \frac{e^2 N_e}{m_e \epsilon_0} \,. \tag{2.8}$$

  Here e is the electron charge, m_e is the electron mass, N_e is the free electron density and ϵ_0 is the vacuum permeability. The plasma frequency, $f_p = \omega_p / 2\pi$, corresponds

to the frequency of the electron oscillations against the positive background. Below the plasma frequency, n_{ion}^2 is negative and n_{ion} is an imaginary number. This explains why radio waves at these frequencies are reflected by the plasma. At mid-latitudes the plasma frequency is $f_p < 15$ MHz, for $N_e < 280 \times 10^{10}\text{m}^{-3}$. Therefore $X < 0.01$ at $f = 150$ MHz.

- The gyro frequency

  The angular frequency of the rotation of an electron around a magnetic field line is given by ω_c, for cyclotron frequency (electron gyro frequency). It is given by

$$\omega_c = \frac{eB}{m_e} . \tag{2.9}$$

  At mid-latitudes, the geomagnetic field strength B is $B \approx 5 \times 10^{-5}$ Tesla and it follows that $f_c = \omega_c/2\pi \approx 1.4$ MHz and $Y \approx 0.01$ at 150 MHz.

  The geomagnetic field makes the ionosphere both an anisotropic medium and a doubly refracting (birefringent) medium, although these characteristics are related. In an anisotropic medium, the index of refraction depends on the angle θ between the direction of propagation and the magnetic field, as can been seen in (2.6). The consequence of double refraction is that there are two and only two characteristic waves that can propagate in the plasma, one with the + sign and one with the − sign in equation (2.6). The difference between these modes is the polarization angle and the phase speed. With propagation parallel to the magnetic field, the + sign corresponds to left circular polarization and the − sign to right circular polarization. With perpendicular propagation, the + sign corresponds to linear polarization parallel to the field and the − sign to linear polarization perpendicular to the field. In this case, the + sign is referred to as the ordinary mode, because the index of refraction is the same as without a magnetic field. The − sign corresponds to the extraordinary mode. The fact that the phase speed depends on the polarization, causes the Faraday rotation, which is the rotation of the polarization angle. It is clear that the distinction between the modes disappears when the magnetic field vanishes.

The electron plasma frequency and the electron gyro frequency both have their ion counterparts. These characteristic frequencies scale with the inverse of the particle's mass. Due to the large ion mass, the ion plasma frequency and the ion gyro frequency are much lower than their electron equivalents, which are already small compared to the radio frequencies under consideration. Because, the ion plasma and gyro frequencies are so small the previous assumption of a stationary ion gas is validated.

For TEC measurements we need a linearized relationship between the ionospheric index of refraction n_{ion} and the electron density N_e. As Z is very small, we can neglect the effect of collisions. Besides, collisions mainly affect the imaginary part of the index of refraction and we are only interested in the real part. When Z is set to zero, refraction becomes real and the tildes in (2.6) can be omitted. This simplification causes a relative error Z^2, or less than 10^{-10}, in the real part of $(n-1)$.

As X and Y are small, the first term in the square root of (2.6) will dominate when $2|\cos\theta| > Y\sin^2\theta$. For $Y = 0.01$, the left hand side of this inequality is more than 3 times

larger than the right hand side, when $\theta < 89.2^0$ or $\theta > 90.8^o$. Therefore, the so called quasi-parallel approximation is valid for almost all angles between the magnetic field and the radio propagation:

$$n_{ion}^2 = 1 - \frac{X}{1 \pm Y \cos\theta} \tag{2.10}$$

This formula is still too complicated. What error do we introduce if we neglect the magnetic field altogether? Under the worst possible circumstances ($X = 0.01$, wave propagation along the magnetic field and circular polarized radiation), the error in $(n_{ion} - 1)$ would still be less than 1 %. Consequently, we feel justified to drop Y from the Appleton-Lassen formula.

The relation is not linear yet. As $X \ll 1$, we can approximate n_{ion} by the first order term of the Taylor expansion around $X = 0$,

$$n_{ion} = \sqrt{1 - X} \approx 1 - \frac{X}{2} = 1 - \frac{e^2}{2m_e\epsilon_0}\frac{N_e}{\omega^2} = 1 - 40.3\frac{N_e}{f^2} \tag{2.11}$$

where the final result is in SI units. This final approximation introduces an error smaller than 0.25 % in $(n_{ion} - 1)$.

We conclude that the ionospheric index of refraction at 150 MHz lies in the following range: $0.995 < n_{ion} < 1$. It is less than one, indicating a phase speed greater than the speed of light.

The main result of this section is the linearized relationship between the index of refraction and the electron density. The toll of the linearization is small: a maximum error of 1 % in $(n_{ion} - 1)$ at 150 MHz and decreasing linearization error with increasing frequency. The ionospheric index of refraction is dispersive, whereas the tropospheric index of refraction is independent of frequency.

2.4 Rays and the optical path length

The linearized relationship between index of refraction and electron density is not sufficient to interpret differential phase shifts as TEC changes. The other criterion is that the phase path between transmitter and receiver can be approximated by a straight line. Before we can estimate the errors introduced by this approximation, we must justify the concepts of phase path, ray, and optical path length. These concepts are introduced and validated by the geometrical optics approximation. There are two criteria for the applicability of the geometrical optics method (see Kravtsov and Orlov 1990, section 2.10):

(i) The index of refraction must not vary significantly over the first Fresnel zone.

(ii) Rays may not come so close to each other that they can no longer be distinguished. This happens near caustic surfaces, for example in the focus of an optical system.

The concept of the Fresnel zone relates to Huygens' principle. In this principle, all elements of a wavefront can be considered secondary emitters. Where the secondary wavelets are in phase, they create an advanced (secondary) wavefront, and so on. Consider a ray between transmitter and receiver and a point on this ray, the stationary point, at a distance d from the receiver. It is known since Fresnel that the major contribution to the field at the receiver, comes from a small surface around the stationary point. This small surface is the first Fresnel zone. Its shape and surface are defined by the requirement that the (secondary) wavelets emitted in phase all over the zone are a maximum of π radians out of phase with wavelets

from the stationary point. It is clear that the Fresnel zone is circular and that the phase difference of π radians corresponds to a path length difference of $\lambda/2$. This sets the radius r_F of the first Fresnel zone to $r_F = \sqrt{d\lambda}$.

The two criteria from above translate into (Kravtsov and Orlov, 1990):

$$r_F \ll \frac{n}{|\nabla_\perp n|} , \tag{2.12}$$

where $\nabla_\perp n$ stands for the gradient of the index of refraction perpendicular to the ray. For a stratified ionosphere we may write, with (2.11),

$$|\nabla n| = \left|\frac{dn_{ion}}{dz}\right| = \left|\frac{-40.3}{f^2}\frac{dN_e}{dz}\right| , \tag{2.13}$$

where z is the altitude. In a Chapman layer the steepest gradient in the electron density is

$$\max(\frac{dN_e}{dz}) = 0.24\frac{N_{e,max}}{H} . \tag{2.14}$$

In extremely unfavorable but stratified conditions, we have $N_{e,max} = 280 \times 10^{10}\mathrm{m}^{-3}$ and ionospheric scale height $H = 10$ km. This gives for

$$\frac{n}{|\nabla_\perp n|} \approx 8.3 \times 10^6 \text{ m} . \tag{2.15}$$

The radius of the first Fresnel zone at $d = 2000$ km from the observer and at $\lambda = 2$ m (150 MHz) equals $r_F = 2 \times 10^3$ m. We conclude that condition (2.12) is satisfied and that the geometrical optics approximation is valid for the description of ionospheric radio wave propagation at the frequencies considered.

Of course, there sometimes are small scale irregularities that have far greater electron density gradients than those of the Chapman layer. These disturbances scatter radio waves, which causes wild oscillations in phase and amplitude. This is called scintillation. If there are traces of scintillation in the data, the geometrical optics approximation is violated and the data may not be used for TEC determination.

While the geometrical optics approximation is validated and the concept of rays is justified, we need to go one step further to see if the rays approximate straight lines. In section 2.1, we have defined the optical path length L. We have also distinguished two contributors to L: the geometrical distance, or range, L_0 and the range error ΔL. This is expressed by the following formula:

$$L = \int_{ray} nds = \underbrace{\int_{line} ds_0}_{L_0} + \underbrace{\int_{line} (n-1)ds_0 + \int_{ray} nds - \int_{line} nds_0}_{\Delta L} . \tag{2.16}$$

Here ds is a path element along the ray and ds_0 is a path element along the straight line (of length L_0) between transmitter and receiver. Propagation is such that the optical path length is stationary to small variations in the path. This is the Fermat principle. In general it means that the phase takes the fastest route, or minimum L. If the rays were to propagate through vacuum, the optical path length would equal the geometrical distance between transmitter and receiver: $L = L_0$. In any other medium there is a difference between the geometrical

distance and the optical path length. This is the range error, ΔL, which is due to refraction, and

$$\Delta L = \underbrace{\int_{line} (n-1) ds_0}_{\propto \text{ TEC}} + \underbrace{\int_{ray} n ds - \int_{line} n ds_0}_{\Delta L_{bend}} . \tag{2.17}$$

The first term in (2.17) is the straight line approximation to the range error, this term is proportional to TEC, as we will see below. The remainder, ΔL_{bend}, represents a correction for the bending of the ray. We will now demonstrate that this term can be neglected. If ray bending can indeed be neglected, ΔL is a good measure of TEC and the differential Doppler technique is founded on a sound base.

By neglecting the magnetic field, the ionosphere can be considered isotropic. By consequence, the phase speed and the group speed have the same direction, although a different magnitude. Therefore the group path (or ray) and the phase path are the same. Ray bending depends on the component of the gradient of the refractive index perpendicular to the ray. When the gradient is zero (homogeneous medium) or when the gradient is parallel to the ray, there is no ray bending. The latter is the case when the rays are perpendicular to the 'structure', such as vertical rays in a purely stratified atmosphere. Therefore ray bending increases with decreasing elevation angle.

Model calculations (Leitinger & Hartmann, 1983) on Chapman profiles (cf. section 1.1) show that the correction for ionospheric bending ΔL_{bend} is approximately

$$\Delta L_{bend} \approx -\frac{\tan^2 \chi}{8 \cos \chi} X_{max}^2 \tau (0.68 - \frac{\tau}{h_t}) . \tag{2.18}$$

Here χ is the zenith angle of the ray at mean ionospheric height h_i, X_{max} is the squared ratio of maximum plasma frequency (for $N_{e,max}$) over radio frequency, h_t is transmitter height and τ is the ionospheric slab thickness (section 1.3). The correction scales with $1/f^4$. Weenink (1987) derived a general expression for ΔL_{bend}, based on a series expansion of the small deviation of n_{ion} from 1 and of the deviation of the propagation from the straight line. Applying a Chapman profile to Weenink's expression gives the same result as (2.18), to our great satisfaction.

In table 2.1, NNSS satellite carrier wave ranges, range errors and ray bending errors, are given for a worst case undisturbed ionosphere (disturbances may enhance ray bending, however). We have separated the effects of the (non-dispersive) troposphere and the (dispersive) ionosphere on the range error: $\Delta L = \Delta L_{trop} + \Delta L_{ion}$. We see that the effect of ionospheric ray bending ΔL_{bend} on the range error ΔL is less than a percent and can indeed be neglected. The fact that ray bending is so small implies that there are no caustics, whose presence would violate criterium (ii). We have neglected tropospheric ray bending, which is independent of frequency and very small: additional range errors of about minus a centimeter.

Filling in the numbers from section 2.3, gives for the ionospheric range error:

$$\Delta L_{ion} \approx \int_{line} (n-1) ds_0 = -\frac{e^2}{2 m_e \epsilon_0 \omega^2} \int_{line} N_e ds_0 = -\frac{40.3}{f^2} \text{ TEC} , \tag{2.19}$$

where the final result is in SI units.

satellite elevation (^{0})	χ (^{0})	L_0 (km)	ΔL_{trop} (m)	ΔL_{ion} (m)	ΔL_{bend} (m)
90	0	1100	2	-1505	0
60	28.1	1240	2	-1706	-1
30	54.6	1852	5	-2597	-5
10	67.9	2949	12	-3999	-25
5	69.6	3385	23	-4316	-32
0	70.2	3901	100	-4442	-35

Table 2.1: Tropospheric and ionospheric range errors and effect of ionospheric ray bending for NNSS satellite at $f = 150$ MHz, altitude 1100 km. Ionospheric parameters: $N_{e,max} = 280 \times 10^{10}\mathrm{m}^{-3}$, slab thickness τ =300 km, mean ionospheric height $h_i = 400$ km.

2.5 The differential Doppler technique

In the preceding sections, we have prepared the introduction of the differential Doppler technique. Now it is time to put everything together.

The satellite transmits two harmonically related, or coherent, frequencies, f_1 and f_2. Coherent means that both frequencies are harmonics of a common basis frequency. Therefore $f_2 = qf_1$, where q is a rational number. For the NNSS, these numbers are: $f_1 = 150$ MHz, $f_2 = 400$ MHz and $q = 8/3$.

The receiver measures the weighted phase difference between phases ϕ_1 and ϕ_2, the differential Doppler phase $\Delta\phi$. Weighted phase difference means that both phase counts are scaled to a reference frequency. Here, f_2 is the the reference frequency. From equation (2.1) we have

$$\Delta\phi = q\phi_1 - \phi_2 = \Delta\phi_0 - \frac{1}{c}(q\omega_1 L_1 - \omega_2 L_2) \ . \tag{2.20}$$

$\Delta\phi_0$ is an unknown phase constant that incorporates the differential phase offset at the transmitter and the unknown number of cycles at phase lock, mentioned in section 2.1. The optical path length can be split, see equation (2.16):

$$L = L_0 + \Delta L_{trop} + \Delta L_{ion} \ . \tag{2.21}$$

The geometrical distance L_0 and the tropospheric range error ΔL_{trop} are independent of frequency. These non-dispersive terms cancel in the evaluation of (2.20). Filling in the numbers gives

$$\Delta\phi = \Delta\phi_0 + \frac{e^2}{2cm_e\epsilon_0}(\frac{q}{\omega_1} - \frac{1}{\omega_2})\mathrm{TEC} = \Delta\phi_0 + 1.29 \times 10^{-14}\ \mathrm{TEC} \ . \tag{2.22}$$

Here we have used equation (2.19), the phase is scaled to the upper NNSS frequency of 400 MHz. Typically, TEC varies between $10^{16}\mathrm{m}^{-2}$ and $10^{18}\mathrm{m}^{-2}$, depending on the time of the day and on the solar activity.

Considerable research has been invested in methods to determine the unknown phase constant $\Delta\phi_0$, which is different every time the receiver locks on the satellite signals. These

methods estimate this offset from a fit to the differential Doppler data (see Leitinger and Putz, 1978). It is hereby assumed that the ionosphere is an infinitesimally thin layer at ionospheric height. This is of course a coarse simplification. When there is only one receiver, these methods further assume a smooth spatial variation (usually linear) of the electron content in the vicinity of the zenith. Leitinger (1975) proposed a method to estimate the offset from the differential Doppler data of two receivers. Although this method alleviates the assumption of smooth spatial variation, the infinitesimally thin layer assumption is maintained.

In section 4.1.1, the discussion will return to the implications of the unknown offset for tomography of the ionosphere. There we will see that tomography is possible without knowledge of the unknown offset. Therefore, the tomographic use of differential Doppler data is the only way to process these data without the implicit assumption of an infinitesimally thin ionosphere.

2.6 The Navy Navigation Satellite System

The U.S. Navy Navigation Satellite System (NNSS, or TRANSIT) was developed between 1958 and 1963 as a ship-borne navigational aid by the Applied Physics Laboratory at Johns Hopkins University. The work that immediately led to the development of the system, was the measurement of the Doppler shift in the radio transmissions from satellite 1957α, better known as Sputnik I, to determine its orbit. Shortly after, it was suggested that the same type of measurements could also be used the other way round: given the satellite orbit, determine the position of the receiver (see Newton, 1967).

The system became available to non-military users by mid-1967. Since then, it has also served as a means to perform geodetic surveying tasks. From the beginning of the nineties, the U.S. Global Positioning System (GPS) has replaced the NNSS as the major satellite based navigation system. At present however, the NNSS is still operational.

The position is determined from a series of measurements of the Doppler shift of signals transmitted during a single pass of a single satellite. Operation is independent of weather conditions and the system has a world-wide range. The number of operational satellites varies around six. They move in nearly circular polar orbits, at altitudes of about 1100 kilometers and with orbital periods of around 108 minutes. At geographic latitude 45^{o}, these satellites provide roughly one pass every hour. A pass lasts about a quarter of an hour. Since the satellites are in a polar orbit (inclination near $90°$), the ground track of a satellite roughly follows a meridian.

The satellites transmit three kinds of information: stable frequencies from which Doppler measurements can be made, timing signals every two minutes and orbital parameters. The satellites transmit two stable harmonically related carrier frequencies of 149.988 MHz and 399.968 MHz. Generally, these are referred to as 150 MHz and 400 MHz nominal frequencies. The 150 MHz signal is broadcasted at 1-2 Watts and the 400 MHz signal at typically twice that power. Each of these carrier frequencies undergoes a Doppler frequency shift, when detected by a receiver, due to the relative velocity between satellite and receiver. The orbital parameters and timing signals are transmitted as balanced digital phase modulations (advance or retardation of the phase) on the stable carrier frequencies, so as not to disturb the Doppler measurements. The bit rate is about 50 bits per second. Corrected timing information and new predictions of the orbital parameters are injected into the satellite memory banks once every 12 hours from a ground station in the U.S..

The user has a receiver which measures the Doppler shifts and decodes the satellite orbital data. Doppler counts, or phase counts, i.e. Doppler frequencies integrated over a 4.6 seconds period, are related to the change in range between satellite and receiver during that interval. These range differences are functions of the unknown receiver coordinates and the satellite coordinates. When the satellite coordinates are known, a least squares estimate of the receiver coordinates can be made using the Doppler counts as observations.

Normal receivers measure the Doppler shift of the 400 MHz carrier wave only. The geodetic receivers also measure the 150 MHz Doppler shift. The additional information is used for a first order correction of the effects of ionospheric refraction. This permits more precise positioning, up to an accuracy of a few meters after several satellite passes. For ionospheric research, the dual frequency data offer important information, as we have seen in the preceding sections of this chapter.

2.7 The receivers

In the present study, we have used eight geodetic NNSS receivers manufactured by the Canadian Marconi Company. Two of these were type CMA-751 and six were the more recent type CMA-761. Five receivers were kindly put at our disposal by the Dutch airline carrier KLM, and the others by three institutes: the Delft University of Technology (TUD), the Royal Dutch Meteorological Institute (KNMI) and the geodetic department of the Dutch dike builders (Meetkundige Dienst Rijkswaterstaat). This Canadian Marconi equipment is portable and consists of three parts: the antenna, the receiver and the digital cassette recorder.

The antenna is a vertically polarized monopole antenna with a horizontal ground plane formed by eight rods mounted radially at the base. The maximum gain of the antenna is approximately 3 dBI. The antenna has an omni directional azimuth coverage that provides good radiation patterns at 150 MHz and 400 MHz. The patterns are symmetric around the vertical axis. For 150 MHz, the maximum gain is at $\sim 12^o$ satellite elevation and at 400 MHz at $\sim 40^o$ elevation. The half-power beamwidth is approximately 50^o at both frequencies. The advantage of this radiation pattern is that the antenna need not be pointed at the moving satellite. The fact that the antenna gain is zero when the satellite is in the zenith, is clearly a disadvantage. The base of the antenna forms a housing for a filter-preamplifier assembly. The ground plane diameter is one meter, the antenna height is 65 cm and it weighs 5 kilograms. Disassembled, it fits in a suitcase.

The antenna is connected to the receiver by a 50 Ohms coaxial cable. The receiver automatically acquires and locks on to the signals of a passing satellite, decodes the satellite messages and derives the Doppler shift frequencies, to produce digital outputs of orbital parameters and integrated Doppler counts. There is one little oddity. The receiver inverts the sign of the Doppler shift: the Doppler shift indicator on the front panel gives a negative shift when the satellite is approaching and positive when receding, quite contrary to the convention! The integration of the Doppler frequencies is performed over 24 periods of 4.6 seconds and one period of 9.6 seconds, together these add up to the 2 minute interval mentioned above. The output of the raw data (counts and orbital parameters) is generated every 4.6 (or 9.6) seconds. This period corresponds to a satellite displacement of 28 kilometers or $0^o.25$ geographic latitude.

The receiver has the dimensions of a medium sized suitcase and weighs roughly 30 kg. Power requirements are 10-30 Watts at 12 Volts direct current. The receiver has internal

batteries to stay operational and to keep up its memory during power failure. The receiver formats the acquired data and computes its position.

Via a 20 wires data cable the receiver is supposed to communicate with the digital cassette recorder. The cassette recorder stores the output of the receiver and it should feed the operating program to the receiver. This scheme poses two major problems: the magnetic information fades and the data cassettes must be replaced daily, which forbids autonomous operation. The problem of information fading may seem not so severe. When we tried the receivers for the first time, however, the old program tapes had become unreadable. That has caused a lot of trouble.

Connection to a personal computer instead of the cassette recorder solved the problems. To make this connection, we replaced the connector on the cassette recorder side of the data cable by a regular 25 pins connector. A simple commercial input/output card makes a parallel connection to a 286 IBM PC or a compatible computer. Down-loading programs is then a safe and simple job and a hard disk of 20 Megabytes is large enough to store months worth of data. In addition, the computer can preprocess the data.

A set of programs controlled operation of the PC. These programs load the operating program into the receiver, and they collect, process and store the data from the receiver. Another program performs diagnostic tests to check whether the system operates correctly. Some characteristics (lock-on time, maximum elevation, pass orientation and satellite number) and quality indicators of the last 15 passes are displayed on the computer screen, together with the results of the diagnostic tests. As a personal computer is not designed to run unattended for weeks, the software was made as robust as possible. Operation was made insensitive to power cuts and minor hardware failures, such as unreadable hard disk sectors.

2.8 Raw data output and processing

Every 2 minute interval, the receiver generates 25 records of raw data output. Each record contains 30 digits. The records contain four pieces of information:

1. Orbital parameters, their time derivatives and some satellite specific information are encoded in 22 of the 25 records.
2. A read-out of the counter of the receiver's internal 5 MHz reference oscillator.
3. An indication on the signal strength of the 150 MHz and 400 MHz signals. Three cases are discerned per signal: high signal to noise ratio, low signal to noise ratio and phase lock loss during the count period.
4. The 400 MHz (f_2) and 150 MHz (f_1) Doppler phase counts (Dc) are given. The 150 MHz Doppler phase counts are scaled up to the 400 MHz counts (i.e. multiplied by 8/3). The receiver has multiplied these counts by 64, to increase the read-out precision from one cycle to 1/64 of a cycle.

The data processing programs compute the satellite positions from the transmitted orbital parameters. They subtract the 400 MHz Doppler phase count from the 150 MHz Doppler phase count. This is the so called differential Doppler phase count (dDc), which equals $64/2\pi$ times the differential Doppler phase from equation (2.22):

$$dDc = Dc_{150} - Dc_{400} = \frac{64}{2\pi}\Delta\phi \,. \tag{2.23}$$

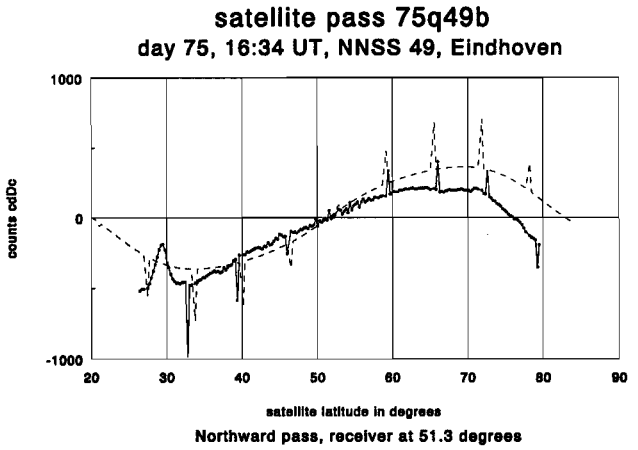

Figure 2.1: An example of a satellite pass registration. Satellite latitude is on the horizontal axis, counts (cdDc) on the vertical axis. The count is proportional to the change in TEC over the integration interval. The uninterrupted curve is a real measurement, the interrupted curve is a simulated pass over a purely stratified ionosphere. See the text for further explanation.

Because only *changes* in phase can be measured, this differential Doppler count has an arbitrary zero level. In fact, the receiver really measures the increase of the phase counts over an integration interval. Thus we arrive at the change in differential Doppler count ($cdDc$):

$$cdDc = dDc_{end} - dDc_{begin} \ . \tag{2.24}$$

This cdDc (or just count for short) is our basic unit. It eliminates the need to use an unknown integration constant. It is also very convenient to express the system's accuracy in this unit. The change (Δ TEC) in TEC over every integration interval is proportional to this count. This Δ TEC is what we call differential TEC. When we fill in the numbers from (2.22) and (2.23) we get

$$\Delta\text{TEC} = 7.61 \times 10^{12} cdDc \ . \tag{2.25}$$

The uninterrupted curve in figure 2.1 is the registration of a satellite pass. The figure may be a bit confusing, since it gives the raw (differential) TEC data. The figure would be easier to interpret if we had followed the convention and plotted relative TEC, which is the integrated differential TEC. Because it is an intermediate result anyhow, we choose to represent the data such as they are fed to the tomographic reconstruction algorithm. Every 25 data points there is a peak. The peaks correspond to data points with integration time of 9.6 instead of 4.6 seconds, which results in higher counts. The time interval between two peaks is 2 minutes. This specific satellite pass is to the north, and time goes from left to right. A southward pass would give the same curve, reflected in the horizontal axis. As the satellite approaches the observer (left half) the intersection of the line of sight with the ionosphere shortens, and therefore the integrated electron density decreases. As a result, $\Delta TEC < 0$ and the count is negative. As the satellite is close to its nearest point of approach (at the receiver's latitude

51.3°), the count is zero, and when the satellite recedes, the count is positive. The bump in the figure at 29° latitude corresponds to a dip in electron content.

The interrupted curve in the figure is an example of a simulated pass over a purely stratified ionosphere. The simulated pass goes from horizon to horizon (zero elevation), whereas the real pass is only registered at elevations larger than zero.

To give an idea of how the data are stored, the first lines of the file that contains the data of the satellite pass of figure 2.1 follow below. Files like these are fed to the tomographic reconstruction program without further processing:

```
  This is a real TEC data file
75 16:36:29  1234 8 250 1010 35 035603461834064   pass header
  16 34                          lock on time UT
T                                differential TEC data
Eindhoven                        station name
   51.2601    5.4919  6365.17    SPHERICAL coordinates station
202                              number of sat positions: rNs = numtec+1

7                                receiver number
NNSS49                           satellite name


   latitude  longit.  radius     cnts quality elev azimuth
                                      indicts

   26.2694   10.3737  7538.12       0   0  0   8.0 170
   26.5238   10.3544  7538.17    -520 339  1   8.3 170
   26.7783   10.3350  7538.21    -507 339  1   8.7 170
   27.0327   10.3157  7538.25    -508 339  1   9.0 170
   27.2872   10.2964  7538.29    -500 339  1   9.3 170
     .         .        .          .   .  .    .   .
```

The first three columns give the position of the satellite in spherical coordinates (degrees and kilometers). In the last columns, elevation and azimuth (degrees) give apparent position of the satellite as seen from the receiver. The counts bear to the difference in TEC: the TEC along the line of sight from the satellite location to the receiver minus the TEC from the preceding satellite position. That explains why there is no count in the first line. Every line corresponds to a 4.6 seconds integration interval. In this period, satellite latitude increases with a quarter degree.

The first two digits of the column with quality indicators give the signal strength (3: high signal to noise ratio), the third digit represents the number of digits of the satellite orbital elements that were received well (should be 9). These three digits indicate the quality of reception, 339 stands for maximum quality. If there is doubt to the correctness of the count itself (count too high or very abrupt changes in the count) the data processing program give 0 instead of 1 in the next column. If the quality indicators do not equal 339 -1, the data point will not be used in the tomographic reconstruction program. This will happen when there is scintillation, when there is interference with man-made noise (which happens quite often at 150 MHz), or when the signal becomes too weak at the end of the pass.

2.9 Calibration

We know what the receivers measure and how to compute differential TEC from the raw data. We also know on what grounds to reject a measurement. We do not yet know the accuracy of the measurements. To get an idea of the precision and stability of the receivers, we installed all antennas on the roof of the Physics Department and tested all receivers simultaneously. Two receivers did not generate any output, these were obviously out of order. We recorded and compared the output of the six remaining receivers in the months February and March of the year 1995, on an on-and-off basis.

To study the effect of antenna or internal oscillator inaccuracies, we connected two different receivers to one antenna or to one 5 MHz reference oscillator (or both). We did not expect that an offset of the local oscillator would produce errors, for the following reason. Harmonics of the internal 5 MHz signal are mixed with the incoming signals to extract the Doppler frequencies (these harmonics are thus subtracted from the incoming signal). A frequency drift of the reference oscillator therefore produces an error in the Doppler counts. The differential Doppler technique uses the *difference* between these counts. The differential procedure cancels a frequency offset of the local oscillator.

Of all simultaneous differential counts, the median value was supposed to represent the correct number. Statistics of the differences from this median give an idea of the accuracy of the receivers. In these tests, only those data points with prime quality indicators are compared. The results of the tests are the following:

1. The discrepancy between the Doppler counts of two receivers, is greatly reduced when they are both connected to the same 5 MHz local oscillator. The discrepancy in differential Doppler count, which scales with Δ TEC, is not reduced (as foreseen above). Therefore, an offset of the internal oscillator does not affect the accuracy of the data.

2. The difference between two receivers' counts is not reduced when they are both connected to the same antenna. Therefore, the major source of error is in the receiver rather than in the antenna.

3. The errors of the receivers are comparable in size.

4. The error in the differential count is independent of the value of the differential count. Therefore we speak of an absolute error rather than a relative error, or 'white noise'.

5. The error has a two sided exponential error distribution. This distribution is given by

$$ED(x) = \frac{1}{\sqrt{2}\sigma} e^{\frac{-\sqrt{2}}{\sigma}|x-\mu|} \tag{2.26}$$

where μ is the mean and σ is the standard deviation. In figure 2.2, we see the result of a satellite pass where 913 data points were compared. Statistics gave a mean error of $\mu = 0.04$ counts and a standard deviation of $\sigma = 5.68$ counts. The curve drawn is the distribution function ED with $\mu = 0$ and $\sigma = 5.68$. A Gaussian distribution with these parameters is not sharp enough around zero and falls off too quickly at the edges. Other passes give similar results. Therefore, we state that the error has a two sided exponential distribution with mean $\mu = 0$ counts and standard deviation $\sigma = 6$ counts. This corresponds to an error of $\sigma = 5 \times 10^{13}\mathrm{m}^{-2}$ in differential TEC.

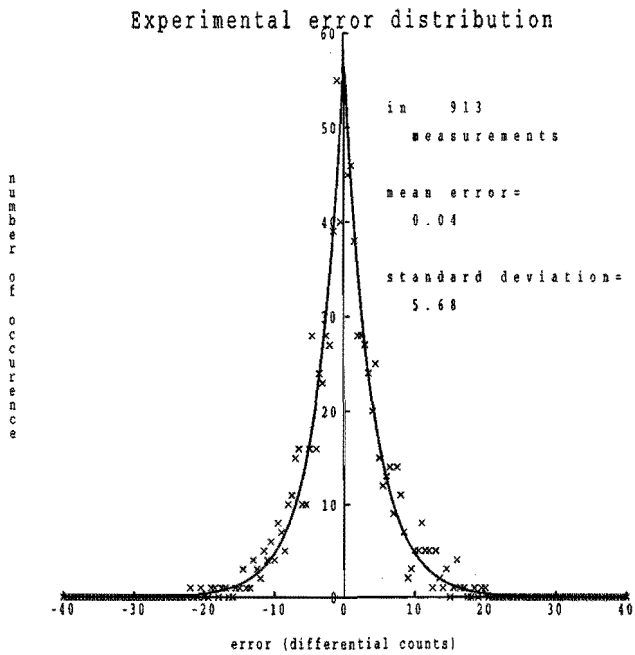

Figure 2.2: The distribution of the measurement errors in the differential counts. The curve is a two sided exponential distribution with mean $\mu = 0$ and standard deviation $\sigma = 5.68$.

Chapter 3

Tomography and inverse problems

An understanding of tomography requires insight in inverse problems, a class of problems tomography is part of.

3.1 About tomography

In many applications, people feel the need to examine the internal structure of an object without opening it. Physicians want to see inside the human body and geologists yearn for a cross-section of the earth. For various reasons, they cannot afford to make many openings in the object. The ensemble of non-invasive techniques to make these cross-sections goes by the name tomography. The word comes from the Greek noun $\tau o \mu \eta$, which means slice.

All tomographic techniques make use of waves. The waves can be electromagnetic or acoustic in origin. They can be emitted, absorbed, transmitted, reflected, refracted and diffracted, or combinations of these, by structures inside the object. Therefore, we speak of emission, transmission, reflection and diffraction tomography. In all cases, waves from many propagation directions must be observed. The more viewing directions, the better the reconstruction of the object. In short, tomography images the internal structure by looking from many directions through the object.

Under certain conditions, wave propagation is almost along straight lines, or straight rays. The most important of these conditions is that the object does not change much over one wavelength. The conditions are generally satisfied for short wavelengths. When the straight ray approximation applies, the description of wave propagation is greatly simplified and so is tomography. There is another advantage of propagation along straight rays. It is then possible to consider propagation in isolated slices of the medium. Therefore, we can reconstruct isolated cross-sections of the object. This is tomography in the classical sense. It has become famous by its medical application in the CT (computerized tomography) scanner (see figure 1.4). These two simplifications made, tomography is mathematically equivalent to the reconstruction of a two dimensional function from its line integrals. This process is described by the inverse Radon transform, which will be discussed in section 3.3.

At longer wavelengths, those of radio and acoustic waves for example, the straight ray approximation may not be valid. However, something of the simplicity of straight line tomography can be conserved when the wave propagation goes along (curved) rays. This approach is applied in the imaging of the earth's interior (Spakman 1993), where the rays are calculated

by ray tracing. The concept of rays is formulated by the geometrical optics approximation, which we have discussed in section 2.4. When the wavelength is too long for the geometrical optics approximation, diffraction effects have to be accounted for, and the ray concept breaks down. This is the domain of diffraction tomography, which, for example, finds an application in the oil industry as the so-called well-to-well tomography (Devaney 1984).

When wave propagation is not along straight lines, the propagation is generally not confined to a plane. By consequence, it is impossible to consider isolated slices. This implies that the measurement and the reconstruction techniques become much more cumbersome. Besides, the name tomography becomes a misnomer. Yet, if the symmetry of the object allows, there is a possibility to confine measurements and reconstruction to a slice. If the object can be assumed not to vary in a certain direction, isolated cross-sections perpendicular to this direction can be made. When this symmetry assumption cannot be made, and when the data collection is insufficient to reconstruct the three dimensional object, it may still be possible to infer some of its statistical properties. This is called statistical tomography.

In its present form, tomography of the ionosphere uses radio waves with a wavelength of 2 meters or less. We have shown in section 2.4, that the straight ray description suffices under these conditions. Therefore, the remainder of this thesis will be concerned with straight line tomography only.

In the experiment, the lines of straight line tomography correspond to rays. The line integrals, which are the experimental data, correspond to a change in amplitude or phase of the waves that propagate along these rays. The integrand can be one of three quantities: the object's emissivity, its absorption coefficient, or its phase slowness (inverse of phase speed). The former two work on the amplitude, the latter on the phase of the wavefield. Tomography thus enables the internal imaging of absorbing objects, of emitting objects and of phase objects. Let us give an example of each of these.

1. Absorbing objects

   The most famous application of straight line tomography is the medical CT scanner (for a review see Herman, 1980). In such a device, an X-ray source moves around the patient. The machine measures the X-ray attenuation of the radiation along many lines in a plane through the patient. The attenuation scales with the natural logarithm of the absorption coefficient integrated along the line of sight. The tomographic reconstruction generates an image of the absorption coefficient; this picture is a cross-section of the patient.

2. Emitting objects

   In a variant of the CT scan, the X-ray absorbing patient is replaced by somebody with features that are made γ-ray emitting. This is accomplished by administration of radioactive isotopes bound to organic molecules that preferentially gather in interesting areas. The radiation propagates in straight lines and is not absorbed by the patient. The outcoming radiation is measured all around the patient and the final picture renders the patients emissivity. This technique is called positron emission tomography, or PET.

3. Phase objects

   A phase object is a transparent object, such as a piece of glass, in which the phase speed differs from that in vacuum. The phase speed traces the spatial structure of the object.

Because phase can only be observed by indirect methods, such as interference, phase objects can be imaged by special tricks only. One such instrument is the phase contrast microscope by Zernike, which makes transparent living cells visible. The ionosphere is another example of a phase object. The free electrons in the ionosphere change the phase speed of radio waves. In chapter 2, we have demonstrated that the phase shift of a carrier wave that has propagated through the ionosphere, scales with the integrated electron density along the line of sight. The inversion gives a picture of the electron density distribution in a slice of the ionosphere.

3.2 Inverse problems

Tomography is part of the class of inverse problems, which is distinct from the class of direct problems. Both types of problems deal with the state of an object, on the one hand, and with an experiment, or a set of observations, on the other. Of course, the state of the object and the outcome of the experiment are related by the laws of physics. These laws are presumed to be known.

The direct problem is a matter of explanation: given the state of the object, explain or predict the outcome of the experiment. This is the problem computational physicists are concerned with. The direct problem follows the natural order of cause and effect.

The inverse problem is a matter of inference: what can we say about the state of an object from the observation or the experimental data? Here the order is reversed: deduce the cause from the effect. It is clear that the direct problem must be well understood, before attempts to solve the inverse problem can be made. In tomography, the unknown state is the two dimensional distribution and the experimental data correspond to the line integrals.

In tomography, the inverse problem is equivalent to finding a solution to a set of integral equations. Another type of inverse problem needs a solution to a set of partial differential equations. In both cases physics determines the shape of the equations. The experimental data give the values of the integrals in the first case and the initial and boundary conditions in the latter.

The problem with inverse problems is that they are often ill-posed. A problem is ill-posed, if it has one of the following properties:

1. a solution does not exist, or
2. the solution is not unique, or
3. the solution is very sensitive to small changes in the input, i.e. it is unstable.

The first characteristic seems inappropriate to inverse problems, because we know that there exists a solution, namely the state of the object we observe. Due to measurement errors, however, the approximate mathematical formulation of the problem may have no solution. The second and third properties are related and come into play when the experimental data contain too little information to deduce the desired information on the state. As a consequence, the solution to the inverse problem is either not unique or extremely sensitive to small variations in the data. Of all three, the third property is the most venomous.

In general, it is impossible to give the true solution to an inverse problem. The best that can be hoped for, is a solution that is consistent with the experimental data and that is useful. Therefore, a solution that satisfies one user may not do for another.

As an illustration, consider a navigator of a yacht that leaves the harbour. There is a lighthouse on the pier and nearby is an airstrip with a light that is illuminated when a

plane is approaching. On board there is a chart on which these beacons are indicated. After a few hours of nice sailing the sun has set and the captain asks the navigator where they are. To determine the position, the navigator takes a compass bearing on the lighthouse, i.e. he determines its azimuth. The navigator sets to solve an inverse problem: determine the position from the bearing. On the chart, he draws a line through the lighthouse with the same bearing. The ship is somewhere on that line, but the navigator does not know where. The problem is underdetermined and the solution is not unique.

The captain is very dissatisfied. Over the skipper's grunts the navigator hears a plane approaching. He is very relieved and he hurries to take a bearing on the airstrip beacon. Again he draws a line on the chart. The intersection of the two lines is the position. But because the lighthouse and the beacon are so close (say a mile apart), the two lines make a very small angle (say 5^0). He sees immediately that a small error in one of the bearings gives a large error in position. As the azimuth is difficult to measure, say with a precision of $2^0.5$, the distance to the harbour may be anything between 7 and 23 miles. The position fix is very sensitive to small errors in the bearings. The problem is ill-posed.

Luckily, the navigator has some extra information that he can use to give a more satisfying estimate of position. He knows they have been sailing for three hours. Because the helmsman assures him that the log has never indicated a speed under 4 miles per hour, nor a speed over 5 miles per hour, he can be sure he is somewhere between 12 and 15 miles from the harbour. The navigator draws two circles of radius 12 and 15 miles and centered on the harbour entrance. His position is between the circles and on the line he had drawn before. This estimate is precise enough to appease the captain.

The general approach to overcome the third and nastiest trait of ill-posed problems, the instability of the solution to small changes in the data, is called regularization. Turchin et al (1971) review the origins of regularization in the solution of incorrectly posed problems, as they call them. The concept of regularization was proposed by Tikhonov in 1963. The idea is to use a priori information to damp the wild behaviour of the solution. The a priori information is cast in a (semi)norm in the solution space. The lower this norm, the more probable the solution in the a priori sense. The weight of this prior norm in the algorithm is indicated by the regularization parameter α, which can be seen as a measure of the importance of the regularization. If regularization is applied in a correct manner, the solution to the inverse problem must approach the true solution when $\alpha \to 0$ and the measurement errors vanish. This is what we will call Tikhonov's criterion.

Another way to look at regularization comes from Bertero et al (1980):

> 'The role of the prior knowledge is to discriminate between interesting solutions and spurious solutions generated by uncontrolled propagation of data errors. The principle of regularization methods is to include the additional conditions explicitly, at the start, instead of resorting consciously or not, during the computations, to some tricks eliminating the instability. The essential drawbacks of such apposite tricks is indeed that their implications, on the class of admissible solutions, often remain in the dark.'

This is what we will refer to as Bertero's criterion, namely to include the prior information explicitly, before the calculations are started. This criterion forces the inverse problem solver to be precise in the mathematical prescription of the solution. The use of Tikhonov's regularization parameter indeed forces the researcher to meet Bertero's criterion.

Continuous inverse theory Transform methods	**Discrete inverse theory** Series expansion methods
1. Rewrite $\mathcal{A}f = \boldsymbol{d}$ to $\mathcal{T}f = d$, where d is the data function whose arguments come from a continuum of real numbers.	1. Find a discretization where $f \approx \sum x_j b_j$. Here the b_j form a finite set of basis functions and the x_j form a set of coefficients.
2. Solve for the unknown function by producing an inversion formula $\mathcal{T}^{-1}$.	2. Rewrite $\mathcal{A}f = \boldsymbol{d}$ to $A\boldsymbol{x} \approx \boldsymbol{d}$,where A is a matrix and $\boldsymbol{x}$ a vector with coefficients.
3. Adapt the inversion formula for application to discrete and noisy data.	3. Solve the system of linear algebraic equations $A\boldsymbol{x} \approx \boldsymbol{d}$.
fast inflexible needs good and even data sampling	slow versatile can do with poor and uneven sampling

Table 3.1: The two basic approaches to inverse problems, see the text for a further explanation.

The navigator's problem from above is not a linear problem, because the geographical coordinates of the yacht are not a linear function of the compass bearings. The ill-posedness, however, is not a property unique to non-linear problems. As we will see later, linear inverse problems can have unstable solutions as well. In section 3.3, we will show that tomography is a linear problem, and for that reason we will focus on linear inverse problems and their regularization in the remainder of this thesis.

The navigator's problem is quite simple, he has to determine the yacht's position only, which is rendered by three coordinates. The fact that he can, in principle, determine his position from only two observations, is the result of the implicit use of another piece of prior information: the yacht must be on the surface of the globe. This reduces the number of independent coordinates to two. Anyhow, the navigator has the easy job to determine only a few coordinates. In many other inverse problems, the number of unknown quantities is infinite. Such is the case in tomography, where a function of two smoothly varying coordinates must be reconstructed from a finite set of measurements.

This illustrates what we have already said about the reason for the ill-posedness of many inverse problems: the experiment does not pass all information to the observer. The loss of information is quite general: most states can be described by an infinite number of parameters only, whereas the experiment only provides a finite set of data points. The finiteness is the result of sampling. This discrepancy (finite vs. infinite) causes the information deficit that makes the problem an ill posed problem. There are basically two strategies to reconcile the

finiteness of the experimental data set with the infinite number of parameters of the unknown state. In the first approach we start by pretending that the data set is complete and therefore effectively infinite. In the end, we try to allow for the finiteness of the number of data points. This is continuous inverse theory. In the second approach we accept the finiteness of the data set, right from the start. We try to find a limited set of parameters describing the solution. This is discrete inverse theory. This distinction was used in the review articles by Lewitt (1983) and Censor (1983). We will continue the chapter with three subsections that describe and compare the two approaches, which are summarized in table 3.1. Before we do so, we must give a formal description of the situation:

The direct problem is linear, or linearized, and should be well understood. It is described by the linear operator $\mathcal{A}$. Because we understand the direct problem, we know $\mathcal{A}$. The direct problem corresponds to an experiment that is described by

$$\boldsymbol{d} = \mathcal{A}f \ . \tag{3.1}$$

Here f is a distribution representing the state, its arguments come from a continuum of real numbers. $\boldsymbol{d}$ is a vector containing the data points d_i, and $d_i = \mathcal{A}_i f$. In the direct problem, $\mathcal{A}$ and f are known and $\boldsymbol{d}$ must be calculated, which is straightforward. In the inverse problem, $\mathcal{A}$ and $\boldsymbol{d}$ are known and f must be found.

3.2.1 Continuous inverse theory

In continuous inverse theory, both the data and the state are treated as distributions whose arguments come from continua of real numbers. The reconstruction methods that result from this strategy are called transform methods. These methods follow a recipe of three steps:

1. Pretend that the data are known perfectly. This means that there is supposedly no loss of information due to measurement errors or to the finiteness of the sampling. The data vector $\boldsymbol{d}$ is replaced by the function d, which is a transform $\mathcal{T}$ of the distribution describing the state: $d = \mathcal{T}f$.

2. Find the inverse transform $\mathcal{T}^{-1}$. Many algorithms make use of transforms with inherent basis functions, such as the goniometrical functions $\sin x$ and $\cos x$ in the Fourier transform. This can lead to confusion when comparing these methods to the methods in discrete inverse theory. The major difference is, however, that the transform methods (implicitly) use an infinite number of basis functions.

3. Adapt the inverse transform so that it can work on discrete data with measurement errors. This is the moment to try and put in the prior information.

In the second step, there may be several inversion formulae, which are mathematically equivalent. When these formulae are discretized in step 3, it is found that the algorithms do not perform identically on noisy and discrete data. This is the result of the different approximations in step 3.

3.2.2 Discrete inverse theory

In discrete inverse theory, both the data and the state are treated as discretized distributions. Its reconstruction methods are called series expansion methods and these methods follow a recipe that also consists of three steps:

1. Assume that the state f is well described by a discretized function

$$f \approx \sum_{j=1}^{m} x_j b_j \ . \tag{3.2}$$

Here b_j is a finite set of orthogonal basis functions, and x_j a set of coefficients. Both output and input of the inverse problem are now represented by a finite set of numbers. This finiteness is essential. If the number of basis functions were allowed to go to infinity, the discretization of f would only be apparent.

2. Rewrite the problem to a matrix equation. First rewrite $d_i = \mathcal{A}_i f$ by

$$\mathcal{A}_i f \approx \mathcal{A}_i \sum_{j=1}^{m} x_j b_j = \sum_{j=1}^{m} \mathcal{A}_i x_j b_j = \sum_{j=1}^{m} x_j \mathcal{A}_i b_j = \sum_{j=1}^{m} x_j a_{i,j} \ . \tag{3.3}$$

Here we have first used the orthogonality of the basis functions and then the linearity of $\mathcal{A}$. It follows that

$$\boldsymbol{d} = \mathcal{A} f \approx A\boldsymbol{x}, \tag{3.4}$$

where A is a matrix with coefficients $a_{i,j}$ given by

$$a_{i,j} = \mathcal{A}_i b_j \ . \tag{3.5}$$

3. Solve the system of linear algebraic equations $A\boldsymbol{x} \approx \boldsymbol{d}$. In this system, every equation corresponds to a measurement and the unknowns are the coefficients of the solution.

Both in the first and last step, the inverse problem solver has the opportunity to put in his prior knowledge. In the first step, the basis functions can be chosen so as to reflect properties of the state, such as symmetry. When the basis functions are well chosen, its number can be reduced. This eases the instability. In the last step, the additional information can be used to solve the system of equations, as we will show in section 3.5.

For an example of discretization in inverse problems, we turn to tomography. In (straight line) tomography, the operator $\mathcal{A}_i$ integrates the two dimensional distribution over the line with index i. Let the distribution be discretized by the pixel representation. In this representation, the basis functions $b_j(x, y)$ are very simple, if the point (x, y) falls in the j^{th} pixel, then $b_j(x, y) = 1$. If it does not, then $b_j(x, y) = 0$. Because the basis functions are so simple, the elements $a_{i,j}$ of matrix A have a straightforward interpretation. As is clear from (3.5), $a_{i,j}$ is the length of the intersection of ray i with pixel j. Because a line of sight intersects only a fraction of all pixels, A is a sparse matrix.

3.2.3 Comparison

The dissimilarities in the two approaches are reflected in the properties of the algorithms. There are three major differences.

1. Speed

It is justified to say that transform methods give an analytical solution, while the series expansion methods find a numerical solution, although both methods use a computer to produce an approximate solution. By consequence, algorithms from continuous inverse theory require less computer time than their competitors from discrete inverse theory.

2. Versatility

   Because systems of equations are much easier too manipulate than analytic transforms, the series expansion methods are much more versatile than the transform methods. This versatility comes in handy when prior knowledge must be included in the algorithm. The versatility also permits weighting of individual measurements (equations), when the quality of data points differ. The versatility will be called upon yet another time. As we will see in section 4.1.1, the measurements in ionospheric tomography are not absolute but they have a differential nature. The series expansion methods can easily cope with this complication.

3. Sampling

   It is evident from step 1, that the transform methods need good sampling of the data. Furthermore, most practical implementations of transform methods require sampling at regular intervals (even sampling). By contrast, series expansion methods do not need even sampling. Moreover, these methods can more easily compensate the loss of information due to poor sampling.

These different properties have consequences for the applicability of the methods. Continuous inverse theory is the method of choice, when there are abundant data of good quality. Such is the case in most medical applications. When the data are incomplete and noisy, as in geophysical experiments, the approach of the discrete inverse theory is more suitable. Tomography of the ionosphere is an example of such a geophysical experiment.

3.3 The Radon transform and its inverse

In the previous section, we have stated that inverse problems can be solved by two different strategies. In this section, we review some of the transform methods from continuous inverse theory, that solve the tomography problem. Because we do not use transform methods in this thesis, the reader may skip this section and continue at 3.4, without risk of loosing the thread of the argument.

In section 3.1, we have seen that straight line tomography is equivalent to the reconstruction of a distribution from its line integrals. This section will start with a formulation of the Radon transform, which is the mathematical description of straight line tomography. The discussion will continue with the inverse Radon transform. This inverse can be formulated in different ways that are mathematically equivalent, but that give different results when applied in practice. We will give three such versions and shortly discuss their merits in practical applications. The formulae will be presented without proof and without mathematical rigour. It is implicitly assumed that all functions satisfy conditions which permit that the operations can be performed. For proofs, the reader is referred to the textbooks by Deans (1983) and by Kak and Slaney (1988).

3.3.1 The Radon transform

The Radon transform is the mathematical description of the direct problem. In the left half of figure 3.1, we see the two dimensional object described by the distribution $f(x, y)$. Fifteen parallel lines are drawn with coordinates (p, ϕ), where p is the line's distance to the origin and ϕ the angle it makes with the x-axis. The line integral of the function over the line is

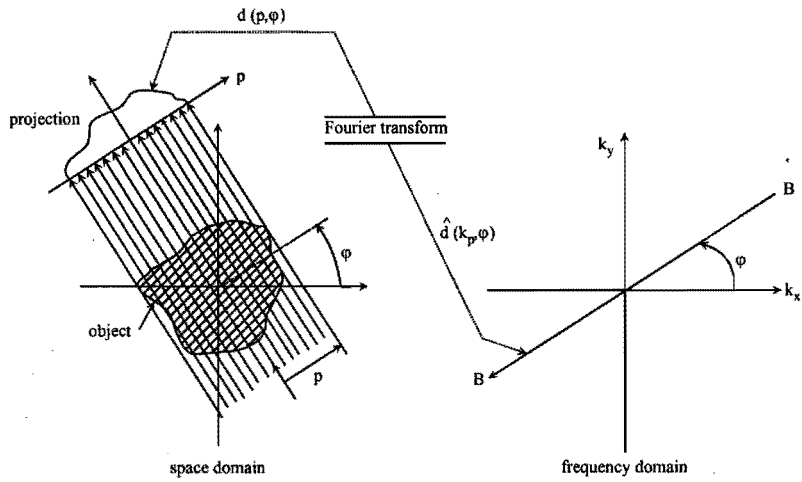

Figure 3.1: The left half shows the geometry of the Radon transform. Together, both halves illustrate the Fourier slice theorem. The 1-dimensional Fourier transform ($\hat{d}$) of the projection data (d) forms a slice (B-B) of the 2-dimensional Fourier transform ($\hat{f}$, not drawn) of the original object (f). From Kak and Slaney (1988).

indicated by $d(p,\phi)$, and $d(p,\phi)$ is called the Radon transform of $f(x,y)$. The sampling of $d(p,\phi)$ constitutes the experimental data. Let us parametrize the line (p,ϕ) with t:

$$\begin{aligned} x &= p\cos\phi - t\sin\phi \,, \\ y &= p\sin\phi + t\cos\phi \,. \end{aligned}$$

Then the Radon transform is given by

$$d(p,\phi) = \int_{-\infty}^{\infty} f(p\cos\phi - t\sin\phi, p\sin\phi + t\cos\phi)\, dt \,. \tag{3.6}$$

It is clear that the Radon transform is a linear transform, i.e. the mapping form f to d is a linear mapping. The Radon transform can be seen as a (linear) Fredholm integral equation of the first kind:

$$d(p,\phi) = \int\int K(p,\phi,x,y)\, f(x,y)\, dx\, dy \,. \tag{3.7}$$

In this equation, each of the coordinate pairs (p,ϕ) and (x,y) should be replaced by a single coordinate, to simplify comparison with the literature on Fredholm equations. The function K is the kernel. In tomography, K is the two dimensional Dirac delta function: $\delta(p - x\cos\phi - y\sin\phi)$, which is non-zero on the line (p,ϕ) only. It is well known that the numerical solution of a Fredholm integral equation of the first kind is unstable. In fact, it is often a disaster (Arfken & Weber, 1995). It is so, because it is an ill-posed problem.

Let us turn our attention again to the left half of figure 3.1, where we see what is called a projection. A projection is a subset of the data $d(p,\phi)$ in which the lines are parallel (ϕ is constant). That is the reason why the Radon transform is sometimes said to deal with

image reconstruction from projections. A powerful and illustrative theorem in the theory of the inverse Radon transform is the Fourier slice theorem, which works in the Fourier space. Let us first consider the two dimensional Fourier transform of the function f:

$$\hat{f}(k_x, k_y) = \int_{-\infty}^{\infty} \int_{-\infty}^{\infty} f(x, y) e^{-2\pi i(xk_x + yk_y)} \, dx \, dy \ , \tag{3.8}$$

and the one dimensional Fourier transform of the data in a projection:

$$\hat{d}(k_p, \phi) = \int_{-\infty}^{\infty} d(p, \phi) e^{-2\pi i p k_p} \, dp \ . \tag{3.9}$$

Here k_x, k_y and k_p are coordinates in Fourier space. Now $\hat{f}$ and $\hat{d}$ are related by a theorem called the Fourier slice theorem, or the projection slice theorem:

$$\hat{d}(k_p, \phi) = \hat{f}(k_p \cos\phi, k_p \sin\phi) \ . \tag{3.10}$$

See Lewitt (1983) for a proof and figure 3.1 for an illustration. The Fourier slice theorem implies that the Fourier transform of a projection of the original distribution is the same as a slice (B-B in the figure) through the two dimensional Fourier transform of the original distribution. As a consequence of this theorem, an inversion of the Radon transform can be obtained by integrating three times: once to transform the data d to $\hat{d}$, and twice to transform $\hat{f}$ to f. The discussion now elaborates on the inverse Radon transform, of which we will present three formulations.

3.3.2 Reconstruction by Fourier inversion

The method suggested above, which is a direct application of the Fourier slice theorem, is called reconstruction by Fourier inversion. Taking the inverse Fourier transform of (3.9), gives (Lewitt 1983):

$$f(x, y) = \int_{-\infty}^{\infty} \int_{-\infty}^{\infty} \hat{d}(\sqrt{k_x^2 + k_y^2}, \arctan \frac{k_y}{k_x}) \, W(\sqrt{k_x^2 + k_y^2}) \, e^{2\pi i(xk_x + yk_y)} dk_x dk_y \ . \tag{3.11}$$

Here W is a window function that equals unity ($W = 1$) in the analytical inversion. In numerical implementations, W can be chosen differently to mitigate the effects of aliasing. This algorithm requires interpolation in the Fourier domain to go from a polar grid (k_p, ϕ) to a Cartesian grid (k_x, k_y), before the inverse Fourier transform can be calculated.

3.3.3 The filtered backprojection

In another approach, the three integrations of the direct Fourier inversion are evaluated differently. The (k_x, k_y) coordinates are exchanged for polar coordinates, the order of integration is changed and use is made of the property

$$d(-p, \phi) = d(p, \phi + \pi) \ . \tag{3.12}$$

After some algebra, this filtered backprojection arrives at a procedure with three successive integrations (3.15), (3.14) and (3.13). The backprojection is evaluated by

$$f(x, y) = \int_0^{\pi} \tilde{d}(x \cos\phi + y \sin\phi, \phi) \, d\phi \ , \tag{3.13}$$

where the filtering is represented by the convolution

$$\tilde{d}(p', \phi) = \int_{-\infty}^{\infty} d(p, \phi)\, q(p' - p)\, dp\,, \tag{3.14}$$

where the filter is given by $\hat{q}(k_p) = |k_p| W(k_p)$ or

$$q(p) = \int_{-\infty}^{\infty} |k_p| W(k_p) e^{2\pi i p k_p} dk_p\,. \tag{3.15}$$

The window function, W, is unity ($W = 1$) for the analytical inversion. In real world applications, W should be chosen differently to reduce unwanted aliasing. The last integral (3.15) has to be computed only once and can be reused in the other reconstructions. In the step called backprojection (3.13), the value of f at a certain point is found by summing all filtered line integrals $\tilde{d}$ from lines through that point.

3.3.4 The inverse Radon transform

The last method we discuss, begins with the same moves as the filtered backprojection algorithm: change of coordinates, change of order of integration and use of (3.12). Then the p-integration is performed by parts. This introduces a partial derivative ($\partial/\partial p$), while it does not reduce the number of integrations, because the integral over p cannot be evaluated. This only seems to complicate things, but it permits calculation the integral over k_p (Junginger and van Haeringen, 1972). The result is an inversion formula, with one partial derivative and two integrations,

$$f(x, y) = \frac{-1}{2\pi^2} \int_{-\pi/2}^{\pi/2} \int_{-\infty}^{\infty} \frac{1}{p - x\cos\phi - y\sin\phi} \frac{\partial d(p, \phi)}{\partial p}\, dp\, d\phi\,. \tag{3.16}$$

Here, the Cauchy principal value of the integral over p is understood. This formula is known as the inverse Radon transform, which was discovered by Radon in 1918 (see Deans, 1983, for a discussion and a translation of the original paper by Radon). The main disadvantage of the inverse Radon transform in practical applications, is the partial differentiation $\partial d(p, \phi)/\partial p$. As the function d is known approximately at some discrete sampling points only, the differentiation will greatly magnify the measurement errors. This makes the method unstable.

3.3.5 Comparison of transform methods

We can conclude that the inverse Radon transform exists and can be computed, when all line integrals are known. All transform methods presented here are linear methods. This is no surprise, since the Radon transform is linear as well. All methods require some kind of interpolation.

For most practical applications, the inverse Radon transform (3.16) is too sensitive to measurement errors. Of the other two, the filtered backprojection is by far the most popular in medical CT scanners. The method is faster than direct Fourier inversion, as only two instead of three integrals have to be calculated. Filtered backprojection does not need the additional interpolation in Fourier space, which the other method does.

An interesting feature of the methods is the option to choose a filter W. From experience, the user can choose the filter that works best with the problem at hand. The filter regularizes the problem.

A is a $m \times n$ matrix (m rows and n columns)			
A is of full rank $\mathrm{rk}(A)=\min(m,n)$			A is rank deficient $\mathrm{rk}(A)< \min(m,n)$
$m > n$ $rk(\mathrm{A}) = n$	$m = n$ $\mathrm{rk}(A) = m = n$	$m < n$ $\mathrm{rk}(A) = m$	m, n unordered $\mathrm{rk}(A) < \min(m,n)$
A^{-1} does not exist	A^{-1} exists	A^{-1} does not exist	A^{-1} does not exist
$A^{-g} = [A^t A]^{-1} A^t$	$A^{-g} = A^{-1}$	$A^{-g} = A^t [A A^t]^{-1}$	$A^{-g} = V D^{-g} U^t$
$A^{-g} A = I_n$ $A A^{-g} \neq I_m$	$A^{-1} A = I_n$ $A A^{-1} = I_m$	$A^{-g} A \neq I_n$ $A A^{-g} = I_m$	$A^{-g} A \neq I_n$ $A A^{-g} \neq I_m$
$A\boldsymbol{x} = \boldsymbol{d}$ is overdetermined	$A\boldsymbol{x} = \boldsymbol{d}$ is evendetermined	$A\boldsymbol{x} = \boldsymbol{d}$ is underdetermined	$A\boldsymbol{x} = \boldsymbol{d}$ is mixeddetermined
$\boldsymbol{x} = A^{-g}\boldsymbol{d}$ minimizer of misfit $= \|A\boldsymbol{x} - \boldsymbol{d}\|$ least squares (LS) solution	$\boldsymbol{x} = A^{-1}\boldsymbol{d}$ exact solution	$\boldsymbol{x} = A^{-g}\boldsymbol{d}$ of all exact solutions, the one with minimal norm $\|\boldsymbol{x}\|$ minimum norm (MN) solution	$\boldsymbol{x} = A^{-g}\boldsymbol{d}$ of all misfit minimizers, the one with minimal norm LS-MN solution

Table 3.2: The generalized solution to a system of equations. A^t represents the transpose of A and A^{-1} stands for the inverse and A^{-g} for the generalized inverse. I_n is the identity matrix of order n.

3.4 The generalized solution

In section 3.2, we have seen that discrete inverse theory reduces the linear(ized) inverse problem to a system of linear algebraic equations. It was also stated that ill-posed inverse problems display one or more of three characteristics: (1) no solution, (2) a non-unique solution or (3) a solution that is extremely sensitive to small variations in the input.

In this section, we will give the so called generalized solution to such a system of equations. This generalized solution circumvents the non-existence and the non-uniqueness, but it is not concerned with the stability. Therefore, the methods of this section will not suffice to solve the inverse tomography problem. In the next section the instability, the third and most venomous characteristic of ill-posed problems, will be tackled by regularization.

Let us recall the system of equations (3.4) to which the inverse problem was reduced:

$$\boldsymbol{d} = A\boldsymbol{x} \ . \tag{3.17}$$

Here the vector $\boldsymbol{d}$ contains the data and the vector $\boldsymbol{x}$ contains the unknown coefficients. A is the coefficient matrix of the system of equations and its elements $a_{i,j}$ are determined by the direct problem and the choice of basis functions. A is a $m \times n$ real matrix, which means that there are m equations (or measurements, data points) and n unknowns (or coefficients); m is set by the experiment or observation and n is determined by the discretization or parametrization of the state. The rank of a matrix is defined as the dimension of the range of the matrix. It equals the number of independent rows in the matrix, which equals the number of independent columns. Matrix A is of full rank when $\text{rk}(A)=\min(m,n)$.

In the following, $\|.\|$ indicates the norm. Although the principles do not depend on the specific choice of the norm, the solution does. The solution is most easily found when we choose the Euclidean norm or the 2-norm, because the equations are then quadratic and the derivatives linear. This explains the expressions 'least squares solution' and 'least squares principle'. The discussion will return to the choice of the norm in section 3.5.7.

Now, the non-existence of a solution to (3.17) is tackled by the minimum misfit principle and the non-uniqueness is circumvented by the minimum norm principle.

1. Minimum misfit principle

   When the system of equations (3.17) is inconsistent, it does not have a solution. In this case, the equal sign (=) should be replaced by a approximately equal sign ($\approx$). The system can be inconsistent as a result of measurement errors, discretization errors, etcetera. Even if there is no true solution, it is still possible to define a best approximate solution, namely the solution that minimizes the misfit. The misfit, or discrepancy, is defined by

   $$\text{misfit} = \|A\boldsymbol{x} - \boldsymbol{d}\| \,. \tag{3.18}$$

   Of course, the misfit of a true solution to (3.17) is zero. The smaller the misfit, the better the approximate solution is supposed to solve the system of equations.

2. Minimum norm principle

   When the system of equations (3.17) is underdetermined, it does not have a unique solution. This is a result of the fact that the data do not contain enough information to specify the solution completely. This problem can be removed by adding extra (a priori) information on the solution. The standard piece of information is that the norm ($\|\boldsymbol{x}\|$) of the solution be small. In some cases, this may be appropriate, for example when the components of $\boldsymbol{x}$ relate to energy content. In other cases it will be less appropriate. Anyhow, the minimum norm principle chooses the solution with minimum norm among all solutions to (3.17). This is the minimum norm solution.

It is possible to say that the generalized solution always employs both principles successively. First, the minimum misfit principle defines a set of best (approximate) solutions. Second, when there is more than one element in this set, the minimum norm principle is used to select one.

The situation that both principles are active, i.e. when the minimum misfit set of best approximate solutions contains more than one element, can only arise if matrix A is not of full rank. When the matrix is of full rank, the minimum misfit and minimum norm principles apply separately and we distinguish three other cases. Here follows a short overview of how the principles apply in the four different cases, which are summarized in table 3.2:

1. Matrix A is of full rank and there are more equations (m) than unknowns (n): $m > n$. A is not square and not invertible. The system of equations is said to be overdetermined. Unless $\boldsymbol{d}$ happens to be in the range of A, the system is inconsistent and has no true solution. The generalized solution is the minimizer of the misfit, which is unique because A is of full rank. This is the minimum misfit solution, or least squares solution when the 2-norm is used.

2. Matrix A is of full rank and the number of equations equals the number of unknowns: $m = n$. The system is evendetermined. A is a square matrix and, since A is of full rank, A is invertible. There is precisely one solution to the system.

3. Matrix A is of full rank and the unknowns outnumber the equations: $m < n$. A is not square and not invertible. The system is underdetermined and because A is also of full rank, there are infinitely many solutions to the system of equations. Of all these, the generalized solution is the one with minimum norm $\|\boldsymbol{x}\|$. This is the minimum norm solution.

4. Matrix A is rank deficient. The system is 'mixed determined'. Unless $\boldsymbol{d}$ happens to be in the range of A, the system is inconsistent. Because A is not of full rank, there are infinitely many points that minimize the misfit. Of all these misfit minimizers, the generalized solution is the one with minimum norm. That is is the minimum misfit - minimum norm solution or the least squares - minimum norm solution:

$$\min_{\boldsymbol{x}\in\mathcal{S}} \|\boldsymbol{x}\|, \quad \mathcal{S} = \{\boldsymbol{x} \in \mathrm{R}^n | \ \min_{\boldsymbol{x}} \|A\boldsymbol{x} - \boldsymbol{d}\| \ \} \ . \tag{3.19}$$

How can these (generalized) solutions be computed? The inverse matrix A^{-1} exists only in the full rank evendetermined case. When we use the Euclidean norm in the minimum misfit and minimum norm principles, there exists a matrix that gives the generalized solution. Such a matrix is called a generalized inverse, A^{-g}, which can be found with the help of the singular value decomposition, or SVD for short.

Every real $(m \times n)$ matrix A can be decomposed by the singular value decomposition. This SVD is a unique decomposition and given by

$$A = UDV^t \text{ , where} \tag{3.20}$$

$$\begin{aligned} U &: \text{ a real } (m \times k) \text{ matrix with orthonormal columns,} \\ D &: \text{ a real } (k \times k) \text{ diagonal positive semidefinite matrix,} \\ V &: \text{ a real } (n \times k) \text{ matrix with orthonormal columns, with} \end{aligned}$$

$$k = \min(m, n) \ . \tag{3.21}$$

Either U or V is a square orthogonal matrix, which means that the transpose equals the inverse. The elements of the diagonal matrix D, are called the singular values of A: sv_i. These singular values are larger than, or equal to zero, $sv_i \geq 0$. The singular values equal the square roots of the eigenvalues of A^tA (if $m \geq n$) or the eigenvalues of AA^t (if $m \leq n$).

When A is of full rank, its singular values are larger than zero, $sv_i > 0$. By consequence, D is invertible where D^{-1} is a diagonal matrix with elements sv_i^{-1}. In this case, it is not hard to proof that

$$A^{-g} = VD^{-1}U^t \ . \tag{3.22}$$

This expression is equivalent to $A^{-g} = [A^t A]^{-1} A^t$, for case 1, or $A^{-g} = A^t [A A^t]^{-1}$, for case 3, as formulated in table 3.2.

If, on the contrary, A is rank deficient, there are singular values that equal zero, and D^{-1} does not exist. Where does that leave us? The power of the SVD is based on the following trick. Consider the diagonal matrix D^{-g} with elements d^{-g}

$$\begin{aligned} d^{-g}{}_i &= sv_i^{-1} \quad \text{if} \quad sv_i > 0 \ , \\ d^{-g}{}_i &= 0 \quad \text{if} \quad sv_i = 0 \ . \end{aligned}$$

Remark that we have replaced $1/0$ by 0, which means that we ignore those parts of the solution that would otherwise be infinite. Isn't that wonderful? With this trick, the generalized solution is given by the generalized inverse $\boldsymbol{x} = A^{-g}\boldsymbol{d}$ and

$$A^{-g} = V D^{-g} U^t \ . \tag{3.23}$$

Proofs of the above can be found in Golub and Van Loan (1989). All that is left to do now, is to find the generalized solution to (3.17), is to compute the SVD. There exist very efficient algorithms (Golub and van Loan 1989) and very efficient routines in various software libraries that do so.

As an illustration, here follows a geometrical interpretation. The solution space is the R^n and every point in this space corresponds to a solution. Every measurement, which is represented by a linear equation in (3.17), corresponds to a hyperplane in solution space. The quadratic form $\|A\boldsymbol{x} - \boldsymbol{d}\| = E$ (with 2-norm) is an ellipsoid in solution space. The centre of the ellipsoid corresponds to the least squares solution of (3.17). The orientations of the ellipsoid's axes are given by the columns of V, and their lengths scale with the inverses of the singular values. The larger the condition number, or the more the singular values differ, the more elongated the ellipsoid. When a singular value is zero, the ellipsoid is degenerated along the corresponding axis, and the ellipsoid's center (the least squares solution) does not exist. The trick of setting $1/0$ to 0, collapses this axis to the point on the axis that is closest to the origin.

Here ends the discussion on the strategies to cope with the non-existence and the non-uniqueness of the solution to the linear discrete inverse problem. They have culminated in the generalized solution. The question of the stability of the generalized solution remains unanswered. This stability is precisely the most serious complication of ill-posed problems. In the next section, we will discuss regularization, which is the procedure to damp the instability. Before we do so, we must define the conditions under which the instability makes the generalized solution unfit for application, or, in other words, when error magnification becomes too large. These conditions are most easily found with the help of the SVD.

We want a solution that is stable to the variations in the input that are caused by measurement errors, discretization errors, roundoff errors, etcetera. Stability means that the norm of the solution does not change much with these variations. In the SVD, matrices U and V have orthonormal columns. Therefore, these matrices do not have much influence on the norm of the solution $\|\boldsymbol{x}\|$. However, matrix D^{-g} strongly affects the norm of the solution and the smallest singular values have the largest effect, by the weight of their large inverses sv_i^{-1} in D^{-g}. Of course, this applies both to the error-free component of the data and to the error component.

The magnifying effect of the smallest singular values causes no harm when it works on the error-free component only. This is the result of the fact that the features of the solution that are magnified, are only very weakly represented in the data. The latter, by the way, is the very essence of the instability of ill-posed problems.

The complications arise from the fact that there is no way to discern the error-free component in the data from the error component, which completely overshadows the weakest features. As a result, direct inversion will mistake some of the errors for the weak features. These are amplified in the reconstruction and error magnification is the result. In other words, the minimum misfit principle matches the solution too closely to the measurements, and to the measurement errors. The information deficit has created the condition under which the error-magnifying effect can occur, but it is the minimum misfit principle that actually magnifies the errors.

It is easy to show that a rough estimate of the relative error magnification REM, is given by

$$\text{REM} \approx \sqrt{\frac{1}{k}\sum_{j=1}^{k}\left(\frac{\max(sv_i)}{sv_j}\right)^2} \,. \tag{3.24}$$

A further estimate shows that REM $\lesssim$ CN, where CN is the condition number of a matrix. CN is defined as the ratio of the largest singular value of a matrix over the smallest:

$$\text{CN} = \frac{\max(sv_i)}{\min(sv_i)} \,, \tag{3.25}$$

and when some singular values are zero, we apply the old trick to evade the infinity of CN:

$$\text{CN} = \frac{\max(sv_i)}{\min(sv_i|\ sv_i > 0)} \,. \tag{3.26}$$

Now we have an estimate of the relative error magnification. We may say that the solution is unacceptable, if it has a relative error larger than 1, or 100%. The relative error in the solution equals the relative error in the data (RED) times the relative error magnification (REM, and REM $\lesssim$ CN). As a result we need regularization when the relative error in data exceeds the inverse of the condition number, or when RED $>$ CN^{-1}.

Generally, the condition number of a matrix increases very rapidly with its size. As a consequence, large inverse problems with many unknowns and many data points are generally far more unstable than those with few unknowns and few data points. In tomography, the condition number generally exceeds 10^6. Because the relative measurement error is generally larger than 10^{-6}, the generalized solution is unstable.

Remark that the SVD illustrates the close relationship between the non-uniqueness and the instability of solutions to ill-posed problems. In the SVD, non-uniqueness of the solution corresponds to a singular value being zero, while instability corresponds to singular values being small!

3.5 The regularized solution

The preceding section solved the non-uniqueness and the non-existence of the solution to the system of equations (3.17) by producing the so called generalized solution. In the end of the

section, it was shown that the generalized solution is unstable, thus establishing the need for regularization.

It has been said and repeated that there is a close relation between the non-uniqueness of the solution and its instability, and that both are caused by an information deficit in the experimental data. The non-uniqueness is solved by the minimum norm principle, and this principle, in its turn, closely resembles the major regularization techniques. These techniques damp the instability by requiring that the norm be small. In section 3.4, we have also seen that, although the instability is caused by the information deficit, it is effectuated by the minimum misfit principle. Therefore, it is no surprise that the same major regularization methods abandon the minimum misfit principle.

We will now present some of the possible regularization methods. Bertero et al (1988) give a similar review, although they put more emphasis on the mathematics. The last subsection discusses the choice of the all-important norm.

3.5.1 Weighting

The first step is to weight the data. This is not regularization in the strict sense. Still, weighting helps to reduce the magnification of errors in the process from measurement to reconstruction. It does so by reducing the weight of data points with a large error and enhancing the weight of high quality data points. The error in the solution is reduced, when every equation is weighted by the inverse of the standard deviation of the error in its corresponding data point. In other words, if the error in data point d_i has a variance σ_i^2, the left and right hand sides of equation i in the system (3.17) must be divided by σ_i. In matrix notation this boils down to left multiplication by $W^{-1/2}$:

$$A\boldsymbol{x} = \boldsymbol{d} \quad \longrightarrow \quad W^{-1/2}A\boldsymbol{x} = W^{-1/2}\boldsymbol{d} \tag{3.27}$$

where $W^{-1/2}$ is a diagonal matrix with elements σ_i^{-1}. The matrix W is defined as a diagonal matrix with elements $w_{i,i} = \sigma_i^2$. It follows that $W^{-1} = W^{-1/2}W^{-1/2}$.

This is not the whole story. When the measurements are not independent, W has elements off the diagonal that are non-zero $w_{i,j} = \mathrm{cov}(d_i, d_j)$. (If d_i and d_j are independent then $\mathrm{cov}(d_i, d_j) = 0$.) W is called the covariance matrix. W is a symmetric positive semidefinite matrix and when all variances are larger than zero, $\sigma_i > 0$, W is positive definite. In this case $W^{-1/2}$ exists. This non-diagonal matrix should be used in (3.27).

It is always good practice to weight the data. To simplify the notation, however, we have omitted W in the rest of this study. Yet, it is implicitly assumed, that the data are weighted. When the reader wants to make the weighting explicit, he should make the following substitutions everywhere: replace $\boldsymbol{d}$ by $W^{-1/2}\boldsymbol{d}$, replace A by $W^{-1/2}A$, replace A^t by $A^tW^{-1/2}$, etcetera.

3.5.2 Limitation of the number of basis functions

In section 3.4, we have seen that the condition number of the matrix A, and therefore the instability of the system (3.17), increases with the size of A. It is therefore a good idea to decrease the size of the inverse problem, which will increase the stability of the solution. We can accomplish this by decreasing the number of basis functions. When the number of basis functions is much smaller than the number of data points, the condition number may shrink to an acceptable size. This is indeed a procedure that is often used to stabilize the solution.

However, it is not regularization in the sense of the Tikhonov criterion, because there is no regularization parameter. (If the number of basis functions had an upper limit set by the regularization parameter, it could be a formal regularization procedure.)

The decrease of the number of basis functions, of course, increases the discretization error. This effect can be mitigated when the basis functions are well chosen and fit the solution well. Such a smart choice of basis functions requires a priori information of the solution.

3.5.3 Truncation of the SVD

In the discussion on the singular value decomposition SVD (section 3.4), we have seen that the contribution to the solution from the smallest singular values, increases the norm of the solution dramatically and therefore destabilizes the solution. We have also seen that the singular values that equal zero and thus frustrate the inversion, are just ignored in the generalized solution. The same attitude towards the smallest non-zero singular values, could enhance the stability of the solution. And indeed it does. This regularizing strategy is known under the name truncated SVD or TSVD.

In this approach, the elements $d^{-g}{}_i$ of the diagonal matrix D^{-g} become

$$d^{-g}{}_i = sv_i^{-1} \quad \text{if} \quad \frac{sv_i}{\max(sv_j)} > \alpha \ ,$$
$$d^{-g}{}_i = 0 \quad \text{if} \quad \frac{sv_i}{\max(sv_j)} < \alpha \ .$$

Here α is the regularization parameter and $\alpha > 0$. We see that the TSVD solution equals the generalized, or SVD, solution when $\alpha \to 0$. When the measurement errors vanish, the SVD solution equals the 'true' solution. Therefore, the TSVD solution is the 'true' solution when $\alpha \to 0$ and the measurement errors vanish. The Tikhonov criterion is thus satisfied.

The truncation procedure sets an artificial limit to the condition number CN: CN$< 1/\alpha$. At the end of section 3.4, we have seen that the condition number roughly equals the relative error magnification. A solution is not acceptable when its relative error is larger than 1, because it is then overgrown by error. Therefore, the product of the relative error in the data (RED) and the error magnification (given by CN) should be smaller than 1: RED$\times$CN <1. As the condition number is artificially limited to CN$< 1/\alpha$, a good choice for the regularization parameter is $\alpha =$RED. This works indeed in practical applications of the TSVD.

The side effect of the truncation is to reject the contributions to the solution by those columns of V that correspond to the smallest singular values. These columns represent features of the solution that are thus rejected. This rejection introduces a systematic error, which should be balanced by the decrease of the random error. The rejection also decreases the Euclidean norm of the solution. Therefore, the assumption that the length of the solution be small, constitutes the a priori information. This may not always be appropriate. Another, user supplied, quadratic norm could be used instead of the standard norm. This is the basis of the generalized SVD and the truncated generalized SVD (see section 3.5.7).

3.5.4 Tikhonov regularization and damped least squares

In the least squares approach, the solution is a vector that minimizes the misfit. We have seen that this approach can lead to unstable solutions. Tikhonov (1963) proposed to damp this instability by minimizing a weighted sum of misfit and norm, instead of just the misfit.

The minimum misfit principle is thus abandoned. In discrete inverse theory, the Tikhonov procedure amounts to finding the $\boldsymbol{x}$ that solves

$$\min_{\boldsymbol{x}\in\mathrm{R}^n} \|A\boldsymbol{x} - \boldsymbol{d}\| + \alpha\|B\boldsymbol{x}\| \,, \tag{3.28}$$

where α is the regularization parameter and $\alpha > 0$. The weighted sum of equation (3.28) is sometimes called the cost function. B is a positive definite matrix and therefore $\|B\boldsymbol{x}\|$ defines a norm, the B-norm. The larger α, the larger the influence of B on the solution. It is clear that the positive definite matrix B should incorporate the prior knowledge, and that a solution that is likely in the a priori sense should have a small B-norm. Usually, B is a discrete approximation of some derivative operator. By this choice, $\|B\boldsymbol{x}\|$ decreases with increasing smoothness of $\boldsymbol{x}$; this choice thus enhances the smoothness of the solution. It is easy to show that the solution to (3.28) is given by

$$\boldsymbol{x} = \left[A^tA + \alpha B^tB\right]^{-1} A^t\boldsymbol{d} \,, \tag{3.29}$$

which always exists because A^tA is positive semidefinite, B^tB is positive definite and $\alpha > 0$. It follows from (3.29) that this solution is a linear mapping from data to solution space, as long as the choice of α and B do not depend on $\boldsymbol{d}$. This procedure satisfies the Tikhonov criterion. The method is also known as damped least squares. The interested reader is kindly referred to Menke (1989), where its use in geophysics is extensively discussed. In the damped least squares approach, the value of α is unspecified. It is left to the user's experience to choose an appropriate value.

The indeterminacy of α can be removed by constrained optimization. The idea is that the user knows an upper limit to the norm of the solution or to the misfit, which he uses as the constraint in a constrained optimization problem. The value for α follows naturally from the constraint. It is clear that this approach does not give a linear mapping from data to solution space, because α will vary with $\boldsymbol{d}$.

Specifying an upper limit, F, to the B-norm of the solution, reduces the inverse problem to finding the solution $\boldsymbol{x}$ of the constrained problem

$$\min_{\boldsymbol{x}\in\mathcal{S}} \|A\boldsymbol{x} - \boldsymbol{d}\|, \quad \mathcal{S} = \{\boldsymbol{x} \in \mathrm{R}^n |\ \|B\boldsymbol{x}\| \leq F\} \,. \tag{3.30}$$

Here the constraint, $\|B\boldsymbol{x}\| \leq F$, comes from the prior information. The set of points in the solution space that satisfy the constraint, $\mathcal{S}$, is called the feasible set. The objective function (the misfit) is given by the experiment. Constrained optimization problems are solved by the method of the Lagrange multipliers, which we will use in chapter 5. The nice thing about this method is, that it uses the damped least squares equation (3.28). In its new function, the regularization parameter α in (3.28), is called the Lagrange multiplier. In the method, the Lagrange multiplier is set by the constraint, which eliminates the indeterminacy. The problem with this approach is, however, that it is generally very hard to estimate F. Therefore, the following strategy is more promising.

Specifying an upper limit to the misfit and not to the norm of the solution, leads to an approach where the roles are reversed. It amounts to solving

$$\min_{\boldsymbol{x}\in\mathcal{S}} \|B\boldsymbol{x}\|, \quad \mathcal{S} = \{\boldsymbol{x} \in \mathrm{R}^n |\ \|A\boldsymbol{x} - \boldsymbol{d}\| \leq E\} \,. \tag{3.31}$$

This problem also uses (3.28), though now α equals the inverse of the Lagrange multiplier, which must again be determined from the constraint. This approach was pioneered by Phillips (1962) for the numerical solution of Fredholm integral equations of the first kind. Mozorov followed (1968) and called the method the error principle. In the review article by Turchin et al (1971), it is called the discrepancy principle.

By this principle, E is set equal to the upper bound of the length of the error vector. Of course, this is an overestimate, which will lead to a regularization that is too strong. As a result, the user is forced to reduce the degree of damping and he is again left to his experience to determine α.

The most obvious thing to save the situation, is to accept the stochastic character of experimental data. We can estimate the length of the error vector, and argue that the misfit of the solution should equal this length. This means that we set E equal to the expected length of the error vector, instead of to an upper limit to its length. This is the approach of this thesis. With this estimated E we have

$$\min_{\boldsymbol{x}\in\mathcal{S}} \|B\boldsymbol{x}\|, \quad \mathcal{S} = \{\boldsymbol{x} \in \mathrm{R}^n | \ \|A\boldsymbol{x} - \boldsymbol{d}\| \ = E\} \ . \tag{3.32}$$

All points in the feasible set, $\mathcal{S}$, are consistent with the experiment, because they fit the data to the expected error. The solution of this constrained optimization problem has the following interpretation: of all points consistent with the experiment it is the one that agrees best with the a priori information.

The feasible set, is the set of all $\boldsymbol{x}$ that satisfy $\|A\boldsymbol{x} - \boldsymbol{d}\| = E$. As we have seen in the geometrical interpretation in section 3.4, this quadratic form corresponds to an ellipsoid in solution space, the feasible region. The larger the condition number of A, the more the ellipsoid is elongated. The size of the ellipsoid is set by the estimated data error E. It follows that a large CN and a large E make that the points in the feasible region are far apart in solution space. The role of the objective function (and therefore of the a priori information) is to choose between the points in the feasible region. Its importance grows when data error and CN increase.

In chapter 5 we will present an algorithm that solves the constrained optimization problem. It will be shown that the quadratic function and the feasible set are convex, which makes the optimization problem easier. It will also be shown that the solution to such a problem lies generally on the boundary of the feasible set. Therefore, solving (3.32) is equivalent to solving 3.31.

What is the expected length of the error vector? In other words, how do we determine E? The length of the error vector equals the sum of the squares of the errors in the data points. We assume that these individual errors have a normal (Gaussian) distribution, and that the system of equations is weighted. In that case, the weighted errors are independent stochastic variables with standard normal distribution. There are m equations and therefore m errors. The sum of squares of these variables is itself a stochastic variable, characterized by the χ^2 distribution with m degrees of freedom. The expected value of a stochastic variable with such a distribution equals $\sqrt{m}$. Therefore, we set $E = \sqrt{m}$.

3.5.5 Bayesian strategy or the maximum likelihood solution

In the discussion of the discrepancy principle, the stochastic behaviour of the data plays an important, though not a vital, role. In contrast, the Bayesian strategy to inverse problem solving is totally based on the concept of probability.

Bayes' formula (cf. Fisher 1974), relates the a priori, $P(\boldsymbol{x})$, and the a posteriori, $P(\boldsymbol{x}|\boldsymbol{d})$, probabilities:

$$P(\boldsymbol{x}|\boldsymbol{d}) = \frac{P(\boldsymbol{x})P(\boldsymbol{d}|\boldsymbol{x})}{P(\boldsymbol{d})} \ . \tag{3.33}$$

P is a probability distribution and $P(a|b)$ is the chance that a will occur, given the fact b, or with the prior knowledge of b. Applied to inverse problems, $P(\boldsymbol{x}|\boldsymbol{d})$ is the chance that the state $\boldsymbol{x}$ is true, given the data $\boldsymbol{d}$. $P(\boldsymbol{d}|\boldsymbol{x})$ is the probability that a given state $\boldsymbol{x}$ gives a certain experimental result $\boldsymbol{d}$. Therefore, $P(\boldsymbol{d}|\boldsymbol{x})$ describes the experiment, or the forward problem. $P(\boldsymbol{x})$ is the a priori probability density function. Although it may seem odd, $P(\boldsymbol{d})$ gives the prior probability of the data, yet its only role is to ensure proper normalization:

$$P(\boldsymbol{d}) = \int P(\boldsymbol{x})P(\boldsymbol{d}|\boldsymbol{x})d\boldsymbol{x} \ . \tag{3.34}$$

The Bayesian strategy aims at finding that solution $\boldsymbol{x}$, for which $P(\boldsymbol{x}|\boldsymbol{d})$ from (3.33) is maximum. It is called the maximum likelihood solution.

Before we can apply this strategy, we must know $P(\boldsymbol{d}|\boldsymbol{x})$ and $P(\boldsymbol{x})$. When the direct problem is described by the system of equations (3.17) and the error in d_i follows a normal distribution with mean zero and variance σ_i^2, then $P(\boldsymbol{d}|\boldsymbol{x})$ is given by

$$P(\boldsymbol{d}|\boldsymbol{x}) = \prod_{i=1}^{m} \frac{1}{\sqrt{2\pi}\sigma_i} \exp\{\frac{-1}{2\sigma_i}(d_i - \sum_{j=1}^{n} a_{i,j}x_j)^2\} \ . \tag{3.35}$$

It is easy to show that $P(\boldsymbol{d}|\boldsymbol{x})$ reaches is maximum when the (weighted) misfit is minimum. The weighted misfit is defined by

$$\text{weighted misfit } = \sum_i \frac{1}{\sigma_i}(d_i - \sum_j a_{i,j}x_j)^2 \ . \tag{3.36}$$

From (3.33) it follows that, if the prior probability distribution $P(\boldsymbol{x})$ is flat, the maximum of $P(\boldsymbol{x}|\boldsymbol{d})$ is attained when $P(\boldsymbol{d}|\boldsymbol{x})$ is maximum. Therefore, the minimum misfit, or least squares solution (the minimizer of 3.36), equals the maximum likelihood solution (the maximizer of 3.33), if $P(\boldsymbol{x})$ is flat. This shows that a flat a priori probability distribution takes us back to the least squares solution, the precise situation we tried to escape from. However, it is very difficult to specify the matemathical form of the prior distribution $P(\boldsymbol{x})$, when the a priori information is defined in general terms. The formulation of $P(\boldsymbol{x})$ becomes relatively easy, when we know one or several specific solutions with associated (a priori) probability distributions. If the associated distribution happens to be normal, the maximum likelihood solution is the same as the damped least squares solution (see Menke, 1989). In most cases though, the prior information is not so specific.

There exists a formal way, however, to define the distribution $P(\boldsymbol{x})$. With help from information theory, it is possible to assign an entropy to every probability distribution $P(\boldsymbol{x})$. The distribution with the highest entropy is the distribution that contains the least information possible, or that is the 'most noncommittal with regard to missing information' (Jaynes, 1968). Generally, the flatter the probability distribution, the higher its entropy.

3.5.6 Maximum entropy

The maximum entropy method is a kind of bastard offspring of the Bayesian strategy. Information theory proper assigns an entropy to a *probability distribution*, $\text{Ent}(P(\boldsymbol{x}))$. Later,

people have used the principle, and assigned an entropy Ent($\boldsymbol{x}$) to every *state* $\boldsymbol{x}$ in the probability distribution (Gull and Daniell, 1978). The entropy of a (macroscopic) state scales with the logarithm of the total number of its possible microscopic realizations. The larger this number, the higher the probability that the state corresponds to reality. In images, the number of realizations equals the total number of ways the image can be produced by a random process of 'filling' the pixels. This is the very reason for the fact that only images with non-negative pixel values have an associated entropy, and only such images will be generated by the maximum entropy method. The smoother the image, the larger its number of possible realizations, and the higher its entropy. The entropy expression is generally a trancedental function with a logarithm somewhere.

The larger the number of realizations, the more likely the state is. Therefore, the state with the highest entropy is considered the most likely in the absence of prior information. This leads to the formulation of the maximum entropy solution in inverse problems: Find the state $\boldsymbol{x}$ that solves the following constrained optimization problem:

$$\max_{\boldsymbol{x}\in\mathcal{S}} \text{Ent}(\boldsymbol{x}), \quad \mathcal{S} = \{\boldsymbol{x} \in \mathrm{R}^n | \ \|A\boldsymbol{x} - \boldsymbol{d}\| \leq E\} \ . \tag{3.37}$$

This formula is quite similar to (3.31). The solution has the following interpretation. Of all states that fit the experimental data to within the measurement error, it is the most noncommittal with regard to missing information. In practice, it imposes smoothness and it guarantees positivity.

3.5.7 The norm

As anticipated, we conclude the section with some remarks on the norm. In the discussion of this chapter we have seen that the norm plays a very important role. All solutions from discrete inverse theory, except maybe those based on Bayes' formula, boil down to optimization. In the formulation of the optimization problem, the norm features in either the objective function or in the constraint or in both. Therefore, we must choose a norm. What is the implication of our choice on the meaning of the solution?

The l-norm, $\|.\|_l$, where $l = 1, 2, 3, \ldots$, is defined by

$$\|\boldsymbol{x}\|_l = \left(\sum_i |x_i|^l \right)^{1/l} \ . \tag{3.38}$$

The 2-norm (or Euclidean norm) is the simplest norm with continuous derivatives. This is of considerable importance, because it greatly simplifies solving the optimization problem. The 2-norm is also the standard norm. Of more importance to our discussion though, is the fact that the Euclidean norm is narrowly related to the Gaussian distribution. [This is indicated by the relationship between equation (3.35), the Gaussian distribution, and equation (3.36), essentially the (weighted) Euclidian norm; in other words, the Euclidian norm appears in the exponent of the Gaussian distribution. In fact, all realizations of an experiment whose (weighted) error vectors ($A\boldsymbol{x} - \boldsymbol{d}$) have the same 2-norm (misfit) $\|A\boldsymbol{x} - \boldsymbol{d}\|_2$, are equally likely, provided that the error distribution is Gaussian.] Add to this close relationship between Gaussian distribution and Euclidian norm, the widespread assumption that measurement errors do indeed have a Gaussian distribution, and the question of the norm seems settled: use the Euclidean norm.

Yet, it is more of a convenient belief than it is a fact, that measurement errors have a Gaussian distribution. The choice of the Gaussian distribution is more often justified by a call to the central limit theorem, than by a statistical analysis of the errors themselves. Anyhow, our receivers produce errors that have a two sided exponential distribution, which is revealed by the close inspection presented in section 2.9. The essential difference between the Gaussian and the two sided exponential distributions is the tolerance to outliers. In the Gaussian distribution, an error larger than three times the standard deviation is very unlikely: a 0.26 % chance. The two sided exponential distribution is much less repudiating, with a chance of 1.44 %. The consequence is that the least squares solution depends more on the outliers than the 1-norm solution. This illustrates the sensitivity of the least squares method to real and noisy data.

An example. We often take the mean value of a set of measurements to approximate the 'true' value. And right we are, because the mean is easy to calculate. If the distribution of the measurement errors is Gaussian, there is a more fundamental justification: The mean value corresponds to the maximum likelihood estimate of the mean of the underlying (Gaussian) distribution. The maximum likelihood estimate is defined as the point $\boldsymbol{x}$ that maximizes $P(\boldsymbol{d}|\boldsymbol{x})$ in (3.35), for $\boldsymbol{d}$ fixed. (The function $P(\boldsymbol{d}|\boldsymbol{x})$ with $\boldsymbol{d}$ fixed is called the likelihood function). In this example we have $n = 1$, and therefore the summation over j is suspended. We assume equal measurement accuracies (σ_i is constant). It follows from (3.36) that the likelihood function is maximized for that x that solves

$$\min_x \sum_{i=1}^{m} (d_i - x)^2 \ . \tag{3.39}$$

Differentiation shows that the mean ($x = \frac{1}{m}\sum d_i$) is the maximum likelihood estimator.

When the set of measurements has a bit of a disorderly appearance, experimenters are inclined to use the median, which they call a more robust estimator. And so it is, because the median is precisely the maximum likelihood estimate, if the error distribution is two sided exponential. In this case, equation (3.39) becomes

$$\min_x \sum_{i=1}^{m} |d_i - x| \ . \tag{3.40}$$

The median solves this optimization problem. The disadvantage is that the median is more laborious to calculate than the mean, because the data have to be sorted.

In this example we see that the mean corresponds to the minimizer of the misfit with 2-norm, and the median to the minimizer of the misfit with 1-norm. It also shows the relation between the 1-norm and the two-sided exponential distribution on the one hand, and the relation between the 2-norm and the Gaussian distribution on the other.

Because the receivers' errors have a two sided exponential distribution, it is not really justified to use the Euclidean norm. The same line of reasoning that couples the Gaussian distribution to the Euclidean norm, leads from the two sided exponential distribution to the 1-norm. In fact, all realizations of an experiment whose (weighted) error vectors ($A\boldsymbol{x} - \boldsymbol{d}$) have the same 1-norm (1-misfit), $\|A\boldsymbol{x} - \boldsymbol{d}\|_1$, are equally likely, if the error distribution is a two sided exponential distribution.

Again, the question seems settled: we should use the 1-norm in the optimization procedures. However, this is a bit too costly from a computational point of view, because powerful

matrix methods, such as SVD, cannot be applied. We will have to make do with the 2-norm. Tests will have to show if its results are satisfying. (Which they are, as we will see in section 4.4.)

Now the choice for the Euclidean norm is made, we are almost there. Within the 2-norm there is still room for differentiation. In the discussion of the SVD we used the regular Euclidean norm, but in the damped least squares methods, the B-norm suddenly showed up. The B-norm is given by $\|B\boldsymbol{x}\|_2$, where B is a positive definite matrix. We have seen that the B-norm is supposed to introduce other prior information than length for the regularization.

There is a modification of the SVD that uses this B-norm, this is the generalized SVD (see section 5.3 of this thesis, or Golub and Van Loan, 1989). Of course, the generalized SVD can be truncated just as well. This is the generalized (or modified) truncated SVD or TMSVD, described by Hansen et al (1992).

3.6 Row action methods

The matrix approaches we have been discussing, have become pretty standard tools to solve systems of equations. In the old days, computer memories were too small to contain the whole of matrix A. To overcome this, and to profit from the sparseness of A, row action methods were developed. These iterative methods consider one equation of the system, and thus one *row* of the matrix, at the time. For really large systems of equations, as in the 3 dimensional tomographic imaging of the interior of the earth, advanced applications of row action methods are still in use (Spakman, 1993). Row action methods for image reconstruction are reviewed by Censor (1981 and 1983). We discuss two typical examples of these row action methods: ART and MART.

3.6.1 ART

The algebraic reconstruction technique, ART for short, was developed for tomography, or image *reconstruction*. Later it was shown to be identical to Kaczmarz's algorithm for solving systems of linear equations, where an equation corresponds to a line integral (or ray) in tomography. The technique starts with an initial approximation to the solution, or image vector. In every step the current estimate is corrected by taking into account a single ray, or equation. The difference $(d_i - (\boldsymbol{x}^k, \boldsymbol{a}_i))$ of the pseudo measurement on the current estimate, $(\boldsymbol{x}^k, \boldsymbol{a}_i)$ and the real measurement (d_i), is redistributed among the pixels, proportional to the intersection length of the ray with the pixel. Thus in every step, only those pixels that are intersected by the ray are corrected.

A formal description of ART is the following. The i^{th} row of A is denoted by $\boldsymbol{a}_i$, being a vector in R^n. Standard inner product is indicated by $(\boldsymbol{x}^k, \boldsymbol{a}_i)$ and, consequently, the norm, $\|.\|$, is Euclidean. Then,

$$\begin{aligned} \text{initial guess} &: \boldsymbol{x}^0 \in \mathrm{R}^n, \text{ arbitrary }, \\ \text{typical step} &: \boldsymbol{x}^{k+1} = \boldsymbol{x}^k + \lambda_k \frac{d_i - (\boldsymbol{x}^k, \boldsymbol{a}_i)}{\|\boldsymbol{a}_i\|^2} \boldsymbol{a}_i \ , \\ \text{where the rays are chosen cyclically} &: i = i_k = k \pmod m + 1 \ . \end{aligned}$$

The λ_k are the relaxation parameters: $0 < \lambda_k < 2$. From Kaczmarz's point of view, the algorithm has the following geometrical interpretation. An equation represents a hyperplane

in the solution space R^n. With $\lambda_k = 1$, every step corresponds to a projection on this hyperplane. When λ_k is smaller this projection is underdone, when larger, it is overdone.

The behaviour and convergence of ART are well understood. If the system of equations is consistent, it can be shown that ART converges to an exact solution. When it is both consistent and underdetermined ART converges to the minimum norm solution, if $\boldsymbol{x}^0 = \mathbf{o}$. When the system is inconsistent, the behaviour of ART is more interesting. In this case ART is cyclically convergent. This means that after many iterations, the estimate follows a fixed and closed trajectory through the solution space. Of course, the cycle period equals the number of equations. When $\lambda_k \to 0$ for $k \to \infty$, the length of this trajectory vanishes and ART converges. It can be shown that it converges to a least squares solution. If, in addition, $\boldsymbol{x}^0 = \mathbf{o}$, ART converges to the least squares-minimum norm solution. This least squares solution is not very satisfying, as we have seen. (For proofs of ART's convergence, see Censor et al 1983).

A variant of ART is the simultaneous iterative reconstruction technique, SIRT. This method sums the computed corrections and after a round through all equations (one step of iteration) , the total correction is applied. The solution of SIRT does not depend on the order of equations and it converges directly (i.e. not cyclically), though not very fast. Again, convergence is towards a least squares solution. Thus the behaviour of SIRT is very similar to that of ART.

Other variants (ART2, ART3, see Censor 1983) take the measurement error into account. The hyperplane is replaced by a hyperslab that has a width determined by the error. The algorithms try to find a point that lies in all hyperslabs. Such a point only exists when a large value for the slab thickness is chosen, which implies an overestimated error. The behaviour of these modified ART algorithms is somewhat better than ART's.

3.6.2 MART

The multiplicative algebraic reconstruction technique, or MART, is in many ways similar to ART. The difference is that where ART is additive, MART is multiplicative. With the same notation, MART is given by:

$$\begin{aligned} \text{initial guess} &: \boldsymbol{x}^0 \in R^n,\ x_j^0 > 0\ , \\ \text{typical step} &: x_j^{k+1} = x_j^k \left(\frac{d_i}{(\boldsymbol{x}^k, \boldsymbol{a}_i)} \right)^{\lambda_k a_{i,j}/\|\boldsymbol{a}_i\|} \qquad j = 1, ..., n\ , \\ \text{where again} &: i = i_k = k \pmod m + 1\ . \end{aligned}$$

The relaxation parameters lie in the interval: $0 < \lambda_k \leq 1$. MART has no geometrical interpretation and its convergence is unclear (Censor 1983). (In one of our tests, the MART solution actually diverged.)

When the system of equations is consistent, it can be shown that MART converges to an exact solution (for references, see Censor 1983). When it is both consistent and underdetermined MART converges to a maximum entropy solution if $\boldsymbol{x}^0 = e^{-1}\mathbf{1}$. When the system of equations is inconsistent, as is most likely the case, the behavior of MART is obscure. An advantage of MART in image reconstruction is the positivity of the result. All elements of the solution $\boldsymbol{x}$ are positive: $x_j > 0\ ,\ j = 1, ..., n$. MART shares this characteristic with the maximum entropy solutions.

3.6.3 Evaluation

In summary, we can conclude that, under favorable conditions, row action methods converge to a least squares solution. Because such a solution often fails in inverse problems, regularization will be needed. In practical applications, regularization is implemented by the following three tricks:

1. Make sure to start with a good initial approximation. This initial guess should be based on a priori information.
2. Stop the iteration long before the final solution is reached. The user must determine the optimum number of iterations, which depends on the problem at hand.
3. Choose a small relaxation parameter, $\lambda \approx 0.2$.

It is clear that these apposite measures do not meet the Tikhonov and Bertero criteria for regularization as formulated in section 3.2. In this thesis, we do not use row action methods. Instead, we will develop an algorithm that borrows much from the damped least squares method and the discrepancy principle.

Chapter 4

Tomography of the ionosphere

The use of tomography for ionospheric imaging gives rise to some specific problems. This chapter analyses these problems and reviews the existing inversion algorithms. Next, it presents a new and model independent algorithm, followed by the results of extensive testing.

4.1 Problems in tomography of the ionosphere

In this section we will discuss the difficulties that emerge, and some of the choices we must make, when differential Doppler data from an array of receivers are used for tomography of the ionosphere. Every subsection is dedicated to one such problem.

4.1.1 The unknown offset in total electron content

In chapter 2, it was shown that the differential Doppler technique does not measure the total electron content (TEC) unambiguously. Instead, it measures differential TEC. In section 2.1, we have made the distinction between differential, relative and absolute TEC.

A differential Doppler receiver registers the differential TEC, which is the change in TEC that occurs with a shift of the line of sight (by a change in satellite position). These differential data can be integrated to obtain a TEC profile, but there remains an unknown offset, or constant of integration. A TEC record with such an unknown offset is called relative TEC. Once the offset is determined and added to relative TEC, we speak of absolute TEC. It must be noted that the information in the relative TEC record is the same as in the differential TEC record. The difference is in the representation. The absolute TEC record, by contrast, is more complete, because it also contains the constant of integration.

Every lock-on to a satellite generates a new and unknown offset, because the phase counting starts again. As a result, there is at least one unknown bias associated with every receiver for every satellite pass. When during a pass, phase lock is lost and acquired again, an additional bias is the result, provided that the data gap is too long to allow interpolation (Leitinger 1994).

The traditional methods of tomography require line integrals, or absolute TEC data, as input. By consequence, it would seem that we have to determine the unknown offset before we can do tomography. Yet, it is possible to modify some reconstruction algorithms so that they can handle differential or relative TEC. We now discuss the different options: use absolute

TEC, adapt the algorithm so that it can handle differential TEC, or adapt the algorithm so that it can handle relative TEC.

Absolute TEC

When we want to use absolute TEC records for tomography, we should first try to determine the unknown offset. In most cases, there is no information on TEC other than from the differential Doppler data. Therefore, the offset must be extracted from the differential Doppler data themselves. There are methods to make such estimates, albeit crude, and they were briefly mentioned in section 2.5. When estimating the offset for further tomographic use, Leitinger's two station method (Leitinger et al, 1975) is the best, because it makes full use of the data from several receivers on the satellite's ground-path. The method is easily generalized to a multi station method (Kersley et al 1993, Leitinger 1994), so that all receivers in the tomography experiment can contribute to the offset determination.

However sophisticated these methods may be, they all share an implicit assumption. It is assumed that all free electrons are confined to an infinitesimally thin layer at known altitude. By contrast, the product of tomography is an image where the electrons are not at all confined to a layer of vanishing thickness! Therefore, the initial assumption is in conflict with the final result. That is an uneasy situation that is best avoided.

Adaptation of algorithm

In the other approach, the tomography algorithm is adapted so that it can handle the data without knowledge of the offset. So far, nobody has found a way to make this change in an algorithm from the class of transform methods. The series expansion methods easily allow such a modification, which illustrates the flexibility as anticipated in section 3.2.

The modification is made by a simple adaptation of the original system of equations. In the original system, every equation corresponds to an absolute TEC measurement. The adaptation must be such, that an individual equation in the new set corresponds to either a relative TEC data-point or a differential TEC data-point. This leads to the two different representations: the relative TEC representation and the differential TEC representation. Here follow the adaptation recipes:

- differential TEC

  To allow for the differential nature of the TEC data, we subtract one equation from the next in the original system of linear equations. Every equation in the resulting system then corresponds to the change in TEC over an integration interval, which is precisely the output of the differential Doppler receiver. The first equation becomes meaningless and therefore, the number of equations in the system is reduced by one. (The first equation corresponds to the initial setting of the receiver's phase counter at phase lock.)

- relative TEC

  To adapt the original system of equations so that it corresponds to a set of relative TEC data points, one should subtract a reference equation from all others. The choice of the reference equation is arbitrary, although the first equation in the system is a natural choice. Again, this reduces the number of equations by one. The resulting system of equations is mathematically equivalent to the one obtained above.

Discussion

In the first studies of tomography of the ionosphere, absolute TEC values were used and the offsets were determined from the TEC data themselves, via single- or multiple station methods. The inaccuracies and ambiguities associated with these methods, along with their interactive and time consuming nature, motivated researchers to adapt the system of equations to one of the forms where the offset need not be estimated. Of the two representations, the relative TEC method has been the most popular, probably because the data preprocessing programs integrate the raw data to yield relative TEC records. Among its advocates we name Fremouw et al (1994), Raymund et al (1994b) and Markkanen et al (1995). Right from the start, however, Kunitsyn has used the differential TEC approach, which he calls phase difference tomography (Kunitsyn et al, 1995).

Which of the three methods is best? The addition of an estimated offset to generate absolute TEC data, has the following disadvantages when used for tomography. First, there is the contradiction between the initial assumption of the thin layer and the final result, where the ionosphere is extended in height. Second, all data-points are contaminated by the (substantial) error in the estimate. These data form the input to an ill-posed inverse problem, which has the main characteristic that it is very sensitive to errors in the data. Third, the method cannot determine the additional offsets that are required when there are data gaps that cannot be closed by interpolation. In the other methods, these problems do not exist. For these reasons, we prefer a method that does not need absolute TEC data.

Of the two methods that remain, adaptation of the system of equations to the differential TEC representation seems a better choice than adaptation to the relative TEC representation. That is a consequence of the fact that the receiver generates differential TEC data, whereas relative TEC data are obtained only after integration of the differential data. This integration makes the errors accumulate and makes them mutually dependent. As a result, the data covariance matrix becomes non-diagonal. In the differential TEC representation, by contrast, the errors are independent and the covariance matrix is diagonal.

It is by the weighting (section 3.5.1), provided that it is done properly, that both methods reduce to the very same system of equations. This is the result of the fact that the differential TEC representation and the relative TEC representation are equivalent.

The difference between the methods is that the weighting is much more cumbersome when the relative TEC representation is used, because the weight-matrix is non-diagonal. For this very reason, we choose to adopt the differential representation.

In the literature, however, there is no agreement on the method of choice. Kunitsyn et al (1995) have argued that the differential method should lead to reconstructions that reveal weaker structures than the other methods. This conclusion is contested by Markkanen et al (1995). They use a method based on relative TEC data. They compare their results with reconstructions made with an algorithm that uses differential TEC data, but that is otherwise the same. They see no essential differences. The fact that both authors see differences anyway, is probably due to the fact that they do not do the weighting properly; although it is not clear from their papers if they use weighting at all. (The reader may oppose that simulations without measurement errors, where weighting is unnecessary, do lead to different results when using either the relative or the differential TEC representation. The results would be the same, however, if they were exact solutions. The fact that the problem is ill-posed in combination with the slightest roundoff errors, makes that these 'exact' solutions are not realistic.)

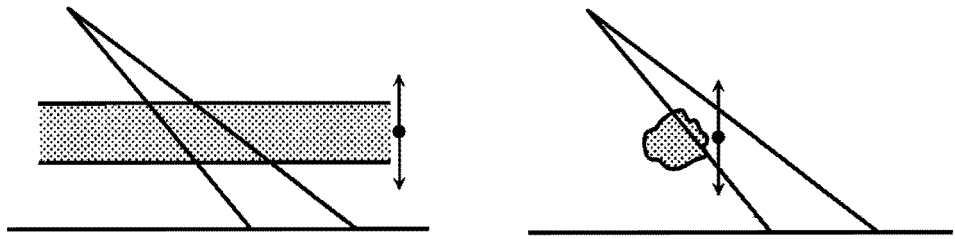

Figure 4.1: Over a flat earth, TEC records (electron density integrated along the diagonal lines) do not change with a height shift of a purely stratified ionospheric layer (left half). By contrast, the height shift of an isolated bulge will not go unnoticed (right half).

4.1.2 Missing horizontals and ill-posedness

In section 3.3, we have seen that the inverse problem of tomography can be solved if all line integrals are known, which is never the case in a real experiment. It is very well possible to make an approximate reconstruction if the data are well sampled, as we also have said. The problem with TEC measurements is that they are not at all well sampled. This bad sampling is the result of the poor geometry.

First, there is the problem that the ionosphere envelops the whole earth, and receivers should be placed around the globe. This is quite unfeasible. Yet, there is no objection to consider an isolated part of the ionosphere.

The second and really troublesome consequence of the geometry, is due to the fact that we only have TEC measurements along lines between orbiting satellites and ground based receivers, with the ionosphere in between. There are no measurements along horizontal lines, say from a satellite at 500 km height to a receiver at the same height. A set of such parallel registrations would give the vertical profile of the ionosphere. Therefore, it is precisely these missing horizontals that would contain the information on the vertical structure of the ionosphere. That information is now missing in the experimental data and can therefore not be expected to be rendered truthfully in the reconstruction.

The following argument illustrates the problem. Imagine a flat earth and a purely horizontally stratified ionosphere that is confined to a layer centered at some altitude, the ionospheric height (figure 4.1, left half). Let a satellite move at a fixed height above this layer, and let a receiver on earth measure TEC. Suppose that the ionospheric layer is shifted in height, but remains the same otherwise. It is clear that this has no effect whatsoever on the measured line integral, or TEC, because the length of the intersection of a ray with the layer is not affected by this shift. It follows that there is no information on the layer's height in the data. By contrast, horizontal TEC data would register the height shift.

Notice that this problem is less serious when we consider an isolated feature instead of a layer, because different lines of sight would cross such an isolated feature when it moves up or down (figure 4.1, right half). It follows that the problem of the missing horizontal integrations is aggravated by the fact that the ionosphere is basically a stratified medium! The problem of the missing horizontals is alleviated somewhat by the curvature of the earth. Through the curvature, a shift of ionospheric height gives a slight difference in the TEC record

of a stratified ionosphere. We will give examples of this phenomenon in the section with test results (section 4.4).

As a result of the missing information, the inverse problem is ill-posed: a change in the vertical structure is only barely reflected in the measurements and leaves a slight fingerprint, or slight evidence, in the data. The reconstruction algorithm would have to amplify this slight evidence in order to reconstruct the vertical structure. Unfortunately, the slight evidence is easily overwhelmed by measurement errors. These errors are amplified equally strong by the reconstruction algorithm, hence the extreme sensitivity to small variation in the input. It follows that regularization is required to damp the instability. In section 3.2, we have discussed several methods of regularization. In this chapter, we will apply them to tomography of the ionosphere.

The problem of the missing horizontals is nicely illustrated by the Fourier slice theorem, as was pointed out by Yeh and Raymund (1991). Let us return to figure 3.1, where this theorem is illustrated, and let us assume for convenience that the earth is flat. In that case, the missing horizontals are those arrows that are approximately parallel to the x-axis in the left half of the figure. It follows that only those projections where the angle ϕ is small, are available. Consequently, the Fourier space is not sampled completely (see the right part of the figure). Actually, only a region in the shape of a bow-tie is sampled. (This bow-tie is aligned along the horizontal axis and centered on the origin.) The vertical spatial frequency components remain unknown and this corresponds to unresolved vertical structure in the reconstruction.

A final remark. The whole problem of the missing horizontals would obviously disappear, if there would exist a measurement geometry where the horizontals are not missing! Such a geometry, where additional receivers are carried by satellites in low orbit, is discussed at the end of section (4.1.5.

4.1.3 The finite pass duration

A NNSS satellite moves in about a quarter of an hour from horizon to horizon. Due to the position of the pixel grid, the TEC data from lines of sight with elevations under roughly $10° - 15°$ cannot be used. We will illustrate this in section 4.4. (Moreover, these low elevation measurements are relatively sensitive to unwanted ray-bending (section 2.4), but that aside.) This means that the effective duration of TEC registration is about 10 minutes. If the ionosphere changes during this registration interval, the data set will be inconsistent. Its effect is comparable to that of measurement errors. Therefore we require that the ionosphere be stationary during the 10 minutes of effective TEC measurement. Two major violations of this restriction are possible. First, a satellite pass occurs during or shortly after passage of the solar terminator at sunrise or sunset. Second, ionospheric disturbances with a period under 20 minutes coincide with a pass registration.

4.1.4 The surface of reconstruction

Due to the earth's rotation and to practical problems, it is impossible to confine the satellite and the receivers to a fixed plane. Therefore, the lines of sight do not intersect and they do not form a surface, they do only approximately so. Moreover, this approximate surface is not flat, but it is curved. Consequently, tomography of the ionosphere has no plane of reconstruction, but only an approximate surface of reconstruction that is more or less a plane.

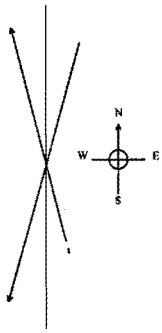

Figure 4.2: Orientation of ground-tracks (diagonal arrows) of NNSS satellites with respect to meridian.

This problem is a consequence of the geometry of the satellite orbit and the location of the receivers. As a result of the rotation of the earth, it is impossible to locate the receivers in such places as to keep all lines of sight in a plane. The orbit of the satellite defines a plane, this is a consequence of Kepler's first law. This plane should be the plane of the ionospheric reconstruction. During a satellite pass, the earth and the ionosphere rotate, and the ionosphere moves through the plane of the orbit. This implies that there is no plane of reconstruction. The best we can do, is to locate the receivers on the satellite's ground-path, which is a curve. As the earth rotates, the ground-path of the next satellite pass is shifted to a parallel ground-path and the receivers should have to be shifted as well. That is not a very practical idea. The second best we can do is to place the receivers on a certain ground-path. If this ground-path coincides with an actual ground-path of a satellite pass, the satellite moves through the zenith of the receivers. As a result, the surface of reconstruction is perpendicular to the surface of the earth. The next time the satellite passes, it is seen at a maximum elevation of say 35^o, and the surface of reconstruction is inclined 35^o with respect to the surface of the earth. This is a curved surface and the lines of sight are only approximately in this surface.

As a NNSS satellite moves in a polar orbit, its ground-path is approximately a meridian. The rotation period is about 110 minutes and in this period the earth rotates 27.5^o. During the 10 minutes of effective TEC registration, the sub-satellite point moves 33^o north or south by its own and 2.5^o west, due to the earth's rotation. When the satellite rises in the south, the ground-track is slightly tilted (north-)westwards with respect to the meridian. Half a day later, the satellite rises in the north, and the ground-track is tilted south-westwards. Consequently, the ground-tracks of north- and southbound satellites have different orientations (see figure 4.2). Because we want frequent registrations, we need data from both north- and southbound satellites. Therefore, we should ignore the westward deviations and put the receivers on the meridian.

Resuming: the surface of reconstruction is bent. The intersection of this surface of reconstruction with the surface of the earth is roughly a meridian. The surface of reconstruction is inclined with respect to the surface of the earth by an angle that roughly equals the maximum elevation angle of the satellite. Last but not least, the lines of sight lie only approximately in

this surface.

This poses a difficulty. We want to reconstruct the electron density in a plane from integrals along lines in the plane. But the lines of sight are not in the plane! This clearly requires a looser definition of the surface of reconstruction. In the new definition, the surface is extended in longitude and it must be assumed that the ionosphere is constant over this extent. An 'element' of the new surface of reconstruction has a well-defined latitude and a well-defined altitude, but only an approximate or mean longitude. The mean longitude is defined by the mean longitude of the points where the lines of sight cross the 'element'. The elements' longitudinal thickness is set by the spread in longitude. There are as much of these crossing points as there are receivers. The better the receivers are located on the satellite's ground-path, the less the spread in longitude and the smaller the longitudinal extent. This has the advantage that the assumption that the ionosphere be constant over the longitudinal extent, is less restricting.

The new definition of the surface of reconstruction requires an extension of the pixel concept. Normally, a pixel is an element of a plane. A regular ionospheric pixel is bounded above and below by segments of arc of fixed altitude, and on the sides by lines of fixed latitude. It is not extended in longitude and all pixels are supposed to be at the same longitude. As the lines of sight are not in the plane in which the pixels are defined, the intersection of a line of sight with such a flat pixel has zero length. Therefore, the new pixel is extended in longitude. In altitude, the new pixel is bounded by spherical surfaces, above and below. In latitude, it is bounded by conic surfaces of fixed latitude.

It is not difficult to compute the length of the intersection of a line of sight with such a pixel; the result of this computation is an element of the geometry matrix A (section 3.2). The centre of such an intersection is at a certain longitude. The mean longitude of all intersections with a pixel defines the longitude of the pixel and the spread in longitude defines the longitudinal extent. In any real measurement geometry, every pixel is at a different longitude, which illustrates the fact that the reconstruction is in a bent surface. This geometry has some strange consequences. For example, a line of sight can enter a pixel, leave the pixel at the side, intersect another pixel, re-enter the first pixel through the same side it has left, although at another longitude, and finally leave again!

Most researchers of ionospheric tomography calculate the geometry matrix A by first assuming a flat geometry, i.e. receivers and satellite orbit in the same meridional plane, and then multiply the intersection lengths with a geometrical correction factor. It is clear from the example above that this is only an approximation. It works well for near zenith satellite passes, but it fails for passes of low elevation.

4.1.5 Tomography with TEC from other sources

TEC data from observations of NNSS satellites are very suitable for tomography of the ionosphere. One reason is that these satellites transmit in the right frequency range, roughly between 100 and 1000 MHz. These frequencies are neither so low that reflection and ray bending occur, nor so high that propagation is insensitive to ionospheric electron density (see chapter 2). Equally important, though, is that their circular orbit is in the right altitude range, roughly 1000 - 5000 km. At 1100 km, the NNSS orbit is neither too low nor too high. The orbit could not be much lower, as the differential Doppler technique misses all of the ionosphere above the satellite orbit. A high orbit, on the other hand, gives a long revolution period and a long pass duration. The NNSS satellites have an effective pass duration of 10

minutes, which is short enough to validate the assumption of a frozen ionosphere. The pass of a satellite at 5000 km altitude takes twice as long.

These considerations lead to the question if there are other sources of TEC data that could be used for tomography. Whether the TEC measurements are based on Faraday rotation, group delay or phase delay, they all require a beacon on one side of the ionosphere and receivers on the other. This beacon can be a satellite or a radio star.

First there is the NNSS system. Its Russian counterpart, CICADA (section 2.2), can and indeed has been used for tomography by Andreeva and comrades (1990).

At greater altitudes, we find another set of beacons, the GPS and GLONASS satellites (also in section 2.2). These satellites are in an orbit at 20,000 km altitude and have a period of 12 hours. By consequence, a satellite pass lasts roughly 5 hours, over which the ionosphere changes a lot. It is possible to take this variation into account. This requires reconstruction of electron density as a function of three variables: two spatial variables for the surface of reconstruction and one for the time. The number of unknowns in the reconstruction thus increased, it will probably be necessary to increase the amount of observational data by inclusion of data from other (GPS) satellites. Unfortunately, these do not have lines of sight in the same surface. Therefore, another (spatial) dimension will come in. This leads to 4D tomography of the ionosphere. Whether this approach could possibly lead to useful results remains an open question. Anyhow, a twofold increase in the number of dimensions squares the number of unknowns. This will increase the size of the matrices by the power four, and the computing time in most matrix based algorithms by the power six. Quite unfeasible at the moment.

At even greater altitudes, the geostationary satellites provide another set of beacons. Because these satellites do not pass at all, they provide a very limited set of line integrals. The only possibility to achieve a sufficient number of lines of sight is to have many different geostationary satellites and an array of receivers on the ground. There are plenty of geostationary satellites, but unfortunately there are not so many beacon satellites among them. Moreover, they all have different transmitter and signal characteristics, which means that every ground station should be equipped with many receivers. Not very practical indeed.

At quasi infinite distances we find the next type of beacons: radio stars. In fact, these objects are not really stars. The important thing is that they are point sources. Their use for tomography of the ionosphere has been suggested by Spoelstra (1991) and Kunitsyn et al (1992). An array of radio telescopes at a parallel of latitude observing a radio star above the equator (declination $\delta = 0°$), gives lines of sight in a surface. The problem is that such a source moves in 12 hours from horizon to horizon, over which the ionosphere is not stationary. This is the same difficulty as encountered with the GPS satellites. Again, the same solutions can be considered, with the restriction that GPS satellites are preferable to radio stars, for two reasons. First, the extraction of TEC data from radio astronomical observations is more difficult (a radio star transmits noise, which is incoherent over all but the shortest time intervals). Second, radio telescopes are much more expensive than GPS receivers.

The conclusion seems justified that, at the moment, tomography of the ionosphere is only feasible with NNSS or CICADA satellites.

The problem of missing horizontals (section 4.1.2) could of course be solved, if there were a source of (near) horizontal TEC data. Such a source becomes available when satellites in low earth orbit (LEOs) are equipped with differential Doppler or GPS receivers. The lines of sight between a LEO and a GPS satellite provide the user with a vertical ionospheric profile

Localized basis functions	Non-localized basis functions
Do not fit a real ionosphere well: many basis functions required	Fit much better, if well chosen: fewer basis functions necessary
Easy to use	More complicated in use
A is a sparse matrix	A is a dense matrix
Relatively easy to include positivity of solution as prior information	Very difficult to include positivity of solution as prior information

Table 4.1: Comparison of the two types of basis functions for tomography.

every time the LEO satellite appears or disappears behind the horizon of the GPS satellite. When this horizontal scan is more or less in the same plane as the (vertical) TEC scans, and when the scans are approximately simultaneous, tomography of the ionosphere could become a really trustworthy diagnostic tool.

4.1.6 The choice of basis functions

If we use discrete inverse theory for the tomographic inversion, we must first choose the basis functions. There are basically two categories. First, there is the group of localized basis functions, such as the pixel-based functions. Such a function is unity inside a pixel and zero outside. Because the natural ionosphere is not built in a pixel grid, these basis functions do not fit well and many are required to get a reasonable discretization. Non-localized basis functions form the second group. In this category we find the Fourier basis functions (sines and cosines basically) and the empirical orthonormal basis functions, which are constructed by Gramm Schmidt orthogonalization of a set of model ionospheres (Fremouw et al 1992). If well chosen, these non-localized basis functions fit the ionosphere much better and relatively few suffice. In table 4.1, the options are compared.

It is mainly the last reason in the table that justifies our choice to use localized basis functions. The prior knowledge that the reconstructed electron density is everywhere positive, is incorporated by additional constraints on the solution, as we will see in section 4.3. This method meets the Tikhonov criterion (section 3.2), while the opportunist measure of putting (intermediate) negative results to zero, does not.

Kunitsyn et al (1995) have refined the use of localized basis functions to a high degree. They make two modifications to the ordinary pixel concept. First, they use triangular, rather than square pixels. They argue that this modification is necessary, because the pseudo measurements of differential TEC on an ionosphere represented by square pixels are a discontinuous function of time. It is not clear why the discontinuity should be a problem, but there is no harm in triangular pixels, either. The second modification is the use of piecewise planar pixels instead of piecewise constant pixels. This means that the electron density is allowed to

vary linearly with position throughout the pixel, rather than being set constant.

4.2 Review of ionospheric reconstruction techniques

Every research group has its own method of reconstruction. All methods have their merits and disadvantages and all methods have their own way to incorporate a priori information. The best way to judge a method is to apply it to several simulated data sets and compare the results with the phantom ionospheres that were used to generate the simulated data. For this, one needs a varied set of realistic model ionospheres, or phantoms. The simulated measurements must approach reality as closely as possible. It is especially important to make a realistic simulation of the measurement errors, because error magnification is a delicate point in most inversion methods.

It is even better to offer the same simulated data sets to different reconstruction techniques and compare the results, as Raymund did (1995). He concludes that there is no overall best algorithm and that the choice of the method should depend on the situation and the user's needs.

Before I give my personal view of the various reconstruction techniques, I mention Raymund's (1994) review that discusses existing algorithms. I also spend some words on the orthogonal decomposition 'framework' (ODA) presented by Sutton and Na (1994). The framework is supposed to encompass all reconstruction techniques. Yet, the ODA principle merely states that all algorithms are based on a linear transform from a (finite) set of basis functions in the measurement domain to a (finite) set of basis functions in the solution domain. Therefore ODA does not cover nonlinear algorithms, such as those based on constrained optimization. Neither does it cover the methods from continuous inverse theory, because they (implicitly) employ an infinite set of basis functions. As a result, ODA is merely an illustration of the linearity of the direct problem in discrete inverse theory.

Most methods encountered in ionospheric tomography, are based on discrete inverse theory. That is no surprise, given the results of section 3.2 where discrete and continuous inverse theory are compared.

Still, some researchers have used transform methods from continuous inverse theory, mainly to investigate the theoretical limits of ionospheric tomography. Continuous inverse theory has been used by Yeh and Raymund (1991) to illustrate the effect of the missing horizontals, as mentioned in section 4.1.2. Reconstruction in the Fourier domain has also been investigated by Rothleitner et al (1994) and by Na et al (1995). Yet, these transform methods have never been applied in real experiments.

Before discrete inverse theory can be applied, the unknown offset problem must be solved by one of the methods from 4.1.1 and the basis functions must be chosen, as discussed in 4.1.6. When that has been done, one of the methods from chapter 3 can be used to solve the system of equations.

The oldest ionospheric reconstruction technique used the ART algorithm (Austen 1986). Today, ART, MART and derivatives are still the most widely used algorithms (Kunitsyn et al 1995, Mitchell et al 1995, Cook and Close 1995, Pryse et al 1995, to name a few). These row action methods have some very serious drawbacks, as discussed in section 3.6, but they are easy to apply, and that partly explains their popularity. Regularization requires that the solutions produced by these iterative methods do not evolve too much from the initial guess. We have seen in section 3.6 that this is accomplished by choosing a small relaxation parameter

($\lambda \approx 0.2$) and by doing just a few steps of the iteration, varying from 3 (Mitchell et al 1995) to 10-20 (Andreeva et al 1990). It is clear that the initial guess is very important, and that most of it is preserved in the final result. In fact, the initial guess (or background ionosphere) determines the large structure and the iteration brings the finer structure into the solution. The success of these methods is therefore determined by the quality of the background model ionosphere. The background ionosphere is usually constructed from ionospheric models (such as the international reference ionosphere, IRI-90). Very often, these model ionospheres are chosen so as to match the TEC and/or ionosonde data, in some way or another. In this way, the row action methods can come up with acceptable reconstructions.

It is clear that these methods depend heavily on input from models and that they are quite untransparant. They do not meet the Bertero criterion for regularization. The all-matrix methods from section 3.5 are a step forward. Here follows a discussion of their applications.

- Raymund et al (1994b) use the singular value decomposition to compute the affine linear subspace whose elements solve the system of equations (3.17) in the least squares sense (the instability is damped by treating the smallest singular values as zero). Because the measurements are incomplete, there are infinitely many points in this subspace and a priori information must decide between them. In the algorithm, the authors do not use the minimum norm principle as prior information, but they choose the point in the affine subspace that is closest to a linear subspace spanned by a set of model ionospheres. Therefore, model ionospheres solve the indeterminacy in the set of equations.

- The algorithm presented by Kunitake et al (1995) uses the modified truncated singular value decomposition (MTSVD). This algorithm uses the modified (or generalized) SVD, which was briefly discussed in section 3.5.7. In this method, the point that has minimum B-norm is supposed to be the most likely in the a priori sense. Unfortunately, Kunitake is not very specific about the prior knowledge that he puts in matrix B.

- Fougere et al (1995) use a maximum entropy algorithm. As we have seen in section 3.5.6, this solution is the most non-committal with respect to missing information. In other words, it adds to the solution as little a priori information as possible. Unfortunately, this is too little to accommodate for the lack of information on the vertical structure, as Fougere and co-authors realize. Their rescue scheme is not very clear.

- Fremouw et al (1992 and 1994) use the weighted damped least squares solution which they obtained from Menke (1989). In section 3.5.4, this method was shown to be equivalent to standard Tikhonov regularization, where the minimum norm principle constitutes the prior information. In their algorithm, the minimum norm principle is good enough because of the clever use of basis functions. They use non-localized basis functions: sines and cosines in the latitudinal direction and empirical orthogonal functions (EOFs) in the vertical direction. The EOFs are based on model ionospheres.

- Markkanen et al (1995), claim that they follow the Bayesian approach in their algorithm. In reality, they use damped least squares, or Tikhonov regularization, as they themselves admit. They do not use the minimum norm principle as prior information, instead they minimize the norm of the difference of their solution with a Chapman ionosphere. This leaves two free parameters that must somehow be determined: scale height and height of maximum electron density.

There is a debate on how to incorporate ionosonde information in the reconstruction algorithms. Basically there are two approaches. The first approach adds the ionosonde measurements, after proper weighting, to the system of equations (cf. Raymund et al 1994). The second approach treats the ionosonde data as a priori information. For example, Heaton et al (1995) use the ionosonde information to determine the background ionosphere that forms their initial guess for the MART iteration. The model independent algorithm that we present in the next section, has an option to incorporate ionosonde information as a priori information.

4.3 A model independent algorithm

In this section we present a new ionospheric reconstruction algorithm. It is self-contained and to a high degree independent of ionospheric models. Instead, regularization is achieved by using much more general information. The algorithm does not require any interactive control from the user, therefore it can run in a batch. The algorithm is based on constrained optimization.

In most ionospheric reconstruction algorithms, the prior information on the vertical structure comes from model ionospheres. These models are by no means perfect. When the results of ionospheric tomography are used for radio propagation predictions or other practical applications, the use of models is perfectly sound. If, on the other hand, the results will be used for a better understanding of ionospheric behaviour or for the construction of better ionospheric models, it might not be so smart to start with existing models in the first place. That is why we have developed a model independent algorithm.

First the preliminaries. In this algorithm we use differential TEC as input, for reasons given in section 4.1.1. For the reasons presented in sections 3.2 and 4.1.1, we use discrete inverse theory. The arguments from section 4.1.6 give us reason to use localized basis functions, and we choose the pixels described in section 4.1.4. This reduces the inverse problem to the system of (weighted) linear algebraic equations (3.17):

$$\boldsymbol{A}\boldsymbol{x} = \boldsymbol{d} \tag{4.1}$$

The minimum misfit principle finds an approximate solution to this system by minimizing the misfit: $\|\boldsymbol{A}\boldsymbol{x} - \boldsymbol{d}\|$. Here the Euclidean norm is understood, which implies that the minimum misfit principle becomes the least squares principle. We have seen that the minimum misfit principle transfers the lack of information in the measurements into instability of the solution. We abandon the minimum misfit principle by requiring that the solution $\boldsymbol{x}$ satisfies the discrepancy principle from section 3.5.4:

$$\|\boldsymbol{A}\boldsymbol{x} - \boldsymbol{d}\| = E \ , \tag{4.2}$$

where E is an estimate of the length of the error vector (see section 3.5.4). All points that satisfy this equation are consistent with the experiment, because they fit the experimental data to the measurement error. There are, however, infinitely many points that solve equation (4.2). The larger the experimental error, E, and the larger the experimental information deficit (large condition number CN), the more these solutions differ. We must use a priori information to decide between these points, i.e. to fill the information gap. We have the following pieces of information:

- The electron density cannot be negative:

$$\boldsymbol{x} \geq \mathbf{o} \; . \tag{4.3}$$

  Here $\mathbf{o}$ is the nillvector, and the $\geq$ sign is understood for all elements in the vector $\boldsymbol{x}$.

- The ionosphere is basically smooth and stratified. In addition, the electron density is low at low and high altitudes. We cast these three pieces of information into a quadratic function $O(\boldsymbol{x})$, that is large when $\boldsymbol{x}$ is at odds with this information. This results in the following strategy:

$$\text{minimize} \;\; O(\boldsymbol{x}) \tag{4.4}$$

  A purist might argue that these three pieces of information are derived from an ionospheric model. They are formulated so broadly, however, that this argument has no more than formal value. Moreover, they are based on sound physical ideas. Stratification is imposed by gravity and smoothness by diffusion. At high altitudes electron density is low because particle density is low and at low altitudes there is no ionizing radiation to create free electrons.

The information from the experiment and the a priori information reduce the inverse problem to a constrained optimization problem:

$$\min_{\boldsymbol{x} \in \mathcal{S}} O(\boldsymbol{x}), \;\; \mathcal{S} = \{\boldsymbol{x} \in \mathrm{R}^n \mid \|A\boldsymbol{x} - \boldsymbol{d}\| = E \wedge \boldsymbol{x} \geq \mathbf{o}\} \tag{4.5}$$

The number of constraints equals the number of pixels (constraints: $\boldsymbol{x} \geq \mathbf{o}$) plus one ($E = \|A\boldsymbol{x} - \boldsymbol{d}\|$). The solution has the following interpretation: of all solutions consistent with the experiment and everywhere positive, it is the one that is most likely in the a priori sense. In chapter 5, we will present an algorithm that solves the constrained optimization problem in case $O(\boldsymbol{x})$ is a quadratic function. Apart from some pathological cases, (4.5) will be shown to have a unique solution.

It is very easy to implement a priori information from ionosonde in this algorithm, simply by adding extra constraints. For example, when we know that the electron density in pixel number 9 should be between 15 and 20×10^4 cm^{-3}, we add the constraints: $x_9 \geq 15 \times 10^4$ cm^{-3} and $x_9 \leq 20 \times 10^4$ cm^{-3}. When we know the density exactly, we add one constraint: e.g. $x_9 = 17 \times 10^4$ cm^{-3}.

What should the function $O(\boldsymbol{x})$ look like? It is convenient to take a quadratic function, because that permits the use of a fast and efficient optimization algorithm. Although the algorithm can handle more general quadratic expressions, it here suffices to define:

$$O(\boldsymbol{x}) = \|B_1\boldsymbol{x}\|^2 + r^2\|B_2\boldsymbol{x}\|^2 + \|B_3\boldsymbol{x}\|^2 \; . \tag{4.6}$$

Again, the Euclidean norm is understood. We discern three contributions to $O(\boldsymbol{x})$. The first, $\|B_1\boldsymbol{x}\|$, is a measure of horizontal flatness: it is large when the densities in two neighbouring pixels differ much. The second, $\|B_2\boldsymbol{x}\|$, is a measure of vertical smoothness. The scaling constant r, $0 < r < 1$, reduces the weight of vertical smoothness with respect to horizontal flatness. This favours a stratified solution, where the ionosphere is more homogeneous in the horizontal than in the vertical direction. The third, $\|B_3\boldsymbol{x}\|$, is a measure of electron density at the upper and lower side of the ionosphere.

Matrix B_3 is a diagonal matrix and most of its diagonal elements are zero. Only those elements on the diagonal that work on pixels at the upper and lower side of the ionosphere, are unity. Matrix B_1 is a first derivative matrix and B_2 is a second or third derivative matrix. The first derivative matrix is given by the $(n-1) \times n$ matrix D_n^1:

$$D_n^1 = \begin{pmatrix} -1 & 1 & & & \\ & -1 & 1 & & \\ & & \cdot & \cdot & \\ & & & -1 & 1 \end{pmatrix} . \tag{4.7}$$

The second and third derivative matrices are given by

$$\begin{aligned} D_n^2 &= D_{n-1}^1 D_n^1 \\ D_n^3 &= D_{n-2}^1 D_n^2 . \end{aligned}$$

These matrices must be adapted so as to work on horizontal neighbours only (in B_1) or on vertical neighbours only (in B_2). Tests similar to those of section 4.4 have shown that the algorithm works best when $r^2 = 10^{-3}$, when we use the third derivative for vertical smoothness and when B_3 works on the lowest pixel row and on the highest two rows of pixels in the grid. The tests also show that the results are not very sensitive to the precise settings.

Because the algorithm is stated in general terms and does not depend on any specific model, its applicability surpasses the ionosphere. With a slight modification in function $O(\boldsymbol{x})$, it has proven itself in quite another field: diagnostics of tokamak plasma by visible light emission tomography (Ingesson 1995). Due to the complexity of tokamak machines, it is impossible to install a sufficient number of detectors around the plasma. As a result, the coverage of the line integrals is poor. This gives rise to the same type of problems as those in tomography of the ionosphere. The a priori information on the tokamak plasma emissivity is remarkably similar to that used above: the emissivity cannot be negative, it is low near the walls of the vessel and the emissivity profile is basically smooth.

4.4 Tests

The idea behind a reconstruction algorithm may be convincing and clear, only tests can properly judge its merits. In this section we summarize the results of such tests. Before we discuss our own tests, we mention the results of a study that compared the performance of different reconstruction algorithms on a set of trial data (Raymund 1995). A precursor of the present algorithm competed in this comparative study (the positivity constraints, $\boldsymbol{x} \geq \mathbf{o}$, were not yet incorporated). It elicited the following judgement:

> '... The error image is unique among the methods. This algorithm shows great promise even in this early stage of development.'

Our own tests were designed so as to resemble reality as much as possible, with an array of five receivers at the same latitude, longitude and altitude as in the experiment (see section 6.1). The array length is 10^o of latitude. We used the same satellite trajectory for all tests: a circular polar orbit at 1100 km altitude with the earth rotating underneath, the satellite's longitude therefore decreases during the passage. The maximum satellite elevation is 89^o.

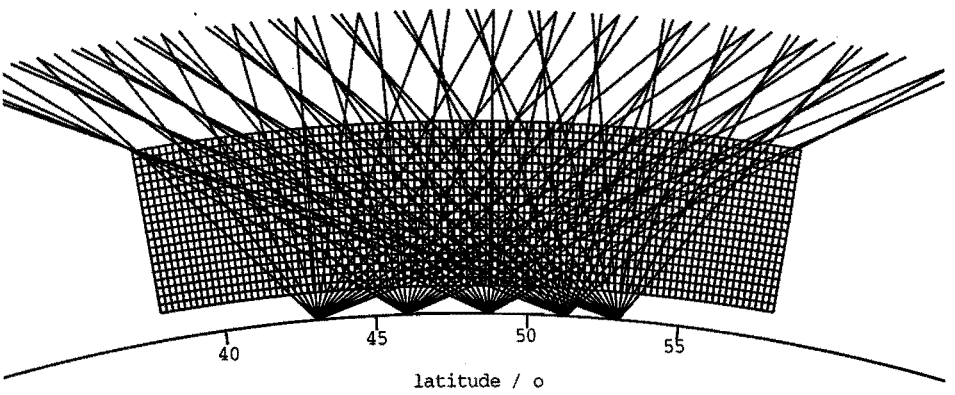

Figure 4.3: The grid of reconstruction and the lines of sight of the pseudo measurements. One in seven on a total of 525 lines of sight are drawn. The grid measures 100 × 20 pixels sized 0.2° × 30 km.

The geometry's projection on the plane of a meridian is shown in figure 4.3. The grid of reconstruction is also drawn, it consists of 100 pixels of 0.2° in the latitudinal direction, and 20 pixels of 30 km in the vertical direction, giving a coverage from 100 km to 700 km altitude. The electron density is supposed to be zero above and below the grid. One out of seven lines of sight are indicated. The integration period was 4.6 seconds, corresponding to the receivers' integration time. Lines of sight that leave the grid at the side are not used, because they traverse a region outside the grid where electron density cannot be neglected. This geometry sets a lower limit to the minimum elevation of usable lines of sight: 14°. In its turn, this reduces the effective pass duration to about 10 minutes. The total number of lines of sight is 525, and the total number of data points is five less, because of the differential nature of the data. The system of equations is therefore underdetermined: 2000 unknowns (pixels) and 520 data points.

We corrupted the pseudo-measurements with realistic errors with a double sided exponential distribution and a magnitude of five counts (see section 2.9). By computing the pseudo-measurements from phantom-ionospheres defined on a grid that was four times finer (twice the number of vertical and horizontal divisions: four times as much pixels) than the reconstruction grid, we simulated the discretization errors.

The top images of figures 4.4 to 4.6 are contour plots of phantom ionospheres. They basically have a Chapman profile (section 1.3) with parameters: $N_{e,\max} = 2 \times 10^5$ cm^{-3}, $H_{\max} = 200$ km and $H_{\text{scale}} = 50$ km. One phantom has some additional large scale structure (figure 4.4) and another is disturbed by an idealized travelling ionospheric disturbance, or TID (figure 4.5). The contours connect points of identical electron density. The contour scale is linear and the density at the highest contour is given at the right. The second image is a reconstruction based on pseudo measurements on the phantom in the top. The third and fourth images are reconstructions based on the same phantom, although shifted in height to $H_{\max} = 300$ km and $H_{\max} = 500$ km, respectively (altitudes given at the right). Images

of the shifted phantoms are omitted to save space and to ease comparison. The oblique lines in the reconstructions represent the outermost lines of sight. Outside these, there is no experimental information and the reconstruction is a stratified continuation. This is a result of the a priori information. At the right, the measurement error and the discretization error are indicated. Because the measurement error is absolute (5 counts), its relative size varies. The reconstruction error is also given, although this quantity is not very indicative of the quality of the reconstruction.

What can we conclude from these tests? The latitudinal structure (figures 4.4 and 4.5) is recovered well. The vertical profile constitutes a problem. First, the algorithm often has problems estimating the height of maximum electron density, as indicated at the right of the reconstructions. In the worst case, it is 90 km in error. The deviation is generally towards the center of the reconstruction. Second, the reconstructed vertical profile is often too smooth, but remember that the smoothness forms part of the prior knowledge! The spreading of the vertical profile results in an underestimate of the maximum density, which can be as much as one third. These effects are especially clear for the reconstructions from phantoms with $H_{\max} = 300$ km. The other profiles are not smeared out as much, because their maxima are closer to the upper or lower edge, where the reconstruction is forced to low densities.

Although recovery of the vertical profile forms a problem, the tests clearly demonstrate that the algorithm can estimate a layer's height with some success. Of course, the problem of the vertical profile is a consequence of the lack of horizontal lines of sight. In section 4.1.2, the problem of the vertical profile was illustrated by a purely stratified ionosphere over a flat earth. In that case, reconstruction of the layer's height is impossible. It was also said that some of the information on the vertical structure is preserved by the curvature of the earth. In figure 4.6, we see that the algorithm is indeed capable of differentiating between purely stratified ionospheres at different altitudes. In the same section, we reasoned that the stratified structure of the ionosphere aggravates the problem of the missing horizontals. This effect is illustrated by figures 4.6 and 4.7. Here we see that the height of an isolated bulge is reconstructed much more accurately than the height of a layer, even though the relative measurement and discretization errors are much larger for the bulge-phantom.

In figure 4.8, we see the effect of a decrease in the number of receivers. The second image in this figure shows that loss of one receiver reduces the detail in the reconstruction above the receiver. Image three and four illustrate the trade-off between receiver spacing and total array length. In the third image, data from receivers 2 and 4 is omitted, i.e. the total array length remains the same, while receiver spacing increases. This decreases resolution and contrast. In the bottom image, the outermost receivers (1 and 5) are ignored, which corresponds to a decrease in array length, while the receiver spacing remains unaltered. The effect is a smaller field of view.

The effect of an error in the estimate of the misfit is shown in figure 4.9. A misfit that is overestimated by a factor 5 (top image), leads to too much regularization and the reconstruction is too smooth. A gross underestimate, only 1 % of the expected misfit, gives slightly too much detail in the reconstruction. We conclude that the solution is not very sensitive to an error in the misfit's estimate. The lower two images show the result of changing measurement errors. An increase of the error by a factor 5 has much the same effect as an overestimate of the misfit by the same factor, which is no surprise. It seems that a total absence of errors only slightly increases the reconstruction quality. This indicates that below a certain level of data error, the flaws in the reconstruction are caused by the lack of information

and not so much by the errors.

In the last figure (4.10), we see the failure of the method to notice a tilt in the layer. With the help of two ionosondes, some of the tilt is restored. One ionosonde is located at 44° and the other at 56° latitude. The algorithm adds equality constraints for a vertical column of pixels from the ionosonde up to the height of maximum electron density.

Other tests (not presented) show that the method cannot reconstruct an ionosphere with a composite vertical profile that consists of two layers. Instead, the reconstruction displays an ionosphere with a single peak. The inaccuracies in the reconstructed vertical profile illustrate that the reconstructions do not provide accurate, detailed and reliable cross-sections of the ionosphere. Still, the reconstructions can give a rough idea of the ionosphere's state and structure. The limitation finds its root in the problem of the missing horizontals. In my opinion, it is the basic limitation in tomography of the ionosphere and therefore common to all reconstruction techniques.

4.5 Conclusions

Let us briefly summarize the results of the last two sections. Concerning the algorithm itself, we conclude from section 4.3:

- The method presented is a new and to a high degree model independent algorithm for ionospheric tomography.
- The fact that it is model independent makes it very suitable for fundamental ionospheric research.
- The solution to the inverse problem is formulated as the solution of a constrained optimization problem, where the a priori knowledge is cast in a precise mathematical form.
- The experiment defines one constraint to the optimization, the other constraints come from the prior knowledge that the electron density cannot be negative. The objective function of the optimization is defined by three more pieces of a priori information: the ionosphere is basically stratified, it is basically smooth and electron density is low at high and low altitudes.
- The strict mathematical prescription of the solution allows easy interpretation of the solution and satisfies the Bertero and Tikhonov criteria (section 3.2).
- Additional information from ionosondes can easily be incorporated by adding extra equality constraints in the optimization problem. Here, every additional constraint corresponds to a pixel that has its electron density measured by the ionosonde.

In section 4.4, the algorithm was tested on data generated by realistic simulation. The main conclusions on the algorithm's behaviour are:

- The algorithm works well and it is stable.
- The latitudinal structure is reconstructed well.

- The reconstruction of the vertical structure is reasonable: the estimate of $H_{\max}$ can be as much as 90 km in error, and a composite layer cannot be resolved from a single layer.
- The contribution of the prior knowledge to the solution can easily be discerned:
  - outside the outermost lines of sight, the reconstruction is a stratified continuation,
  - the electron density is low at the upper and lower edge of the grid,
  - the vertical profile is generally (too) smooth, which may result in an underestimate of the maximum density by as much as one third.
- The height of an isolated bulge in electron density is recovered much more accurately than the height of a layer.
- The reconstructions give a rough idea of the ionosphere's state and structure, but they do not provide accurate, detailed and reliable cross-sections. This limitation finds its root in the problem of the missing horizontals and it is the basic limitation in tomography of the ionosphere.

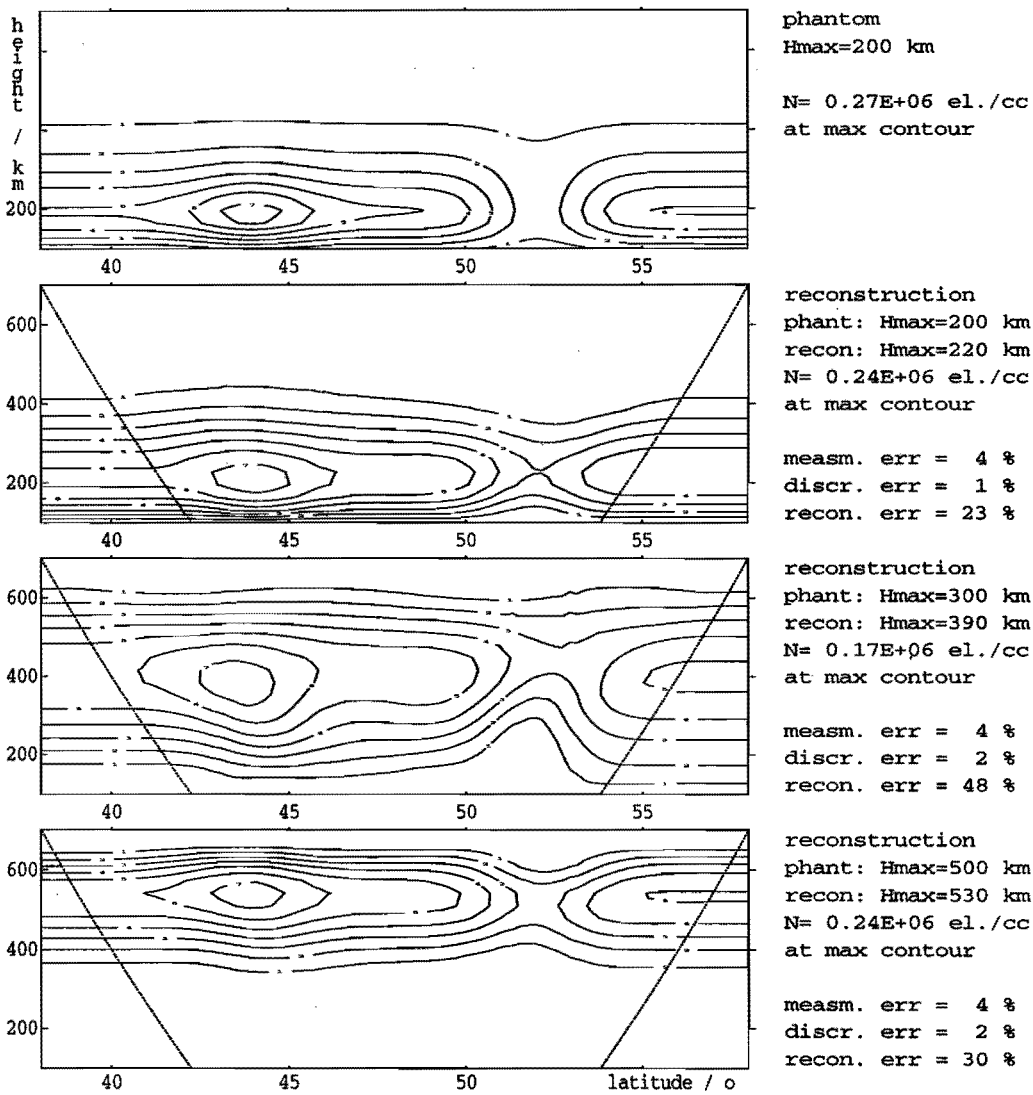

Figure 4.4: Phantom (top) and reconstructions for ionosphere with some structure. Reconstructions from pseudo measurements on phantoms with different $H_{\max}$. The latitudinal structure is recovered more reliably than the vertical profile. This can be concluded from the difference between the original and reconstructed $H_{\max}$, indicated at the right.

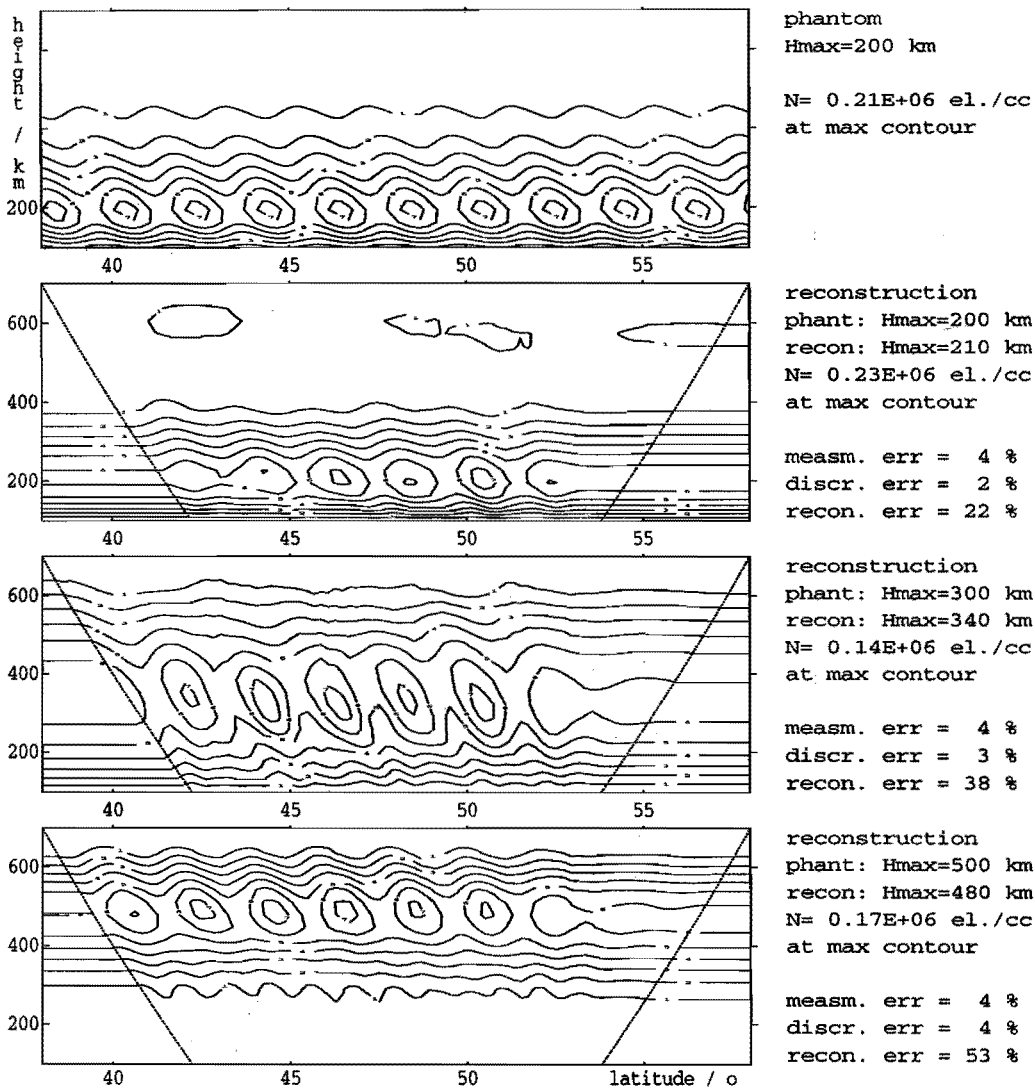

Figure 4.5: Phantom (top) and reconstructions (with different $H_{\max}$) for ionosphere with travelling ionospheric disturbance, or TID. The TID has latitudinal wavelength 2°, amplitude 15 % and southward tilt 30°. Reconstructions from pseudo measurements on phantoms with different $H_{\max}$. TID structure north of the northernmost receiver is not reconstructed. This is due to the tilt. Lines of sight heading for the upper right corner subsequently intersect a maximum and a minimum of the TID. As a result, the TID is not seen.

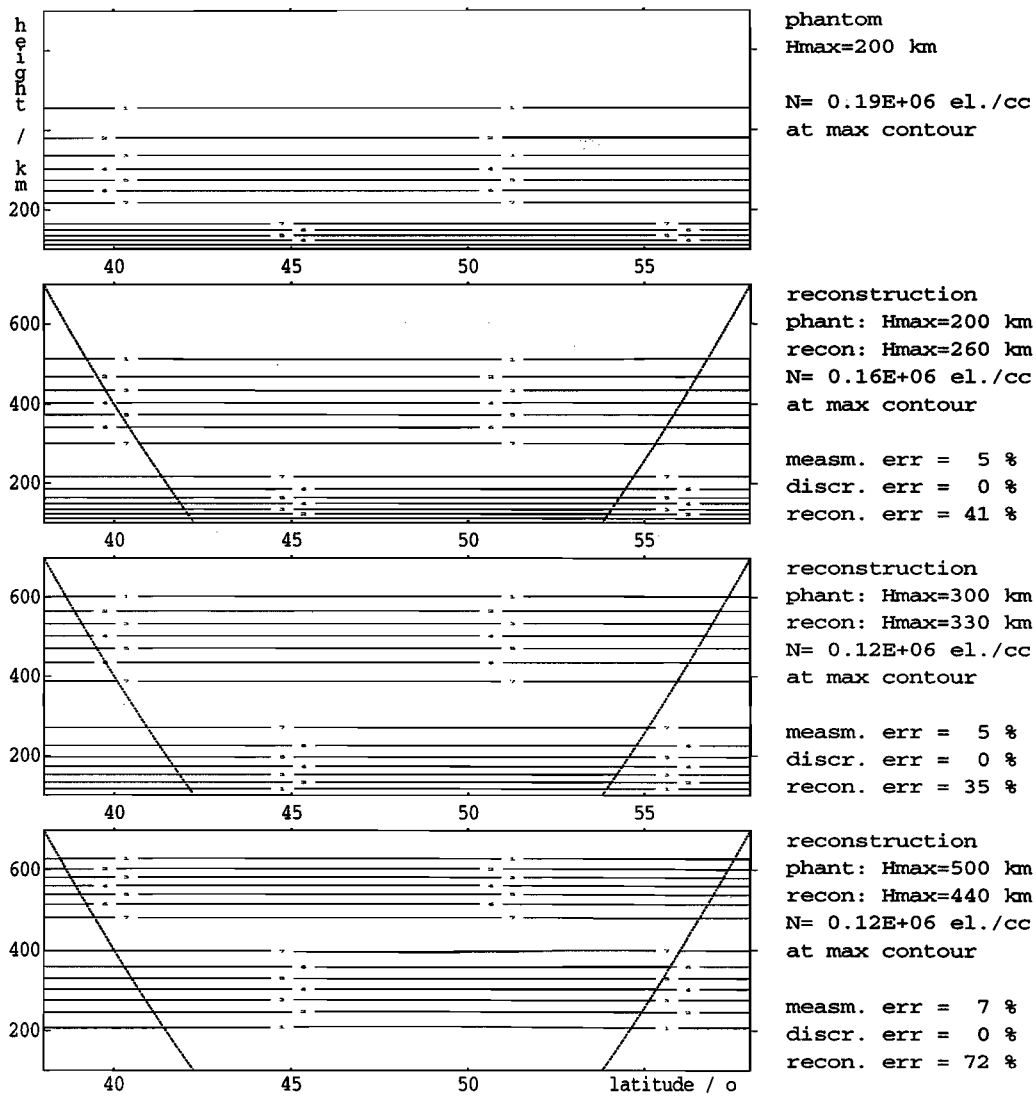

Figure 4.6: Phantom (top) and reconstructions for purely stratified ionosphere. Reconstructions from pseudo measurements on phantoms with different $H_{\max}$. As in the previous 2 figures, the layer's height is estimated with moderate success.

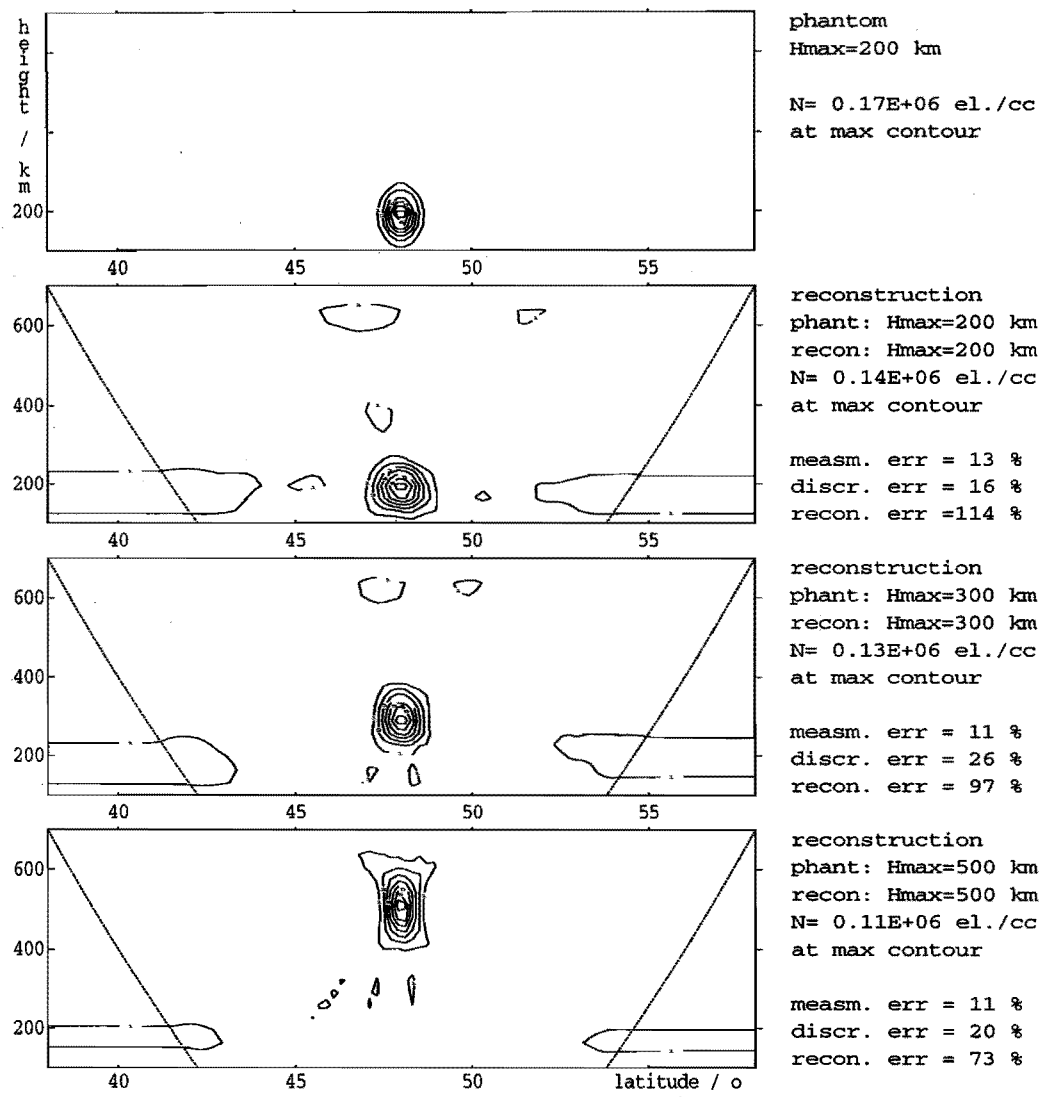

Figure 4.7: Bulge shaped phantom (top) and reconstructions for bulge at different heights. It is clear that the height of an isolated feature is reconstructed perfectly, in contrast to the height of a layer (figure 4.6).

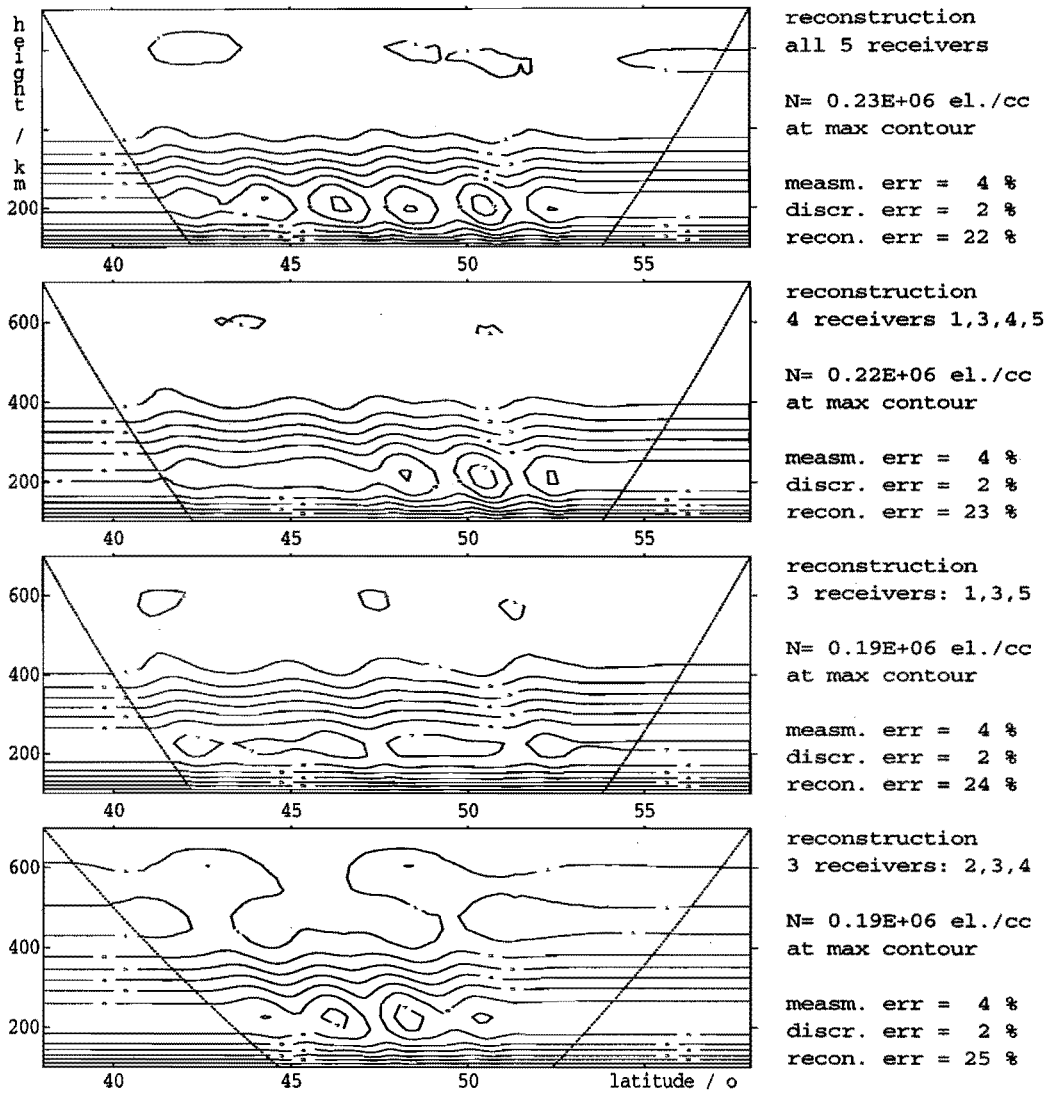

Figure 4.8: The effect of a reduced number of receivers. The phantom (not shown) is the same as in figure 4.5. In the second image, receiver number 2 at latitude 46.2° is removed. In the third image, receivers number 2 and 4 are taken out, which means that the spacing increases while the total length of the array remains the same. In the bottom image, receivers 1 and 5 are taken out, which reduces the array length but leaves the spacing unaltered. It follows that an increase in receiver spacing reduces contrast and resolution, whereas a decrease in the total array length narrows the field of view.

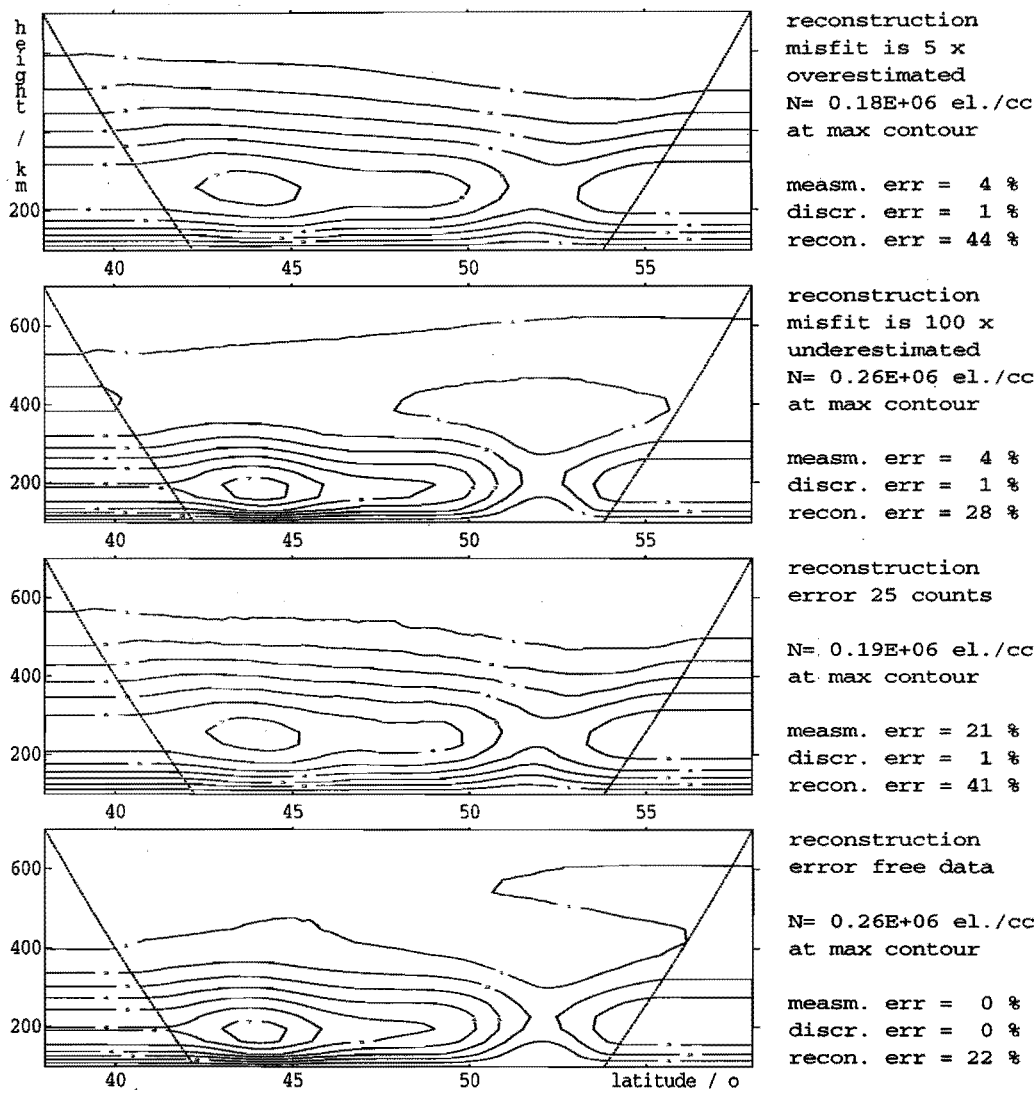

Figure 4.9: The effect of wrong misfit estimate (upper pair of images) and changing measurement errors (lower pair). The phantom (not shown) is the same as in figure 4.4. An overestimate of the misfit results in an overly smooth picture, while an underestimate gives slightly too much detail. The effect of varying measurement error is strikingly similar to that of the erroneous misfit estimate.

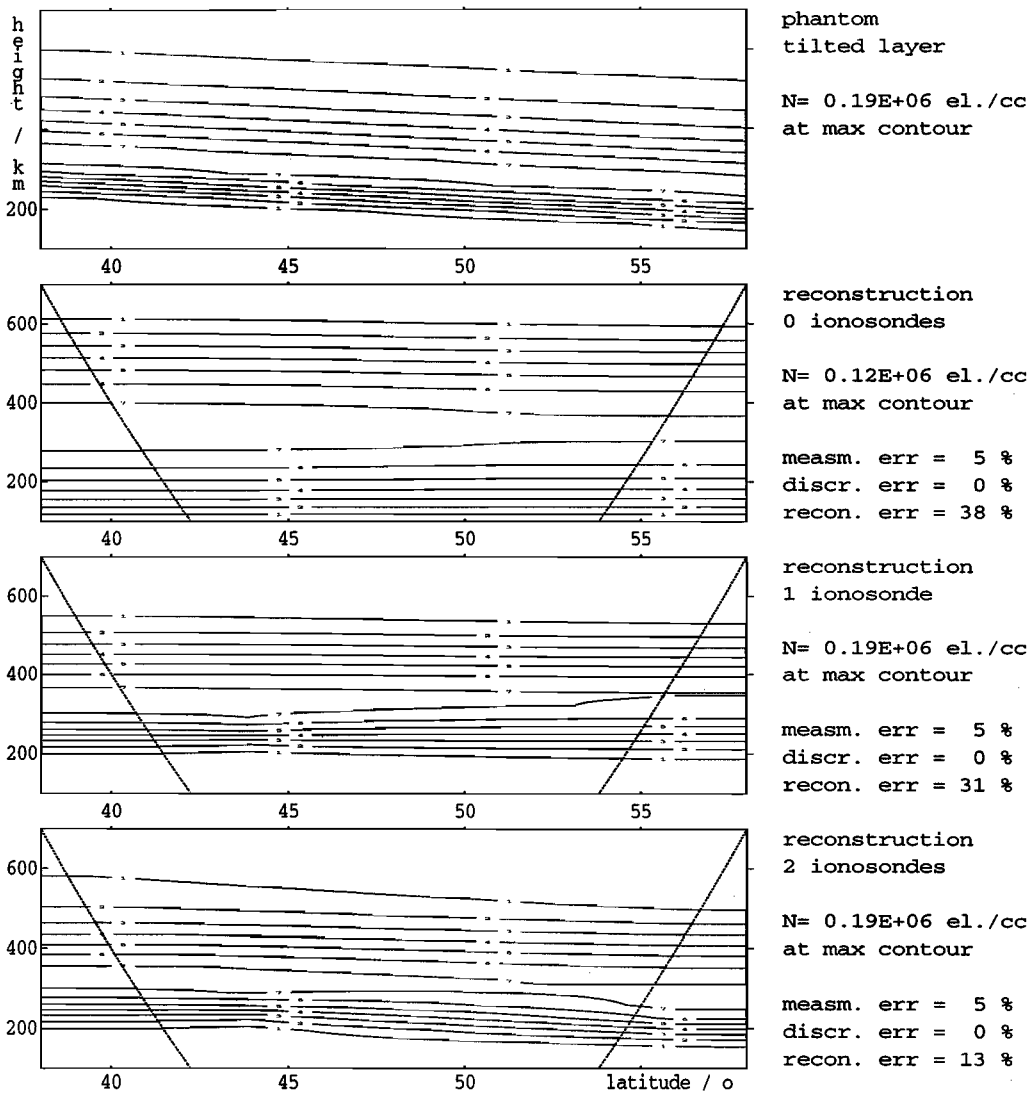

Figure 4.10: At the top a phantom with a tilted layer. Only with the aid of two ionosondes, the tilt can be reconstructed. One ionosonde (at 44° latitude, third image) does not help, but one ionosonde more (at 56° latitude, bottom image) does.

Chapter 5

Constrained optimization

This chapter presents the mathematical details of a constrained optimization algorithm, which is designed to tackle inverse problems.

5.1 Formulation and strategy

To complete the algorithm from section 4.3, we must solve the constrained optimization problem:

$$\min_{\boldsymbol{x}\in\mathcal{S}} O(\boldsymbol{x}), \quad \mathcal{S} = \{\boldsymbol{x} \in \mathrm{R}^n \mid \|A\boldsymbol{x} - \boldsymbol{d}\| = E \ \wedge \ \boldsymbol{x} \geq \mathbf{o}\} \tag{4.5}$$

The feasible set $\mathcal{S}$ is defined by n inequality constraints to impose positivity ($\boldsymbol{x} \geq \mathbf{o}$), plus one equality constraint ($\|A\boldsymbol{x} - \boldsymbol{d}\| = E$), which is provided by the experiment. The object function $O(\boldsymbol{x})$ contains a priori information. $O(\boldsymbol{x})$ is a quadratic function defined by

$$O(\boldsymbol{x}) = \|B_1\boldsymbol{x}\|^2 + r^2\|B_2\boldsymbol{x}\|^2 + \|B_3\boldsymbol{x}\|^2 \ . \tag{4.6}$$

Here, the Euclidean norm is understood. We assume that the experiment is specific enough to add to the prior knowledge. This means that a point most likely in the a priori sense, i.e. where $O(\boldsymbol{x})$ is minimal, should not satisfy the experiment to within the measurement error:

$$\boldsymbol{x}' \text{ solves } \min_{\boldsymbol{x}\in\mathrm{R}^n} O(\boldsymbol{x}) \quad \longrightarrow \quad \|A\boldsymbol{x}' - \boldsymbol{d}\| > E \tag{5.1}$$

If (5.1) were not true, the experiment would not contribute to the solution. Instead, the solution would be completely defined by the a priori information, a pathological situation.

As O is a convex function, it has no local minima. From (5.1) follows that the minimum of O is not in the set $\{\boldsymbol{x} \in \mathrm{R}^n \mid \|A\boldsymbol{x} - \boldsymbol{d}\| \leq E\}$. Therefore, we may just as well replace the equality constraint $\|A\boldsymbol{x} - \boldsymbol{d}\| = E$ by the inequality constraint $\|A\boldsymbol{x} - \boldsymbol{d}\| \leq E$. It also follows that this constraint is active, which means that the solution would change if the constraint were abandoned. This seemingly pointless redefinition of the constraint ensures that the Lagrange multiplier for this constraint is larger than zero. In the following sections, we will make good use of this knowledge.

The general approach to solve a constrained optimization problem is the method of the Lagrange multipliers. This method introduces a Lagrange multiplier for every constraint, and produces a set of conditions (the Kuhn-Tucker conditions) that the solution must satisfy. These Kuhn-Tucker (KT) conditions are a system of equations and inequalities. The solution

of this system is the solution to the constrained optimization problem. In general, the complexity of a constrained optimization problem increases with the number of constraints. To be more precise, the complexity increases with the number of active constraints, because inactive constraints can be ignored. It is clear that knowledge about which constraint is active and which is not, simplifies the constrained optimization. Above, we have seen that the constraint $\|A\boldsymbol{x} - \boldsymbol{d}\| \leq E$ is active.

The power of the algorithm presented in this section, resides in the fact that the solution is rewritten as a function of the Lagrange multipliers. This reformulation is, in terms of computational effort, the greatest part of the work. The next and relatively quick step, is to solve the Lagrange multipliers from the set of constraints. Because the number of active constraints is generally smaller than the number of unknowns in the solution vector, this approach reduces computing time considerably.

We rewrite the constrained optimization problem into the following general form. Consider two continuous quadratic functions, $O(\boldsymbol{x})$ and $g(\boldsymbol{x})$, the object function and the constraint function respectively:

$$O: \mathrm{R}^n \rightarrow \mathrm{R}, \quad O(\boldsymbol{x}) = \boldsymbol{x}^t B\boldsymbol{x} + 2\boldsymbol{b}^t\boldsymbol{x} , \tag{5.2}$$

$$g: \mathrm{R}^n \rightarrow \mathrm{R}, \quad g(\boldsymbol{x}) = \boldsymbol{x}^t C\boldsymbol{x} + 2\boldsymbol{c}^t\boldsymbol{x} + e . \tag{5.3}$$

Here, e is a scalar, $\boldsymbol{x}, \boldsymbol{b}, \boldsymbol{c}$ are real n-vectors and B and C are real, symmetric and positive semidefinite $(n \times n)$ matrices; ^{t} indicates the transpose. We define the constrained optimization problem and the feasible set $\mathcal{S}'$ by

$$\min_{\boldsymbol{x} \in \mathcal{S}'} O(\boldsymbol{x}), \quad \mathcal{S}' = \{\boldsymbol{x} \in \mathrm{R}^n \mid g(\boldsymbol{x}) \leq 0 \ \wedge \ \boldsymbol{x} \geq \mathbf{o}\} , \tag{5.4}$$

which is equivalent to the original optimization problem (4.5), if $O(\boldsymbol{x})$ is convex and if (5.1) is satisfied. Rewriting (4.6) to (5.2) gives $B = B_1^t B_1 + r^2 B_2^t B_2 + B_3^t B_3$, and $\boldsymbol{b} = \mathbf{o}$. Likewise,

$$g(\boldsymbol{x}) = \|A\boldsymbol{x} - \boldsymbol{d}\|^2 - E^2 , \tag{5.5}$$

from which follows: $C = A^t A$, $\boldsymbol{c} = -\boldsymbol{d}^t A$, and $e = \boldsymbol{d}^t\boldsymbol{d} - E^2$. The definition of matrices B and C ensures that they are symmetric and positive (semi)definite. The Hessian matrices of the functions f and g are $2B$ and $2C$ respectively. Because these matrices are positive semidefinite, the functions f and g are convex. As g is a convex function, the set $\{\boldsymbol{x} \in \mathrm{R}^n \mid g(\boldsymbol{x}) \leq 0\}$ is convex, as is the set $\{\boldsymbol{x} \in \mathrm{R}^n \mid \boldsymbol{x} \geq \mathbf{o}\}$. This guarantees that their intersection, $\mathcal{S}'$, is a convex set as well. $\mathcal{S}'$ is also a closed set.

We will find a solution to the constrained optimization problem (5.4) if: (I) the feasible set $\mathcal{S}'$ is not empty and (II) the kernels of B and C only have the nilvector in common. The second condition is written as

$$\ker(B) \cap \ker(C) = \{\mathbf{o}\} . \tag{5.6}$$

This condition is quite logical. It merely states that the subspace of solution space that goes unnoticed in the experiment, $\ker(C)$, does not overlap with the subspace towards which the a priori information is indifferent, $\ker(B)$. In other words, there may be no vectors that are both invisible to the experiment and to the a priori information, since those are the only criteria to discriminate them. Similarly, the solution is stable if there exists no vector $\boldsymbol{z}$ for which both $\|B\boldsymbol{z}\|$ and $\|C\boldsymbol{z}\|$ are very small.

5.2 The Kuhn-Tucker conditions

The KT conditions to the constrained optimization problem (5.4) are given by

$$\nabla O(\boldsymbol{x}) + \lambda \nabla g(\boldsymbol{x}) + \sum_{i=1}^{n} l_i \nabla(-2x_i) = \mathbf{o} , \tag{5.7}$$

$$\text{where} \quad \lambda g(\boldsymbol{x}) = 0 , \tag{5.8}$$

$$\lambda \geq 0 , \tag{5.9}$$

$$g(\boldsymbol{x}) \leq 0 , \tag{5.10}$$

$$\text{and for all } i = 1, ..., n \quad l_i x_i = 0 , \tag{5.11}$$

$$l_i \geq 0 , \tag{5.12}$$

$$x_i \geq 0 . \tag{5.13}$$

Here, the set of Lagrange multipliers (λ, l_i) is introduced, one multiplier for every constraint: λ for $g(\boldsymbol{x}) \leq 0$ and l_i for $x_i \geq 0$. We are going to find a point that meets the KT conditions. This point solves the constrained optimization problem. Let $\boldsymbol{l}$ be the n-vector with elements l_i. The first KT condition, equation (5.7), gives

$$2B\boldsymbol{x} + 2\boldsymbol{b} + 2\lambda C\boldsymbol{x} + 2\lambda \boldsymbol{c} - 2\boldsymbol{l} = \mathbf{o} , \tag{5.14}$$

or

$$[B + \lambda C]\boldsymbol{x} = \boldsymbol{l} - \boldsymbol{b} - \lambda \boldsymbol{c} . \tag{5.15}$$

Because B and C are both positive semidefinite, the inverse of the matrix $[B + \lambda C]$ exists if $\lambda > 0$ and if condition (5.6) is satisfied. When we find a general expression for the inverse, we can rewrite the solution as a function of the Lagrange multipliers:

$$\boldsymbol{x} = \boldsymbol{x}(\lambda, \boldsymbol{l}) = [B + \lambda C]^{-1}(\boldsymbol{l} - \boldsymbol{b} - \lambda \boldsymbol{c}) . \tag{5.16}$$

5.3 The matrix pencil

In the literature, $[B + \lambda C]$ is referred to as a matrix pencil (e.g. Gantmacher 1959, Parlett 1980). Our pencil is symmetric and, by condition (5.6), regular. For regular pencils, it is possible to derive a closed expression for the inverse $[B + \lambda C]^{-1}$. One method is based on the generalized eigenvalue problem, as we now show. Another method is based on the generalized singular value decomposition, to which we will return at the end of the section.

Because B and C are symmetric and positive semidefinite and because of (5.6), matrix $B+C$ is symmetric and positive-definite. Therefore matrix $[B+C]^{-\frac{1}{2}}$ exists and is symmetric and positive definite. We write

$$[B + \lambda C]^{-1} = [B + C]^{-\frac{1}{2}} \left[I_n + (\lambda - 1)[B + C]^{-\frac{1}{2}} C [B + C]^{-\frac{1}{2}} \right]^{-1} [B + C]^{-\frac{1}{2}} , \tag{5.17}$$

where I_n is the identity matrix of order n. We are going to diagonalize the matrix between brackets:

$$I_n + (\lambda - 1)[B + C]^{-\frac{1}{2}} C [B + C]^{-\frac{1}{2}} . \tag{5.18}$$

To this end, we consider the eigenvalue problem

$$[B+C]^{-\frac{1}{2}}C[B+C]^{-\frac{1}{2}}|u_i\rangle = \mu_i|u_i\rangle \ , \tag{5.19}$$

where we use Dirac notation. As the matrix in (5.19) is symmetric and positive semidefinite, the eigenvalues satisfy

$$\mu_i \geq 0 \ , \quad i = 1, \ldots, n \ . \tag{5.20}$$

As the matrix in (5.19) is symmetric, the spectral theorem states that $|u_i\rangle$ is a complete set of normalized orthogonal eigenvectors:

$$\langle u_i|u_j\rangle = \delta_{ij} \ \text{ and } \ \sum_{i=1}^{n} |u_i\rangle\langle u_i| = I_n \ . \tag{5.21}$$

Let

$$|y_i\rangle = [B+C]^{-\frac{1}{2}}|u_i\rangle \ , \tag{5.22}$$

then (5.19) becomes the generalized eigenvalue problem

$$C|y_i\rangle = \mu_i[B+C]|y_i\rangle \ . \tag{5.23}$$

The final solution will be given in terms of the generalized eigenvectors $|y_i\rangle$ and eigenvalues μ_i. Therefore, the solution of the generalized eigenvalue problem forms the heart of the algorithm. There are many software libraries with routines to do this job.

From equation (5.23) it is not difficult to see that there are no eigenvalues μ_i larger than 1, this gives with (5.20)

$$0 \leq \mu_i \leq 1 \ , \quad i = 1, \ldots, n \tag{5.24}$$

and

$$\mu_i = 0 \ \longleftrightarrow \ |y_i\rangle \in \ker(C) \ , \tag{5.25}$$

$$\mu_i = 1 \ \longleftrightarrow \ |y_i\rangle \in \ker(B) \ . \tag{5.26}$$

We also know that

$$\langle y_i|C|y_j\rangle = \mu_i\langle y_i|B+C|y_j\rangle = \mu_i\langle u_i|u_j\rangle = \mu_i\delta_{ij} \ . \tag{5.27}$$

The normalized orthogonal eigenvectors and the eigenvalues of the matrix in (5.18), are $|u_i\rangle$ and $1+(\lambda-1)\mu_i$ respectively. Therefore

$$\left[I_n + (\lambda-1)[B+C]^{-\frac{1}{2}}C[B+C]^{-\frac{1}{2}}\right]^{-1} = \sum_{i=1}^{n} \frac{|u_i\rangle\langle u_i|}{1+(\lambda-1)\mu_i} \tag{5.28}$$

and after left and right multiplication of (5.28) with $[B+C]^{-\frac{1}{2}}$

$$[B+\lambda C]^{-1} = \sum_{i=1}^{n} \frac{|y_i\rangle\langle y_i|}{1+(\lambda-1)\mu_i} \ . \tag{5.29}$$

Substitution of (5.29) into (5.16) gives the solution

$$|x\rangle = \sum_{i=1}^{n} \frac{\langle y_i|l-b\rangle - \lambda\langle y_i|c\rangle}{1+(\lambda-1)\mu_i}|y_i\rangle \ . \tag{5.30}$$

We promised to conclude with a few words on the generalized singular value decomposition. The generalized singular value decomposition (Golub and van Loan 1989) provides a linear and nonsingular transformation X, such that $X^tBX = \Sigma_B$ and $X^tCX = \Sigma_C$ are both diagonal matrices. This gives for the inverse of the pencil $[B + \lambda C]^{-1} = X[\Sigma_B + \lambda\Sigma_C]^{-1}X^t$, which is easy to compute because the matrix between brackets is diagonal. It is easy to show that the columns of matrix X are the same as the generalized eigenvectors $|y_i\rangle$, which illustrates the similarity between the generalized eigenvalue problem and the generalized singular value decomposition. The remainder of this chapter does not depend very much on which of the methods is used.

5.4 The Lagrange multipliers

The effort of the preceding section has yielded a closed expression (5.30) for the solution as a function of the Lagrange multipliers λ and $\boldsymbol{l}$. Now we need to know the Lagrange multipliers. This section shows how to compute the Lagrange multipliers from the constraints. We will proceed in two steps. In the first step, we only consider the constraint $g(\boldsymbol{x}) \leq 0$. In the second step, the positivity bounds $\boldsymbol{x} \geq \mathbf{o}$ are also included. The inclusion of positivity is really an iterative process that involves both steps. The solution is found in the space of the Lagrange multipliers. Because there are relatively few active constraints, this process is much faster than finding the solution directly in solution space.

5.4.1 Without positivity constraints

As we only consider the constraint $g(\boldsymbol{x}) \leq 0$, we have dropped the positivity constraints, which implies that we do not consider $\boldsymbol{l}$. This leaves only λ to be determined.

The prior information has told us that we can replace the equality constraint by an inequality constraint. This has given us $\lambda \geq 0$. We also know that the constraint is active, which tells us $\lambda > 0$ and $g(\boldsymbol{x}) = 0$. In other words, the KT conditions (5.8) through (5.10) reduce to

$$\lambda > 0 , \tag{5.31}$$

$$g(\boldsymbol{x}) = 0 . \tag{5.32}$$

Substitution of the solution (5.30) into $g(\boldsymbol{x}) = 0$, and using (5.27), gives an equation to which λ is the root:

$$0 = g(\boldsymbol{x}(\lambda)) = e + \sum_{i=1}^{n} \frac{[\lambda\langle c|y_i\rangle + \langle b - l|y_i\rangle]\,[(2\mu_i - 2 - \lambda\mu_i)\langle c|y_i\rangle + \mu_i\langle b - l|y_i\rangle]}{(1 + (\lambda - 1)\mu_i)^2} . \tag{5.33}$$

The function g decreases monotonically for $\lambda > 0$, because

$$\frac{\partial g}{\partial \lambda} = -2\sum_{i=1}^{n} \frac{[(1 - \mu_i)\langle c|y_i\rangle - \mu_i\langle b - l|y_i\rangle]^2}{(1 + (\lambda - 1)\mu_i)^3} \leq 0 , \tag{5.34}$$

$$\text{if } \lambda > 0 \quad \text{and} \quad 0 \leq \mu_i \leq 1 . \tag{5.35}$$

As a result, equation (5.33) has a root λ , $\lambda > 0$, if

$$\lim_{\lambda \downarrow 0} g(\boldsymbol{x}(\lambda)) \geq 0 \geq \lim_{\lambda \to \infty} g(\boldsymbol{x}(\lambda)) . \tag{5.36}$$

As g is a decreasing function of λ, it is straightforward to solve λ numerically from (5.33).

It is instructive to consider the solution (5.30) in the limits $\lambda \downarrow 0$ and $\lambda \to \infty$:

$$\lim_{\lambda \downarrow 0} \boldsymbol{x}(\lambda) \text{ exists} \quad \text{if} \quad \mu_i = 1 \text{ implies } \langle l - b | y_i \rangle = 0 \ , \tag{5.37}$$

$$\lim_{\lambda \to \infty} \boldsymbol{x}(\lambda) \text{ exists} \quad \text{if} \quad \mu_i = 0 \text{ implies } \langle c | y_i \rangle = 0 \ . \tag{5.38}$$

If these solutions exist, they are the minimizers of O and g on R^n:

$$\lim_{\lambda \downarrow 0} O(\boldsymbol{x}(\lambda)) = \min_{\boldsymbol{x} \in \mathrm{R}^n} O(\boldsymbol{x}) \ , \tag{5.39}$$

$$\lim_{\lambda \to \infty} g(\boldsymbol{x}(\lambda)) = \min_{\boldsymbol{x} \in \mathrm{R}^n} g(\boldsymbol{x}) \ . \tag{5.40}$$

In the appendix we proof the second statement (5.40), whereas the first statement can be proved along the same lines. As we see, $\lim_{\lambda \downarrow 0} \boldsymbol{x}(\lambda)$ corresponds to an unconstrained minimum of O and $\lim_{\lambda \to \infty} \boldsymbol{x}(\lambda)$ is determined solely by the constraint and corresponds to the minimum misfit solution.

The expression (5.30) fails if there is no root λ, $\lambda > 0$, to equation (5.33). This happens when either of the two inequalities in (5.36) is violated. When the left hand inequality is violated, the solution is an interior point of $\mathcal{S}'$ and (5.1) is not satisfied. The right hand inequality is violated when the feasible set $\mathcal{S}'$ is empty. In other words:

$$\lim_{\lambda \downarrow 0} g(\boldsymbol{x}(\lambda)) < 0 \quad \longleftrightarrow \quad \lim_{\lambda \downarrow 0} \boldsymbol{x}(\lambda) \text{ is interior point of } \mathcal{S}' \text{ and minimizer of } O \ , \tag{5.41}$$

$$\lim_{\lambda \to \infty} g(\boldsymbol{x}(\lambda)) > 0 \quad \longleftrightarrow \quad \mathcal{S}' = \emptyset \ . \tag{5.42}$$

Statement (5.41) follows from (5.39) and (5.42) follows from (5.40).

5.4.2 The positivity constraints

We now have a solution where the positivity constraints are not included. Some of these positivity constraints are probably violated. In this section, we describe the adaptation of the solution so that these constraints are no longer violated. The positivity constraints are directly coupled to an element of the solution vector and vice versa. It is important to know which positivity constraints are active. The indices of the active constraints constitute the active set $\mathcal{A}$. The inactive set $\mathcal{I}$ contains the indices of the inactive constraints and $\mathcal{A} \cup \mathcal{I} = \{1, 2, ..., n\}$. Let $\mathcal{A}$ contain p elements.

Which positivity constraints are active? Surely, an active constraint should violate the positivity constraint, i.e. the corresponding element of the solution $\boldsymbol{x}$ should be negative. As vector $\boldsymbol{x}$ is a discretization of a (two-dimensional) distribution (chapter 3), we guess that the active constraints correspond to the negative local minima in the distribution $\boldsymbol{x}$. By the imposed smoothness of the solution (via $O(\boldsymbol{x})$), the other (less) negative parts in the solution are likely to follow their neighbours, so that these constraints are satisfied as well. The active constraints are satisfied by the introduction of the vector $\Delta\boldsymbol{x}$,

$$\boldsymbol{x}^{new} = \boldsymbol{x}^{old} + \Delta\boldsymbol{x} \tag{5.43}$$

of which the 'active' elements satisfy:

$$\Delta x_j = -x_j \ , \quad j \in \mathcal{A} \ , \tag{5.44}$$

where the x_j are the negative local minima of the solution. We do not bother about the 'inactive' elements ($j \in \mathcal{I}$)of $\Delta \boldsymbol{x}$.

We are going to change the Lagrange multipliers in the active set by so much that (5.44) is satisfied, and thereby the active constraints. The other Lagrange multipliers must remain zero, because they are not in the active set. In other words, we want to update the vector of constraints by a vector $\Delta \boldsymbol{l}$,

$$\boldsymbol{l}^{new} = \boldsymbol{l}^{old} + \Delta \boldsymbol{l} \tag{5.45}$$

of which the 'inactive' elements satisfy:

$$\Delta l_j = 0 \quad , \quad j \in \mathcal{I} \; . \tag{5.46}$$

Because equation (5.16) is linear in $\boldsymbol{l}$, it follows that

$$\Delta \boldsymbol{x} = [B + \lambda C]^{-1} \Delta \boldsymbol{l} \; . \tag{5.47}$$

This is a system of n equations with n unknowns: p unknowns Δl_j , $j \in \mathcal{A}$ plus $(n-p)$ unknowns Δx_j , $j \in \mathcal{I}$. (The other Δl_j and Δx_j are given by (5.44) and (5.46).) Because we are not interested in the unknowns Δx_j , $j \in \mathcal{I}$, we remove them from the system (5.47). This gives

$$\Delta x_j = \sum_{i=1}^{n} \frac{\langle y_i | \Delta l \rangle}{1 + (\lambda - 1)\mu_i} \, |y_i\rangle_j \qquad j \in \mathcal{A} \; , \tag{5.48}$$

where we have used equation (5.30). This is a system of p equations, with p unknowns (Δl_j , $j \in \mathcal{A}$). Solution of this system gives an update of the Lagrange multipliers. The new set of Lagrange multipliers must be checked for positivity, condition (5.12). Those that fail this test must be removed from the active set $\mathcal{A}$. With the new set of Lagrange multipliers, we return to section 5.4.1, where the solution to equation (5.33) yields a new λ and equation (5.30) a new solution. This iterative process is repeated until all constraints are satisfied.

Here, we do not prove that this iterative process converges and indeed converges to the correct solution. Instead, we have tested the algorithm to both over- and underdetermined inverse problems in tomography of the ionosphere and of tokamak plasma emissivity. In all cases, the algorithm converges. These results were compared to the solutions of the constrained optimization algorithm from the NAG library (E04UCF) that finds successive approximations in solution space. Indeed the solutions were the same. Yet, the NAG (Numerical Algorithms Group) algorithm is slower than ours. Moreover, it fails for the large problems, where our algorithm works smoothly.

5.5 Practical use of the algorithm

The recipe for practical use of the algorithm is:

1. Solve the generalized eigenvalue problem (5.23), this is a n^3 process.
2. Calculate the inner products $\langle b|y_i\rangle$ and $\langle c|y_i\rangle$, n^2 processes.
3. Solve the Lagrange multiplier λ from (5.33), n^1 process.
4. Use the results in (5.30) to calculate the solution, n^2 process.

5. Check if solution satisfies the positiveness constraints, n^1 process. If it does, we are ready. If not, we continue.

6. Add negative local minima to the active set, n^1 process.

7. Solve $\Delta \boldsymbol{l}$ from (5.48) and update $\boldsymbol{l}$, p^3 process.

8. Check if the positivity constraints satisfy $l_j < 0$, p^1 process. If not, remove the violators from the active set and go to step 7.

9. Calculate the inner products $\langle l|y_i\rangle$, $n \times p$ process. Go to step 3.

For the stability of the algorithm, it is important that the matrices B and C are scaled so that their eigenvalues are of comparable size. If either B or C is positive definite, the algorithm can be simplified (see the appendix) and scaling is not necessary.

The heart and computationally most demanding part of the algorithm is the solution of the generalized eigenvalue problem. Routine F02AEF from the NAG library does this job very well. This routine takes advantage of the symmetry and also performs the right normalization. In our application, where $n = 2000$, the routine takes roughly 25 cpu minutes on a Silicon Graphics Power Challenge with R8000 processors. The rest of the algorithm takes only a few minutes, because the number p of active constraints is much smaller than n. Typically, $100 < p < 200$. The method has great advantages for successive problems where the measurement geometry remains the same, and therefore B and C. In that case, the real work (solution of the generalized eigenvalue problem) should be done only once. In tomography of the ionosphere, measurement geometry changes every satellite pass. In many other experiments, by contrast, measurement geometry remains the same over many reconstructions. We have mentioned tomography for tokamak plasma diagnostics, but there are many more industrial applications.

5.6 Appendix

In the derivation in section 5.3, it was assumed that the matrix-sum $B + C$ were positive definite. The derivation is simplified when either of the constituent matrices (B or C) is positive definite. In the following two subsections, these simplifications are given. In the last subsection, the proof of (5.40) is given.

5.6.1 Matrix C is positive definite

Matrix C is symmetric and positive-definite, therefore the matrix $C^{-\frac{1}{2}}$ exists and is symmetric and positive-definite. We write

$$[B + \lambda C]^{-1} = C^{-\frac{1}{2}} \left[C^{-\frac{1}{2}} B C^{-\frac{1}{2}} + \lambda I_n\right]^{-1} C^{-\frac{1}{2}} \tag{5.17a}$$

and diagonalize the matrix between brackets

$$C^{-\frac{1}{2}} B C^{-\frac{1}{2}} + \lambda I_n \ , \tag{5.18a}$$

for which we consider the eigenvalue problem

$$C^{-\frac{1}{2}} B C^{-\frac{1}{2}} |u_i\rangle = \mu_i |u_i\rangle \ . \tag{5.19a}$$

As the matrix in (5.19a) is symmetric and positive semidefinite, the eigenvalues satisfy

$$\mu_i \geq 0 \ , \quad i = 1, \ldots, n \ . \tag{5.20a}$$

As the matrix in (5.19a) is symmetric, the spectral theorem states that $|u_i\rangle$ is a complete set of normalized orthogonal eigenvectors:

$$\langle u_i|u_j\rangle = \delta_{ij} \ \text{ and } \ \sum_{i=1}^{n} |u_i\rangle\langle u_i| = I_n \ . \tag{5.21a}$$

Let

$$|y_i\rangle = C^{-\frac{1}{2}}|u_i\rangle \ , \tag{5.22a}$$

then (5.19a) becomes

$$B|y_i\rangle = \mu_i C|y_i\rangle \ . \tag{5.23a}$$

We also know that

$$\langle y_i|C|y_j\rangle = \langle u_i|u_j\rangle = \delta_{ij} \ . \tag{5.27a}$$

The normalized orthogonal eigenvectors and the eigenvalues of the matrix in (5.18a), are $|u_i\rangle$ and $\lambda + \mu_i$ respectively. Therefore

$$\left[C^{-\frac{1}{2}}BC^{-\frac{1}{2}} + \lambda I_n\right]^{-1} = \sum_{i=1}^{n} \frac{|u_i\rangle\langle u_i|}{\lambda + \mu_i} \tag{5.28a}$$

and after left and right multiplication of (5.28a) with $C^{-\frac{1}{2}}$

$$[B + \lambda C]^{-1} = \sum_{i=1}^{n} \frac{|y_i\rangle\langle y_i|}{\lambda + \mu_i} \ . \tag{5.29a}$$

Substituting (5.29a) in (5.16) gives the solution

$$|x\rangle = -\sum_{i=1}^{n} \frac{\langle y_i|b\rangle + \lambda\langle y_i|c\rangle}{\lambda + \mu_i}|y_i\rangle \ . \tag{5.30a}$$

Substitution of the solution (5.30a) into $g(\boldsymbol{x}) = 0$ gives an equation to which λ is the root:

$$0 = g(\boldsymbol{x}(\lambda)) = e + \sum_{i=1}^{n} \frac{-\lambda^2\langle c|y_i\rangle^2 \ - 2\mu_i\lambda\langle c|y_i\rangle^2 + \langle b - l|y_i\rangle^2 - 2\mu_i\langle b - l|y_i\rangle\langle c|y_i\rangle}{(\lambda + \mu_i)^2} \ . \tag{5.33a}$$

Here, we have used the relations (5.27a). Again, g decreases monotonically for $\lambda > 0$.

5.6.2 Matrix B is positive definite

Matrix B is symmetric and positive-definite, therefore the matrix $B^{-\frac{1}{2}}$ exists and is symmetric and positive-definite. We write

$$[B + \lambda C]^{-1} = B^{-\frac{1}{2}}\left[I_n + \lambda B^{-\frac{1}{2}}CB^{-\frac{1}{2}}\right]^{-1}B^{-\frac{1}{2}} \tag{5.17b}$$

and diagonalize the matrix between brackets

$$I_n + \lambda B^{-\frac{1}{2}}CB^{-\frac{1}{2}} \tag{5.18b} \ ,$$

for which we consider the eigenvalue problem

$$B^{-\frac{1}{2}}CB^{-\frac{1}{2}}|u_i\rangle = \mu_i|u_i\rangle \ . \tag{5.19b}$$

As the matrix in (5.19b) is symmetric and positive semidefinite, the eigenvalues satisfy

$$\mu_i \geq 0 \ , \quad i = 1, \ldots, n \ . \tag{5.20b}$$

As the matrix in (5.19b) is symmetric, the spectral theorem states that $|u_i\rangle$ is a complete set of normalized orthogonal eigenvectors:

$$\langle u_i|u_j\rangle = \delta_{ij} \ \text{ and } \ \sum_{i=1}^{n} |u_i\rangle\langle u_i| = I_n \ . \tag{5.21b}$$

Let

$$|y_i\rangle = B^{-\frac{1}{2}}|u_i\rangle \ , \tag{5.22b}$$

then (5.19b) becomes

$$C|y_i\rangle = \mu_i B|y_i\rangle \ . \tag{5.23b}$$

We know that

$$\langle y_i|C|y_j\rangle = \langle y_i|\mu_j B|y_j\rangle = \mu_j\langle u_i|u_j\rangle = \mu_j\delta_{ij} \ . \tag{5.27b}$$

The normalized orthogonal eigenvectors and the eigenvalues of the matrix in (5.18b), are $|u_i\rangle$ and $1 + \lambda\mu_i$ respectively. Therefore

$$\left[I_n + \lambda B^{-\frac{1}{2}}CB^{-\frac{1}{2}}\right]^{-1} = \sum_{i=1}^{n} \frac{|u_i\rangle\langle u_i|}{1 + \lambda\mu_i} \tag{5.28b}$$

and after left and right multiplication of (5.28b) with $B^{-\frac{1}{2}}$

$$[B + \lambda C]^{-1} = \sum_{i=1}^{n} \frac{|y_i\rangle\langle y_i|}{1 + \lambda\mu_i} \ . \tag{5.29b}$$

Substituting (5.29b) in (5.16) gives the solution

$$|x\rangle = -\sum_{i=1}^{n} \frac{\langle y_i|b\rangle + \lambda\langle y_i|c\rangle}{1 + \lambda\mu_i}|y_i\rangle \ . \tag{5.30b}$$

Substitution of the solution (5.30b) into $g(\boldsymbol{x}) = 0$ gives an equation to which λ is the root:

$$0 = g(\boldsymbol{x}(\lambda)) = e + \sum_{i=1}^{n} \frac{-\mu_i\lambda^2\langle c|y_i\rangle^2 \ - 2\lambda\langle c|y_i\rangle^2 + \mu_i\langle b - l|y_i\rangle^2 - 2\langle b - l|y_i\rangle\langle c|y_i\rangle}{(1 + \lambda\mu_i)^2} \ . \tag{5.33b}$$

Here, we have used use the relations (5.27b). Again, g decreases monotonically for $\lambda > 0$.

5.6.3 Proof of (5.40)

Because $g(|x\rangle)$ is a convex function, we know

$$|x'\rangle \text{ solves } \min_{|x\rangle \in \mathbb{R}^n} O(|x\rangle > \leftrightarrow \nabla g(|x'\rangle) = \mathbf{o} \leftrightarrow |c\rangle = -C|x'\rangle \,. \tag{5.49}$$

We now show that $\lim_{\lambda\to\infty} |x\rangle$ satisfies this condition.

$$\begin{aligned}
|c\rangle &= \lim_{\lambda\to\infty} -C|x(\lambda)\rangle && (5.50)\\
&= \sum_{\substack{i=1\\ \mu_i\neq 0}}^{n} \frac{\langle y_i|c\rangle}{\mu_i}\, C|y_i\rangle + \sum_{\substack{i=1\\ \mu_i=0}}^{n} \langle y_i|b\rangle\, C|y_i\rangle && (5.51)\\
&= \sum_{\substack{i=1\\ \mu_i\neq 0}}^{n} \langle y_i|c\rangle\, [B+C]|y_i\rangle && (5.52)\\
&= \sum_{i=1}^{n} \langle y_i|c\rangle\, [B+C]|y_i\rangle && (5.53)\\
&= \sum_{i=1}^{n} \langle u_i|[B+C]^{-\frac{1}{2}}|c\rangle\, [B+C]^{\frac{1}{2}}|u_i\rangle \,, && (5.54)\\
[B+C]^{-\frac{1}{2}}|c\rangle &= \sum_{i=1}^{n} \langle u_i|[B+C]^{-\frac{1}{2}}|c\rangle\, |u_i\rangle \,. && (5.55)
\end{aligned}$$

The last sum in (5.51) vanishes because of (5.25). In (5.53) the contribution of the extra $\mu_i = 0$ terms is zero, which we know from the condition in (5.38). As $|u_i\rangle$ is a complete orthonormal set, equation (5.55) just gives the orthogonal decomposition of $[B+C]^{-\frac{1}{2}}|c\rangle$. Therefore, the last equation is true, which completes the proof.

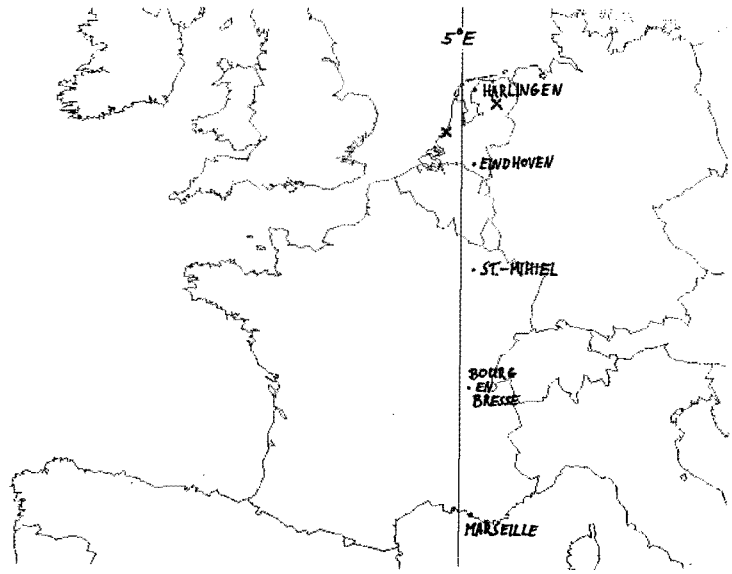

Figure 6.1: Map of receiver locations. The fifth degree of longitude is drawn. The receivers are located along the $5\frac{1}{2}^{\circ}$ E meridian over an extent of 1105 km. Crosses mark the positions of the chirpsounder's transmitter and receiver.

town	geographical coordinates	spherical coordinates	geomagnetic coordinates
Harlingen	lat = 53°.17321 lon = 5°.42502 height = 57 m	$\theta = 52°.98840$ $\phi = 5°.42502$ r = 6,364,532 m	$\Theta = 54°.2$ $\Phi = 88°.9$
Eindhoven	lat = 51°.44765 lon = 5°.49202 height = 72 m	$\theta = 51°.25994$ $\phi = 5°.49202$ r = 6,365,171 m	$\Theta = 52°.5$ $\Phi = 89°.7$
Saint-Mihiel	lat = 48°.89040 lon = 5°.53871 height = 274 m	$\theta = 48°.69967$ $\phi = 5°.53871$ r = 6,366,312 m	$\Theta = 50°.1$ $\Phi = 89°.1$
Bourg-en-Bresse	lat = 46°.20705 lon = 5°.22577 height = 306 m	$\theta = 46°.01477$ $\phi = 5°.22577$ r = 6,367,342 m	$\Theta = 47°.6$ $\Phi = 87°.7$
Marseille	lat = 43°.23151 lon = 5°.43976 height = 236 m	$\theta = 43°.03949$ $\phi = 5°.43976$ r = 6,368,382 m	$\Theta = 44°.7$ $\Phi = 86°.7$

Table 6.1: Coordinates of the antenna phase centers. The approximate geomagnetic coordinates are computed from the 1988 International Geomagnetic Reference Field.

Chapter 6

The experiment

This chapter describes the campaign and the results of an ionospheric tomography experiment. This experiment was conducted in spring 1995 and employed five receivers on the Eindhoven meridian, from Harlingen to Marseille.

6.1 The campaign

In the fall of 1994, the roof of the Physics Department of Eindhoven University of Technology had supported the antennas over a few months' time. On the highest floor, the receivers had been functioning well and confidence in the equipment was large enough to start preparations for a measurement campaign. The plan was to employ five receivers along the meridian of Eindhoven. The latitudinal range of the chain of receivers is determined by the sea. In the north, the meridian stands out to the North Sea from Harlingen. In Marseille, the meridian meets its southern barrier: the Mediterranean Sea. These towns form the natural ends of the array. The length of the array is thus set to 1105 kilometers, which guarantees sufficient angular coverage for a tomography experiment. The location of the array corresponds to our interest: the mid-latitude ionosphere. As follows from the geomagnetic coordinates in table 6.1, the array (and therefore the grid of reconstruction) is too far to the south to see much of the trough. On the other side, the grid is too far to the north to observe the equatorial anomaly.

It did not take long to find enthousiastic hosts for the receivers. They provided a flat roof with a clear view for the antenna and a sheltered room with power for the receiver and computer. In Harlingen, we were the guest of Noordzee College, School voor de Rijn-, binnen- en kustvaart (School for Rine-, inland- and coastal navigation). The municipality of Saint-Mihiel in France hosted a receiver at the elementary school Groupe Scolaire de la Halle. The Théâtre Municipal in Bourg-en-Bresse held another set of equipment. The southernmost antenna was supported by the roof of the tallest building of the Université de Marseille in Luminy: le Faculté des Sciences. Under the roof, the food storage room for laboratory animals housed receiver and computer. Table 6.1 gives the coordinates of the antenna locations and figure 6.1 contains a map. The receivers were very well placed along a meridian: the largest longitudinal separation between two receivers is only 0.3°.

On the 9th of March 1995, the northernmost receiver was installed in Harlingen. Next, the expedition went southwards. Dates of installation were March 13 (Saint-Mihiel), March 15 (Bourg-en-Bresse) and March 17 (Marseille). After a weekend's rest in the Provence,

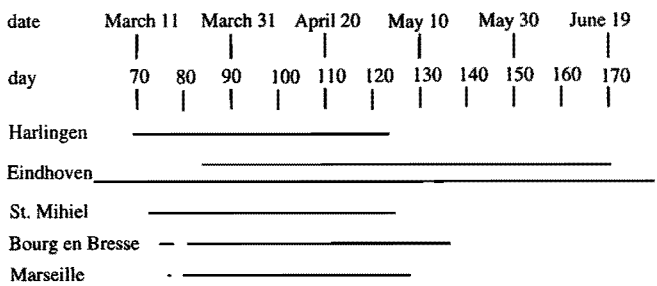

Figure 6.2: Overview of successful receiver operation, indicated by horizontal lines. Dates and day numbers in the year 1995.

we returned northwards and checked the receivers on our way back. We found that the equipment in Marseille and Bourg-en-Bresse had failed already. These were reset. On return in Eindhoven, the sixth receiver, the spare one, was installed as well. During the experiment, the hosts kept headquarters informed about the receivers' doings, but actual data were not transmitted. Towards the end of April, there was an inspection and data collection tour. All receivers were functioning well. After that tour, the receivers failed one after another, as can be seen in the schedule in figure 6.2. In the beginning of June, we took all receivers back to Eindhoven. The campaign counted a hundred days, among which 45 consecutive days of successful simultaneous operation. We are aware that the time of the year (spring) is not ideal for TID observation: wintertime is the season. It is unfortunate that the campaign could not be organized in winter.

6.2 Results

The 45 day interval of simultaneous receiver operation has yielded registration of roughly 1200 passes of six different NNSS satellites. The satellites were: NNSS-23, NNSS-25, NNSS-27, NNSS-31, NNSS-32 and NNSS-49. Of course, some satellite passes were missed by one receiver and others were missed by another. This reduces the number of passes suitable for tomographic reconstruction. To minimize problems with ray bending and ill-definition of the surface of reconstruction, we discarded all satellite passes with an elevation less than 30^o. Of course, this limit is somewhat arbitrary. The selection leaves us with 539 passes, which is an average of twelve per day. Most of these satellite passes were recorded by four or five receivers, but an occasional reconstruction is based on data recorded by only three receivers.

The 539 images of electron density were reconstructed by the algorithm described in chapters 4 and 5. The grid of reconstruction contains 2000 pixels: 100 pixels of 0.2^o in the latitudinal direction, and 20 pixels of 30 km height in the vertical direction. The grid covers an area between 38^o and 58^o latitude and between 100 km to 700 km altitude. In geomagnetic coordinates, the grid extends from 40^o to 59^o latitude. Figure 6.3 gives an example of a reconstruction, of which there are 538 more available for inspection.

In the following five subsections, we summarize the results. Section 6.2.1 compares the results from tomography against independent measurements of $N_{e,\max}$. In section 6.2.2, we

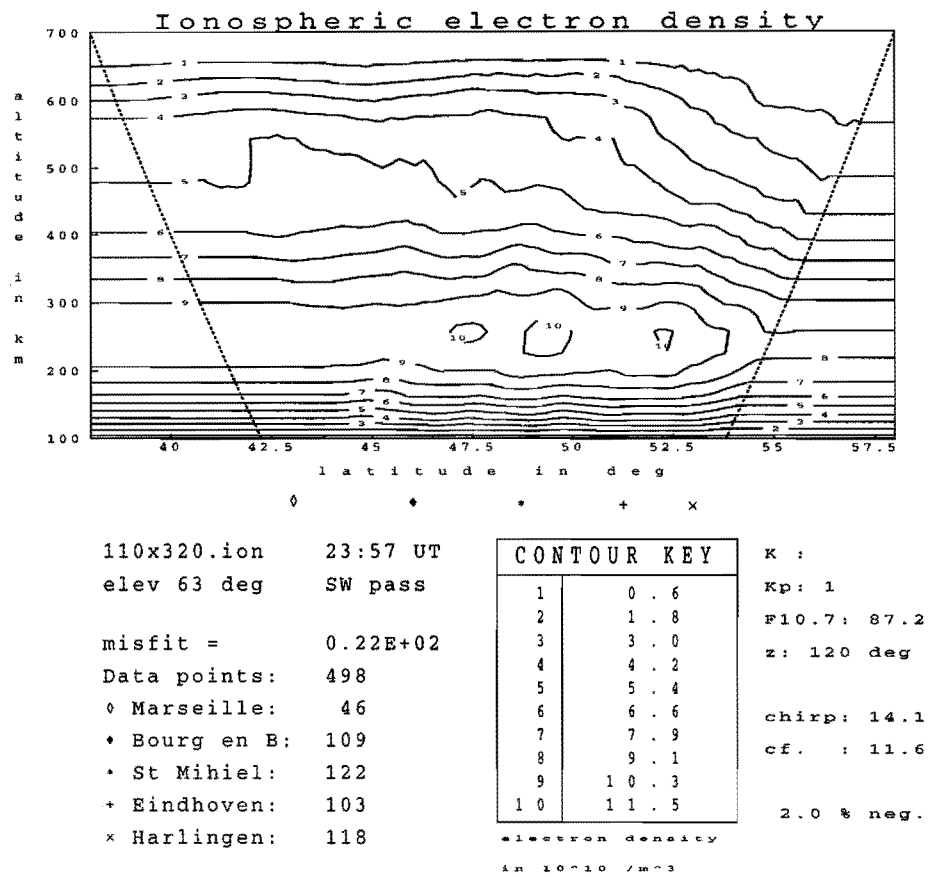

Figure 6.3: An example of a reconstruction. The file name 110x320.ion is unique and contains the day number (110, i.e. April 20), the satellite number (32) and the hour of the day (x, i.e. the 24^{th} hour). The satellite had a maximum elevation of 63° above the western horizon and moved southwards. Receiver location is indicated by the symbols at ground level. The interrupted diagonal lines represent the outermost lines of sight. Beyond these, the reconstruction forms a stratified continuation. The number of data points per receiver is indicated. The contours connect points of identical electron density and the contour scale is given by the contour key. At the right of the figure, entries give the planetary magnetic index (K_p), solar 10.7 cm flux ($F_{10.7}$) and solar zenith angle (z). Then follows the density (in 10^4 per cc) as derived from chirpsounder data (chirp), which should be compared against the density reconstructed by tomography, given in the next entry (cf.). The percentage in the lower right bottom is a measure of the negativeness of the reconstruction, if the positivity constraints are not included.

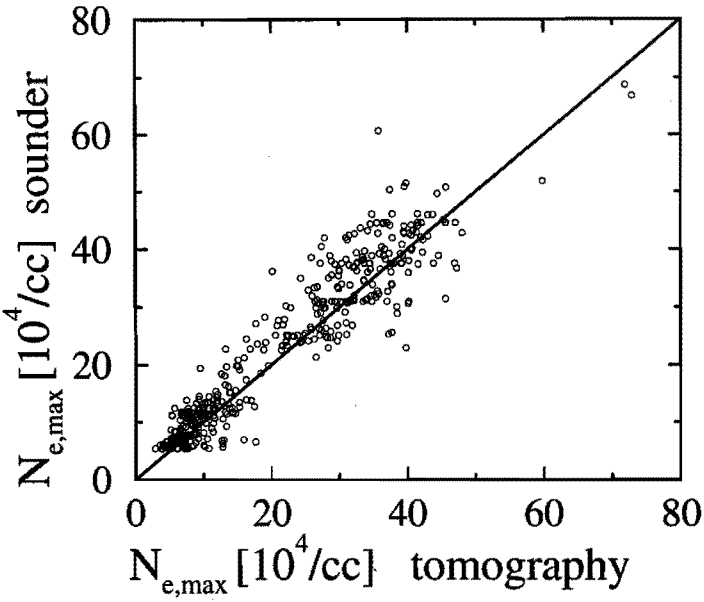

Figure 6.4: Comparison of the maximum electron density derived from the chirpsounder against the result from the tomographic reconstruction. The diagonal is drawn to ease interpretation. Tomography systematically underestimates the maximum electron density by 5% and the mean error is 18% (see text).

discuss the daily variation of $N_{e,\max}$ and $H_{\max}$. Next, we proceed with a summary of the results where the ionosphere significantly deviates from stratification. The trough is discussed in 6.2.3 and travelling ionospheric disturbances in section 6.2.5. Irregular (nighttime) ionospheres, which do not not fall in any existing category, are presented in section 6.2.4.

6.2.1 Comparison with chirpsounder

The Koninklijke Landmacht (the Royal Netherlands Army) provides hourly records of f_oF_2, based on chiprsounder measurements. Via equation (2.8), these data are readily converted to maximum electron density $N_{e,\max}$, which can be compared against the results from tomography. The chirpsounder transmitter and receiver are located in Havelte (52°.8 N, 6°.3 E) and Den Haag (52°.0 N, 4°.3 E), respectively. The middle of the transmission path lies at 52°.4 N and 5°.3 E, which is fairly well on the meridian of Eindhoven. When the chirpsounder can not determine f_oF_2 directly, maximum usable frequency (MUF) is used: f_oF_2 = MUF - 0.7 MHz. Because of the large inaccuracy, the chirpsounder records do not contain $H_{\max}$, the height of maximum electron density.

Generally, a satellite pass does not coincide with a sounding, that occurs 7 minutes after every hour. To allow comparison, the electron density as derived from the sounding is interpolated linearly over time. Because the soundings failed every now and then (systematically labelled 'atmospheric disturbance' by the operator), there are 409 points of comparison,

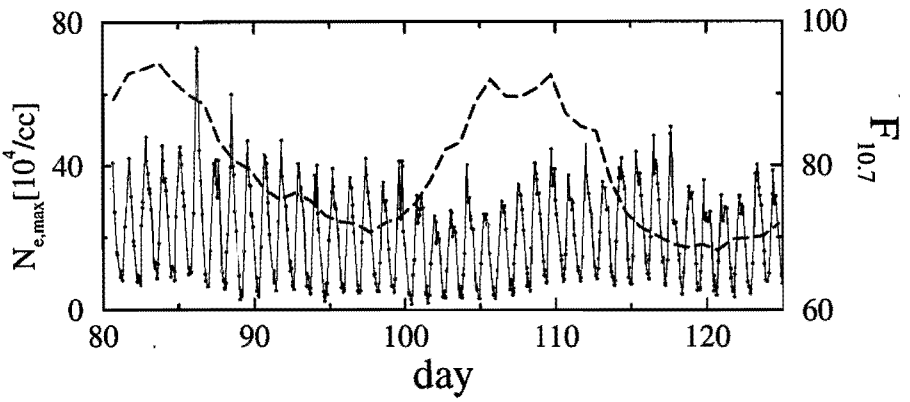

Figure 6.5: Maximum electron density versus time. The dashed line is the solar 10.7 cm flux in $10^{-22}\mathrm{Wm}^{-2}\mathrm{Hz}^{-1}$. The daily rhythm in $N_{e,\max}$ is clearly visible, but the graph also suggests an oscillation with a period of 25 days, that coincides with the variation in $F_{10.7}$. This is best visible in the nighttime $N_{e,\max}$, the lower envelope of the daily oscillation.

instead of 539. These points are marked in figure 6.4, where the electron density derived from the soundings is plotted against the maximum of the density profile at the middle of the transmission path, as computed in the tomographic reconstruction. If there were perfect accordance, all points in the figure would lie on the diagonal (drawn). The figure shows that there is a strong agreement between the two records. Still, the majority of the points lies above the diagonal, which means that the soundings systematically indicate a higher density than tomography. This agrees with the test results, that showed that the tomographic reconstructions are generally too smooth and therefore underestimate the maximum electron density (section 4.4).

Division of the density from tomography by the density from the chirpsounder, gives a ratio. If there were no errors, all ratios would equal unity. The mean of the set of 409 computed ratios is 0.95, which reflects a systematic underestimation by 5%.. Let the error be defined as the absolute value of the difference between this ratio and unity. With this definition, the mean error is 18%. This error cannot be explained solely by the inaccuracies in the interpolation over time.

We also compared our data with records from the ionosonde in Juliusruh (54°.6 N, 13°.3 E) on the German island Rügen, near the Polish border. The resulting graph is very similar to figure 6.4, and the statistics give the same result too. Intercomparison of the soundings (chirpsounder vs. the ionosonde in Rügen) gives the same statistics as well, although the systematic difference disappears (as it should). It is hard to tell from this ménage à trois which method is the source of error. Surely, they are not all due to tomography.

6.2.2 The daily patterns

When turning over the pages with reconstructions, several daily patterns emerge. Most obvious is the variation in electron density ($N_{e,\max}$), followed by the varying height of the layer of maximum electron density ($H_{\max}$).

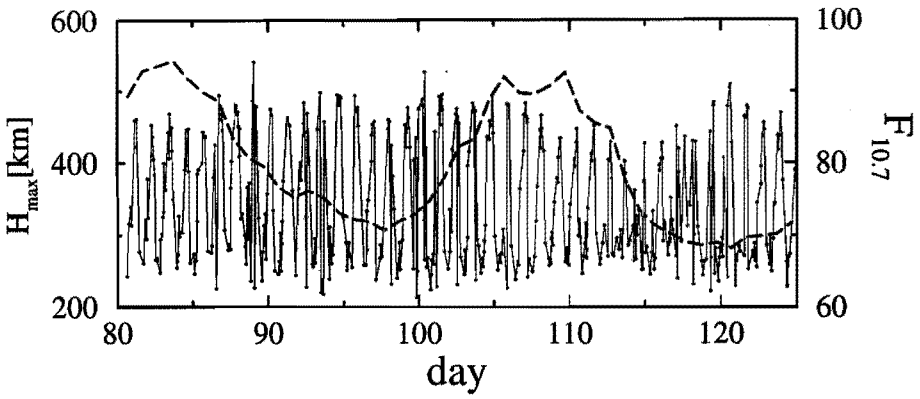

Figure 6.6: Height of the layer of maximum electron density versus time. The daily rhythm in $H_{\max}$ is evident, although it is not as clear as the oscillation in $N_{e,\max}$.

The daily variation in electron density (from the tomographic reconstruction) is given in figure 6.5. Day number is along the horizontal axis and plotted along the vertical axis is $N_{e,\max}$. The figure clearly shows a daily pattern, with high densities during the day and low densities during the night. The figure also suggests an oscillation with a period of about 25 days. This oscillation is most clearly visible in the nighttime electron density, or the lower envelope of the daily oscillation. This envelope hints at maxima around night 84/85 and night 109/110, separated by 25 nights. Solar rotation has a period of $\sim$ 25 days as well. The superimposed dashed curve shows that this is no coincidence. It gives solar radio flux at 10.7 cm, which is a measure of solar activity and UV flux. The figure shows that the 10.7 cm flux peaks at the same time as the nighttime electron density (the lower envelope).

The daily pattern in $N_{e,\max}$ is summarized in figure 6.7. Here we see $N_{e,max}$ as a function of solar zenith angle. Filled circles represent morning (am) passes and open squares represent afternoon (pm) passes. The diurnal variation is clearly visible. A kind of hysteresis loop can be seen as well: for solar zenith angles in the range $80^o < \chi < 110^o$, evening density is higher than morning density. This effect can be interpreted in terms of long dissociative recombination time scales (section 1.3). Recombination takes its time to unite ions and electrons once the sun has ionized the tenuous atmospheric gases. As a result, high electron density can persist while the sun sets.

Even more interesting than the daily variation in $N_{e,\max}$ is the pattern in $H_{\max}$. Figure 6.6 gives the height of the layer of maximum electron density as a function of time. Again we see a diurnal variation, although the pattern is not as clear as the oscillation in figure 6.5. In figure 6.8 this daily pattern is summarized. It follows that $H_{\max}$ increases with χ during the day. During the night, $H_{\max}$ is higher than during the day; in daytime, $200 < H_{\max} < 300$ km, and at night $400 < H_{\max} < 550$ km. This is consistent with Chapman theory. Moreover, the high nocturnal altitudes agree with the general notion that (dissociative) recombination rates decrease with altitude as a result of decreasing (neutral) density (section 1.3). Because recombination is slow at high altitudes, $H_{\max}$ shifts effectively upwards when ionization has ceased and electron density is controlled by recombination. Another factor might be the

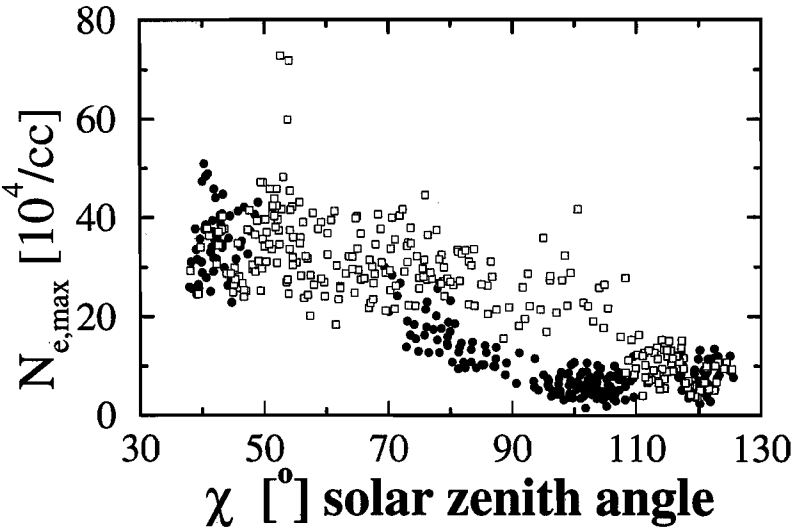

Figure 6.7: Maximum electron density versus solar zenith angle. $N_{e,\max}$ decreases with increasing χ. Solid circles represent morning passes and open squares represent afternoon passes. At 400 km altitude, the horizon has zenith angle $\sim 110^o$. Therefore, when $\chi > 110^o$, night reigns the ionosphere. Note the morning-evening hysteresis loop, where the am and pm points each occupy a different zone for $80^o < \chi < 110^o$.

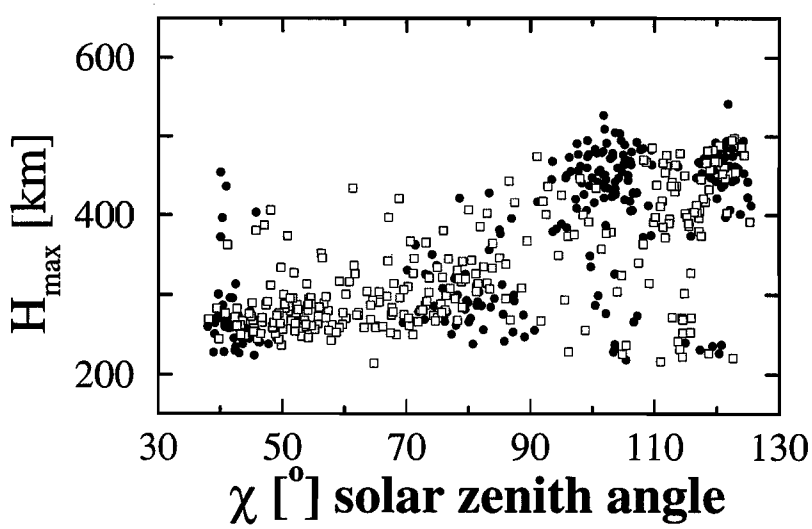

Figure 6.8: Height of maximum electron density versus solar zenith angle. $H_{\max}$ increases with χ and remains high during the night.

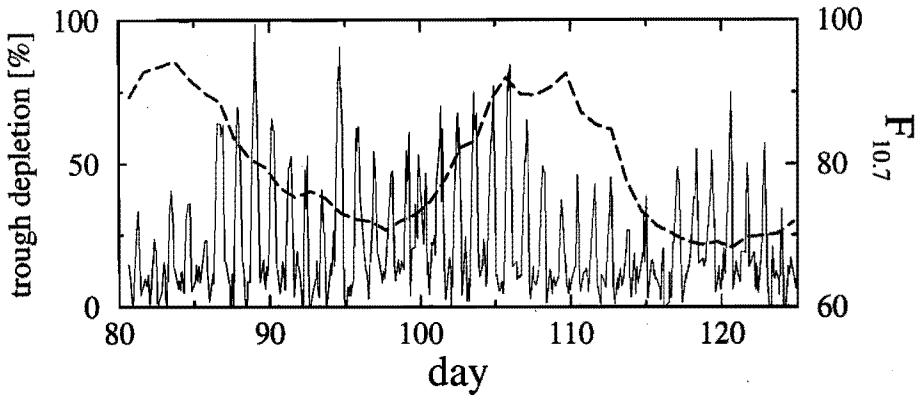

Figure 6.9: Trough depletion versus time. The daily pattern is clearly visible. Solar 10.7 cm flux is superimposed. The graph suggests an anticorrelation between nighttime trough depletion and $F_{10.7}$.

downward transport of plasma from the plasmasphere.

The nice thing is, that the tomographic method is indeed capable of seeing the variation in $H_{\max}$. We have anticipated in chapter 4, that it is difficult to estimate $H_{\max}$ by tomography. This could explain the relatively large scatter in figures 6.6 and 6.8. Moreover, it is difficult to determine $H_{\max}$ by any other method. For example, the chirpsounder and ionosonde records, which we compared against our $N_{e,\max}$, do not contain $H_{\max}$. And indeed, records like ours on the daily variation in $H_{\max}$ are scarce in the literature.

6.2.3 The trough

In high-latitude experiments of ionospheric tomography, the trough (section 1.3.2) is a recurring phenomenon (Pryse et al 1993, Kunitsyn et al 1995, Mitchell et al 1995). Images of the trough constitute one of the main successes of the method. Our mid-latitude experiment is too far too the south to really see the trough. However, there are nights that we can see its southern flank. In figures 6.11 and 6.12, we see the behaviour of the southern flank of the trough during night 92/93 (April 2/3, 1995).

An objective measure of this manifestation of the trough is the relative depletion of electron density at the northern end of the grid of reconstruction as compared to the mean electron density in the middle part of the grid. Figure 6.9 gives this relative trough depletion as a function of time. It follows that there is a strong diurnal variation, where trough depletion is strongest during the night. There might be be a weak anticorrelation between trough depletion and solar 10.7 cm flux. Trough depletion seems to be strongest when $F_{10.7}$ (background line) is low. The data give no indication of a correlation between trough depletion and the planetary magnetic activity index K_p.

6.2.4 The disturbed ionosphere

Although the unperturbed mid-latitude ionosphere exhibits clear and interesting daily

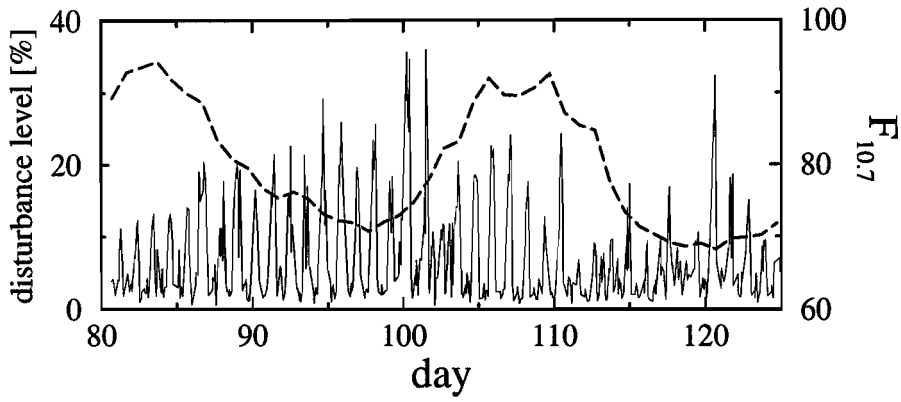

Figure 6.10: Disturbance level versus time. The daily pattern is clearly visible. Solar 10.7 cm flux is superimposed. The graph hints at an anticorrelation between (nocturnal) disturbance and $F_{10.7}$.

variations, nothing bores more than endless series of pictures of the regular and stratified ionosphere. Here, irregularities are welcome distractions. Moreover, this research was initiated out of curiosity about ionospheric disturbances, and especially about the travelling ionospheric disturbance or TID. The section will conclude with images of these disturbances, but we start with a few words.

An objective measure of the degree to which the ionosphere is spatially disturbed, is the relative residue that remains after a smooth fit is subtracted from the reconstructed ionosphere. This measure, the relative disturbance, is plotted versus time in figure 6.10. Again there is a clear diurnal variation, where disturbances are relatively frequent and strong during the night. And again, there could be a weak anticorrelation with solar $F_{10.7}$, as we saw for trough depletion. There seems to be no correlation with K_p. Figures 6.11 through 6.16 contain series of reconstructions of three such disturbed nights. In figure 6.14, a steep depletion seems to move equatorward by roughly 1°/hour, while the regular trough seems to be stationary at the northern side of the field.

It is clear from the study that the ionosphere is more disturbed and less stratified in the night than during the day. It would seem that recombination rate (that dictates the nighttime electron distribution) varies more strongly with position than ionization (that stabilizes the situation during the day). It is not really possible to categorize the nighttime irregularities.

6.2.5 TIDs

A disturbed ionosphere is one thing, a travelling ionospheric disturbance is quite something else. Only when the disturbance has an ordered and quasiperiodic appearance, there is a clear and positive TID identification. In other words, we are looking for something like the idealized TID of figure 4.5. Visual inspection shows that in roughly a quarter of all days, more or less quasiperiodic structures appear, such as in figure 6.3. Usually, these are daytime manifestations. The quasiperiodic structure in these reconstructions is weak. Sometimes it depends on the contour scaling whether the structure can be seen or not. Figures 6.17 through

6.19, contain three series of reconstructions where the quasiperiodic structure is visible at time intervals. The enhancements are tilted southward at the top, which is consistent with equatorward propagation. Unfortunately, the identification of features in successive frames to derive propagation speed is ambiguous. The TID wavelength, as projected on the meridional plane of reconstruction, varies from 190 to 290 km. The oscillations can therefore be associated with medium scale TIDs. Two remarks on the paucity of TID observations are in order. First, visual inspection of raw TEC data sometimes suggested oscillation at latitudes beyond the grid of reconstruction (both in the north and the south). These were not further considered. Second, the campaign was in spring, not the TID season, which is winter (Leitinger, private communication).

In the literature, there are two more examples of dynamic TID behaviour imaged by tomography: Cook et al (1995) present one pair of reconstructions over Mid-America, 46 minutes apart, with quasiperiodic structure and latitudinal wavelength of 640 km. Pryse et al (1995) present two pairs of images over Britain, (44 and 56 minutes apart) and latitudinal wavelength of 220 km. In the three cases, the enhancements are tilted up- and equatorward, indicative of motion towards the equator. The authors point at features in the successive images that are supposed to have moved. In my opinion, the identifications are ambiguous. Pryse et al (1995) suggest that the TIDs they see are caused by a strong flow in the jet stream north of the UK, as shown in 300 mbar weather charts. The authors do not explain how this flow, that presumably streams towards the east, could possibly generate southward propagating disturbances with much larger phase speed. Whatever the mechanism might be, we did not find a correlation between TID occurrence and 300 mbar weather patterns (Deutsche Wetterdients charts, kindly provided by van Velthoven) over the period of our campaign.

We have checked the TID identifications in our data against presence of quasiperiodic oscillations in the Westerbork interferometer calibration measurements. Every now and then, the radio telescopes observe a strong astronomical pointsource to calibrate the instrument. These measurements contain information on changes in the optical path length, that are partially due to the ionosphere. Therefore, TIDs are visible as oscillations. As Westerbork (52°.9 N, 6°.6 E) is quite near the Eindhoven meridian, we have looked for simultaneous TID registrations. This effort is comparable to Spoelstra's 1992 study.

At 92 cm wavelength, there were 24 Westerbork calibration measurements longer than 30 minutes in the period between March 21 and April 3. Between the 5^{th} and 26^{th} of April, there were 12 such calibration measurements at 49 cm wavelength (Spoelstra, private communication). Unfortunately, we found no coincident TID registrations. Several facts could explain this absence.

1. Suitable Westerbork calibration measurements in the period of the tomography campaign are scarce and few coincide with satellite passes. In his 1992 paper, Spoelstra compares satellite pass registrations and Westerbork calibration measurements that are more than 2 hours apart.

2. The Westerbork array extends over 3 km in the east-west direction. It is only sensitive to gradients in TEC over that baseline. By contrast, TEC records from NNSS observation see north-south gradients over much longer distances.

3. In the Westerbork data, the effects of ionospheric oscillations with periods $\gtrsim$ 12 minutes

dominate. An oscillation with so short a period cannot be seen in a tomographic reconstruction (section 4.1.3).

We have made some remarks about possible correlations of TIDs and other phenomena from the tomography campaign with independent records (anticorrelation with $F_{10.7}$, no correlation with Westerbork, nor with K_p and 300 mbar weather patterns). Of course, the goal of such climatological study is to find possible excitation mechanisms for TIDs and other ionospheric phenomena. For this purpose, however, the 45 day period of observations is very short, and statistical evidence is poor. A sound statistical analysis would require a campaign carried out over a period preferably longer than a year.

Yet, for a climatological study of TIDs, single station differential Doppler registrations are equally good as tomography from multiple stations, because an image of a TID is not needed for its identification. Such a TEC database, based on many years of NNSS satellite observation, exists in Graz, Austria (Leitinger, private communication). A study on TID climatology and correlation with possible TID excitation mechanisms based on these data could be very fruitful. Comparison with the 22 years Westerbork TID climatology (Spoelstra, 1996) could answer the question if both methods observe the same ionospheric phenomena.

6.3 Conclusions

From 539 tomographic reconstructions of the ionosphere based on data collected over a 45 day campaign mounted in spring 1995 over the Netherlands and France, we conclude the following:

1. Comparison of $N_{e,\max}$ from tomography with chirpsounder records shows a mean disagreement of 18% between the methods, that is not all due to tomography. It further shows that the tomography $N_{e,\max}$ findings are systematically 5% lower than the chirpsounder's.

2. The tomography campaign reveals a clear diurnal pattern in $N_{e,\max}$. It also suggests a weak 25 day oscillation. The 25 day oscillation coincides with solar 10.7 cm flux ($F_{10.7}$) and reflects solar rotation.

3. The tomography campaign shows a diurnal pattern in $H_{\max}$. During the day, $H_{\max}$ is low, $200 < H_{\max} < 300$ km, and increases with solar zenith angle. At night, it is high, $400 < H_{\max} < 550$ km. This is consistent with Chapman theory and with the general notion that recombination rates decrease with altitude.

4. In many nights, a depletion of electron density in the northern part of the reconstruction forms, indicative of the trough. In some nights, the through's southern flank can be seen as a steep gradient in electron density. There is no correlation of trough depletion with K_p, but there might be an anticorrelation with $F_{10.7}$.

5. During the night, the ionosphere is much more disturbed and less stratified than during the day. This could be explained in terms of strong local variations in dissociative recombination rate. These disturbances are not really quasiperiodic and are hard to classify. The disturbance level does not correlate with K_p, it might anticorrelate with $F_{10.7}$.

6. In the results from the tomography campaign, TID identifications are weak and scarce. Most of them occur during the day and they are medium scale. They are tilted equatorward at the top. Unambiguous identification of features in successive reconstructions is impossible. The quasiperiodic oscillations do not correlate with K_p, $F_{10.7}$, oscillations in Westerbork calibration measurements nor with 300 mbar weather patterns.

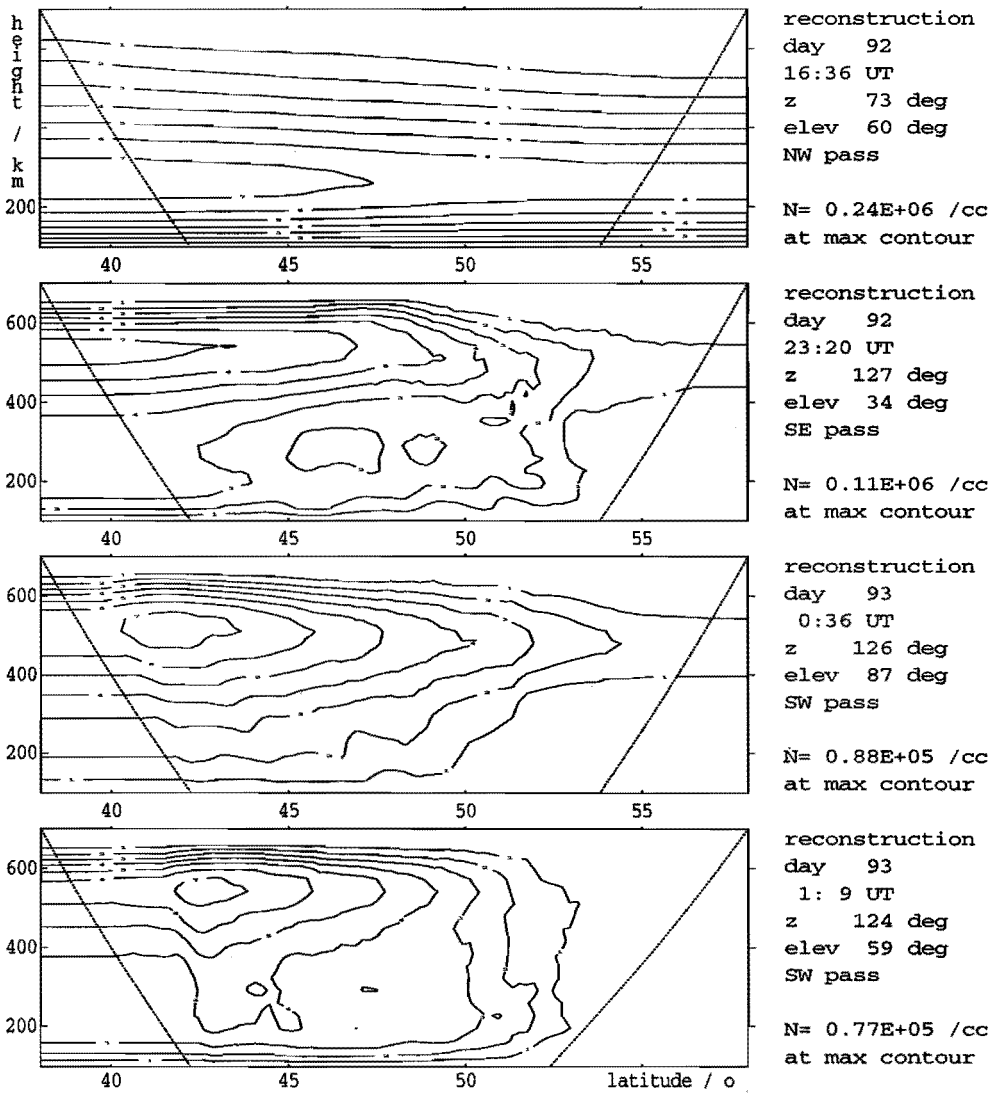

Figure 6.11: Disturbed night 2/3 April, 1996. The series begins at 16:36 UT with a quiet and stratified ionosphere, $H_{\max} = 275$ km, typical daytime height. Then, trouble starts and the trough comes in. The southern flank of the severely depleted trough is clearly visible. In the fourth frame, the trough is at its deepest (depletion 91%) and at its southernmost point. Continues ..

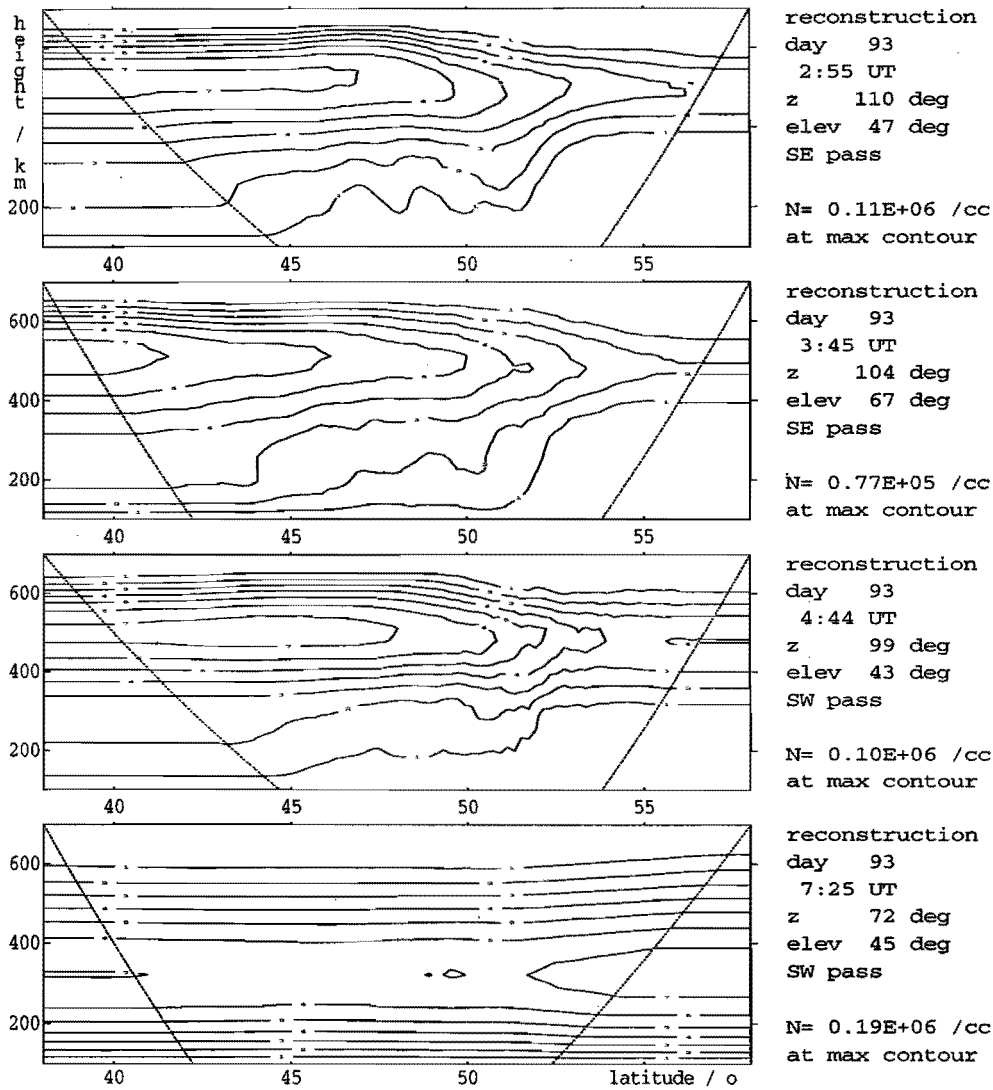

Figure 6.12: .. continued. Strange enough, magnetic conditions were quiet, $K_p = o^+$. In the last frame, rest has returned with the morning.

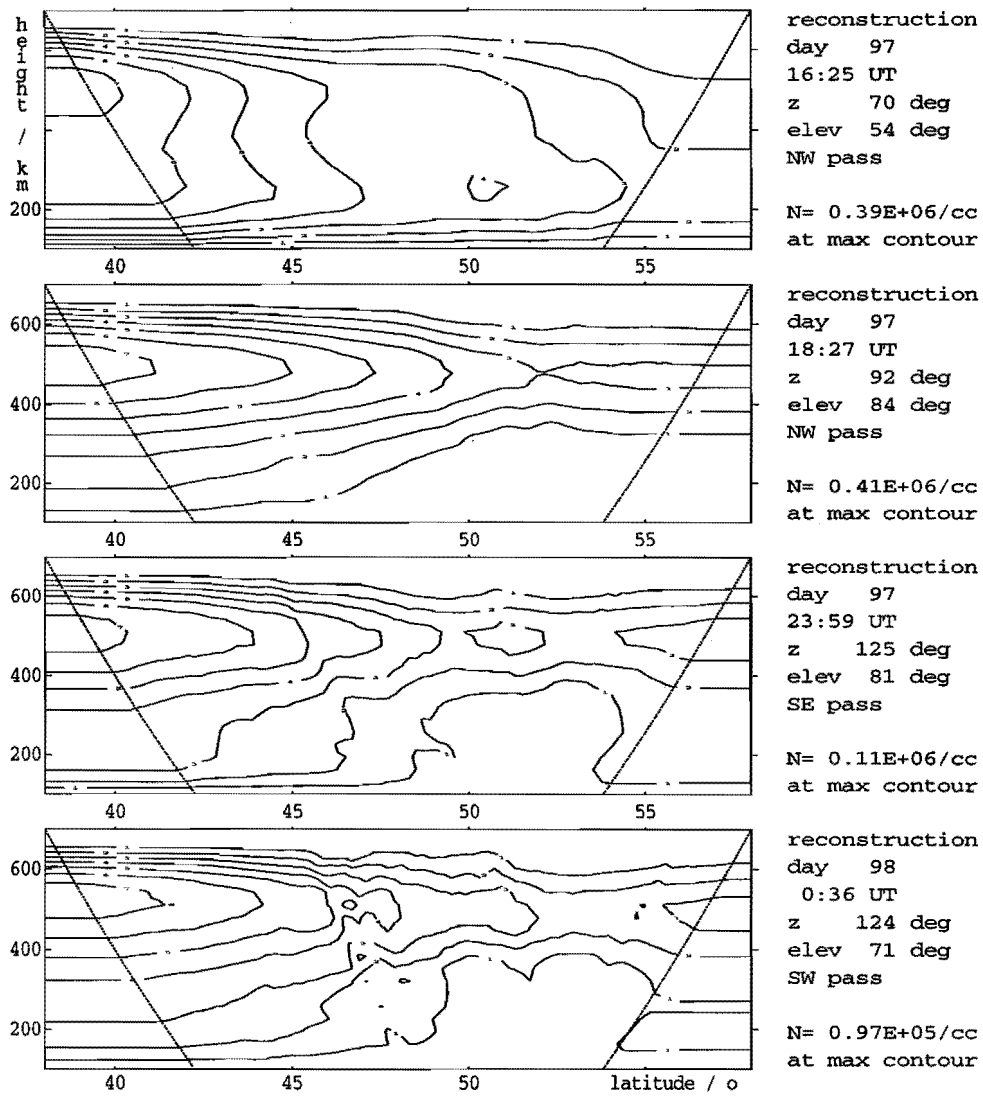

Figure 6.13: Disturbed night 7/8 April, 1996. A trough seems to be present in the third and fourth frame. Continues ..

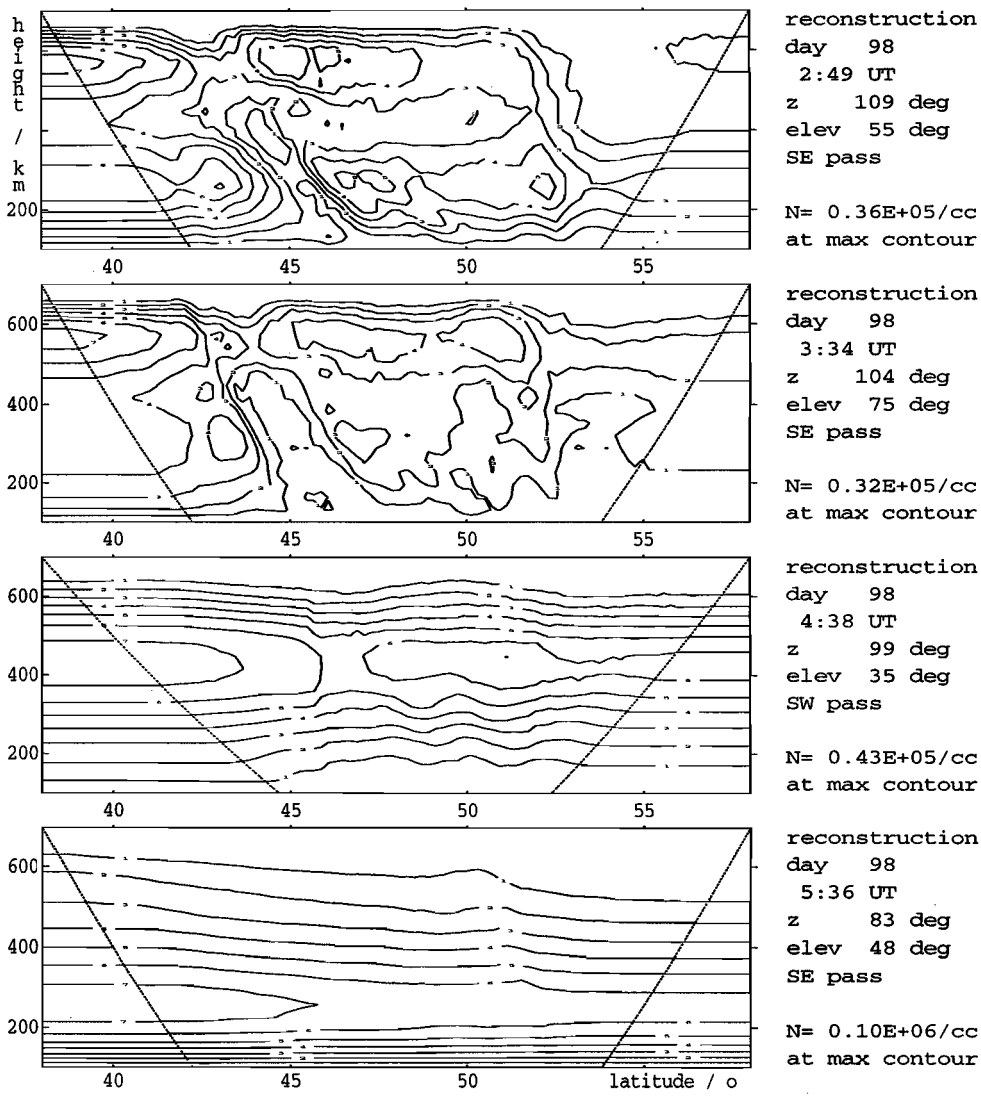

Figure 6.14: .. continued. In the top frame, a peculiar depletion seems to have formed at $\sim 45^o$ N. This depletion appears to move southward by roughly 1^o/hour, while the main depletion (trough) seems to be stationary at the northern end of the field of view. In the morning, everything is quiet.

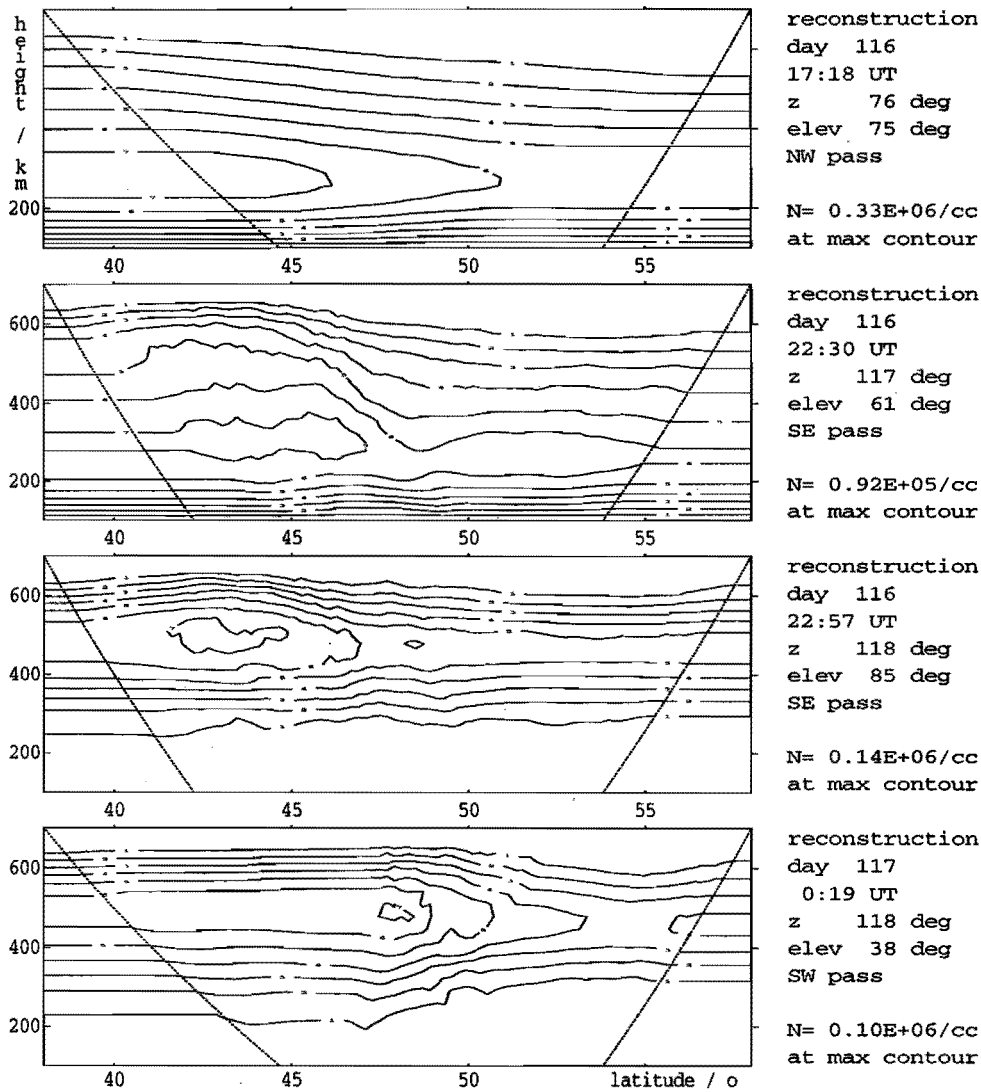

Figure 6.15: Disturbed night 26/27 April, 1996. This series is typical of a disturbed night. The series begins with a quiet afternoon ionosphere. After sunset, density drops and $H_{\max}$ rises. A slight troughlike depletion forms. Continues ..

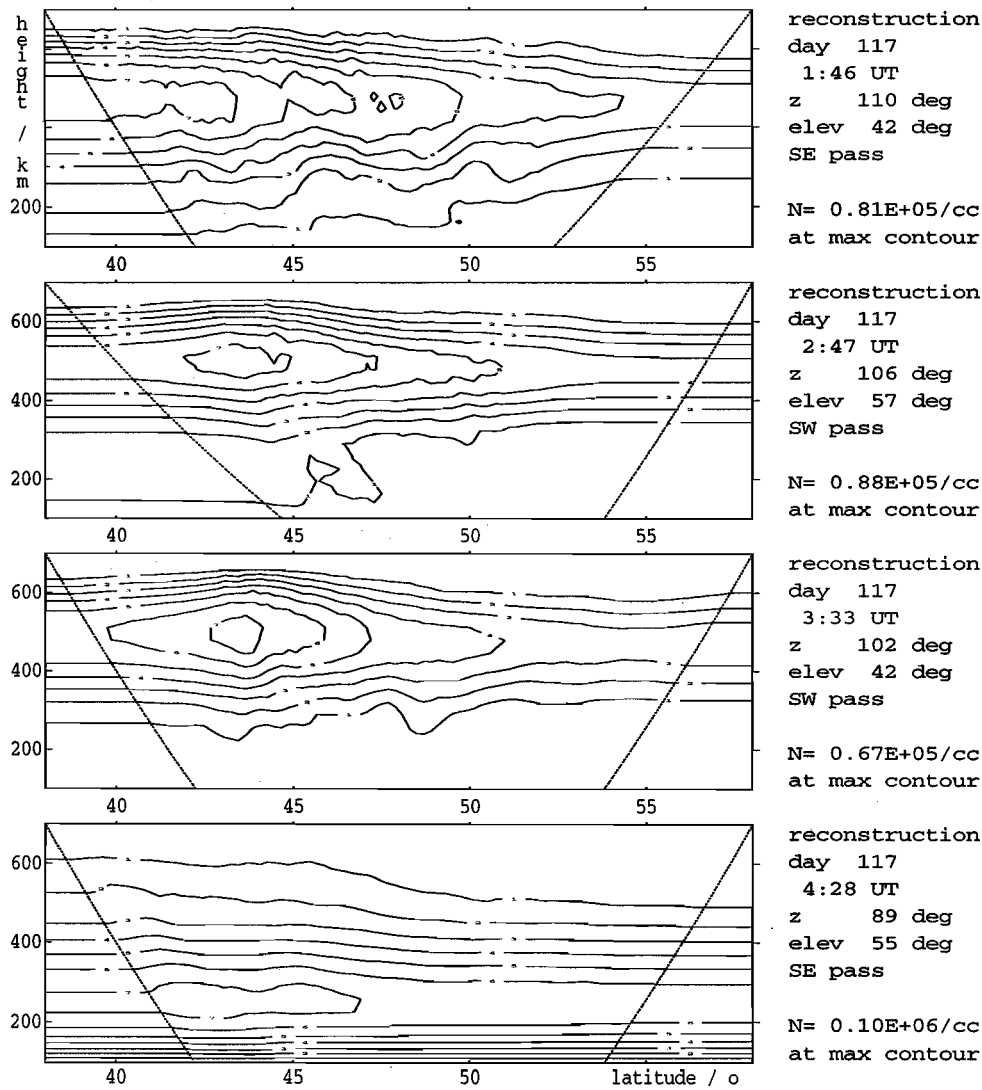

Figure 6.16: .. continued. Some periodic structure seems to be present in the top frame. In the morning, the ionosphere fills and settles at daytime altitude.

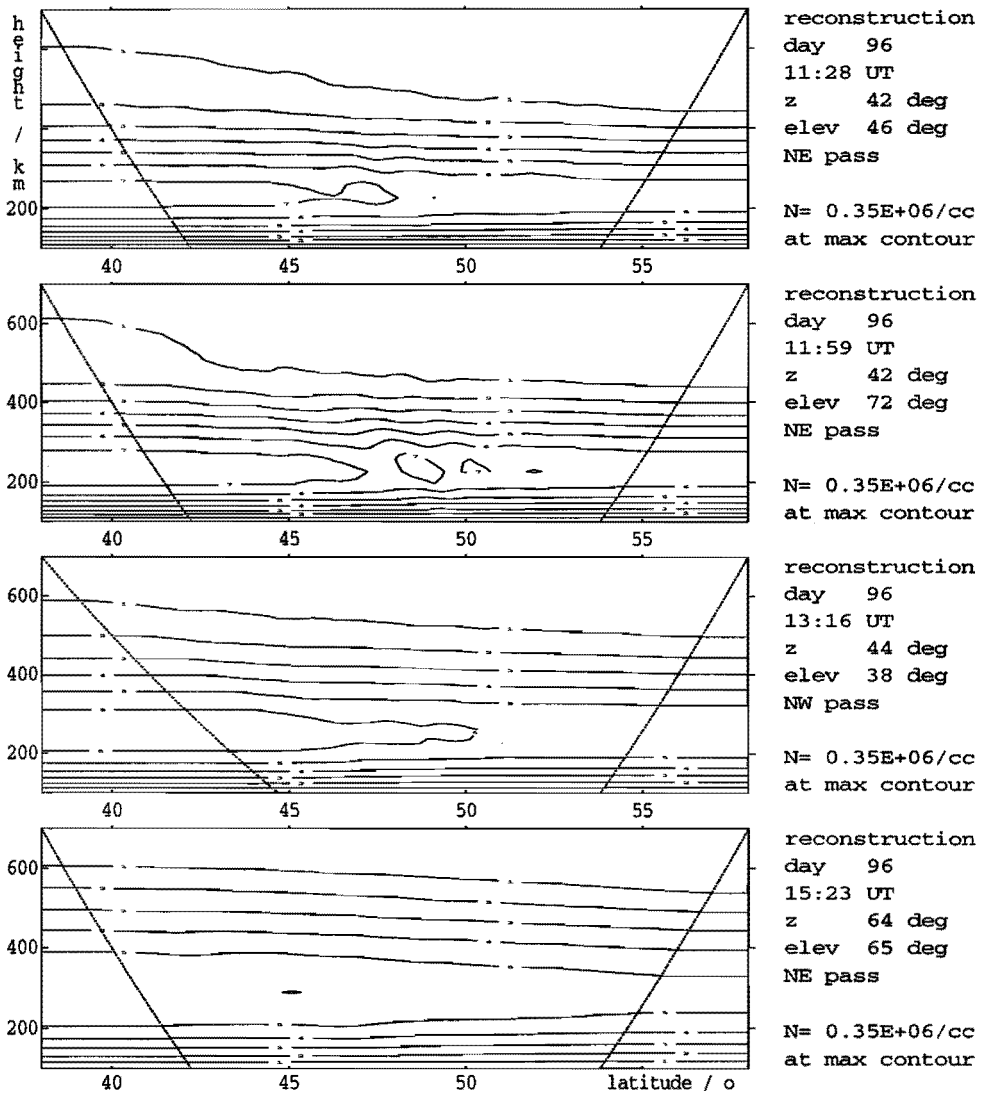

Figure 6.17: Quasiperiodic daytime structure on April 6, 1995. Projected wavelength $\sim 1^{o}.6$, or ~ 190 km.

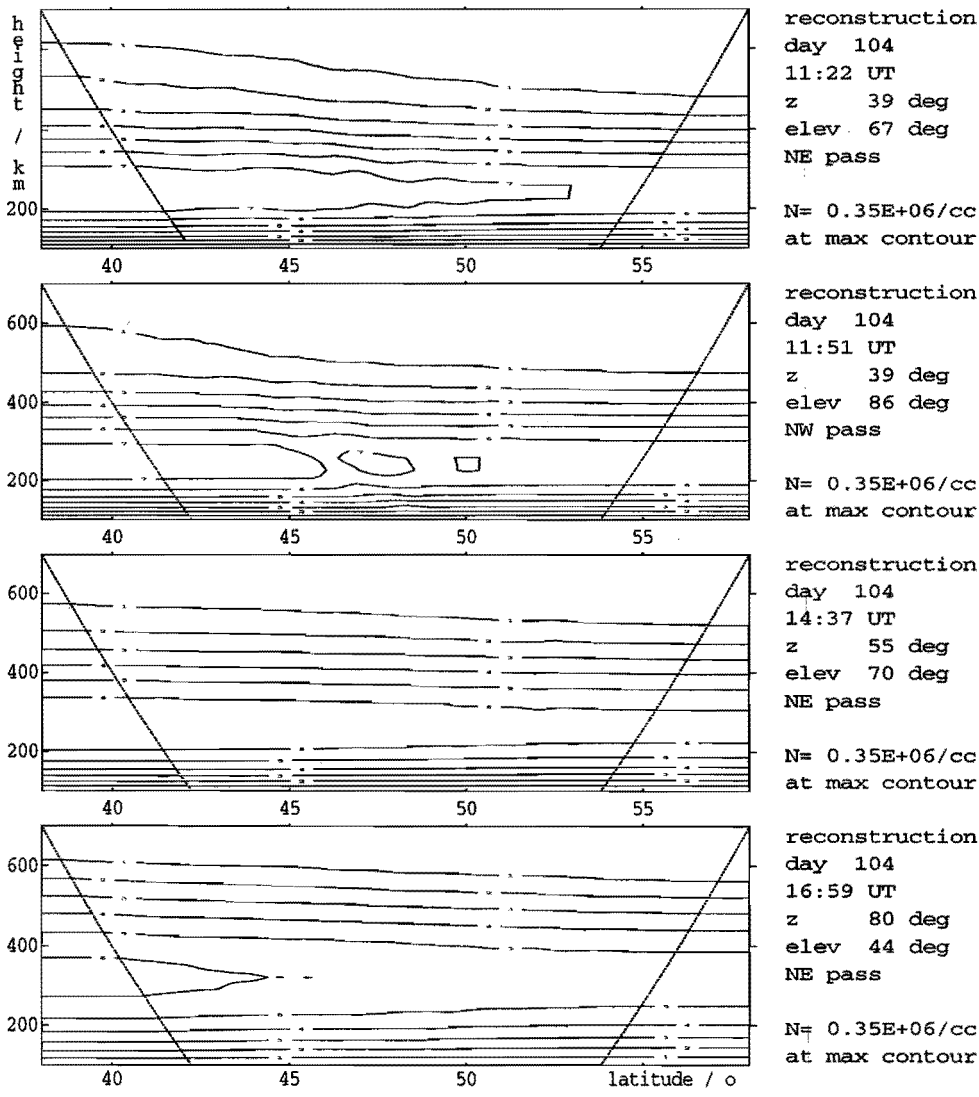

Figure 6.18: Quasiperiodic daytime structure on April 14, 1995. Projected wavelength $\sim 2^{\circ}.5$, or ~ 290 km.

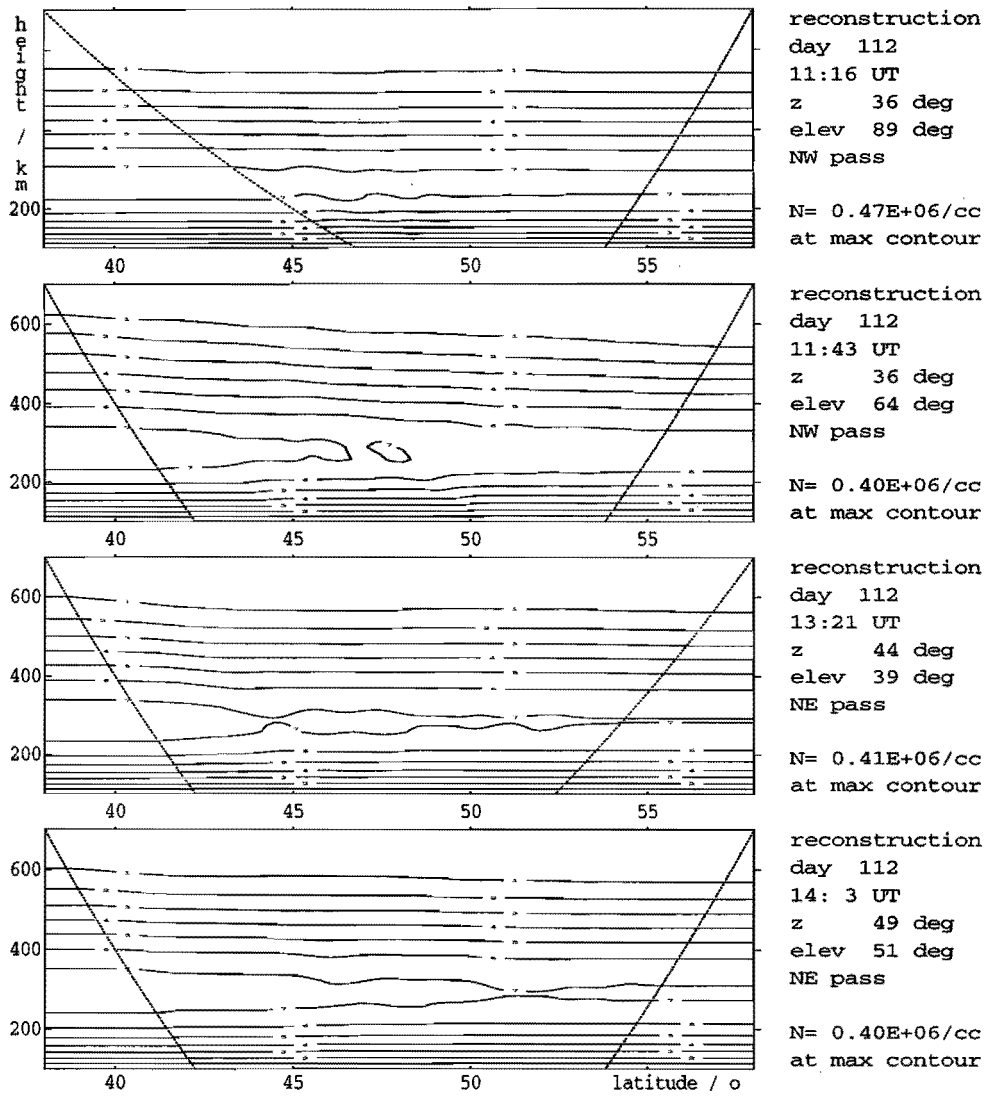

Figure 6.19: Quasiperiodic daytime structure on April 22, 1995. Projected wavelength $\sim 1°.8$, or ~ 210 km.

Chapter 7

Conclusion

Differential Doppler measurements of beacon satellite signals by an array of receivers on earth can be used to reconstruct cross-sections of ionospheric electron density. These images can give a rough picture of the ionosphere's state and structure, but they are certainly not accurate, detailed and reliable reproductions. The uncertainties in the reconstructions relate much more to the vertical structure than to the horizontal structure. This results from the fact that the measurement geometry does not provide (near-)horizontal lines of sight (or dito line integrals). These would contain the information on the ionosphere's vertical profile. As that piece of information is virtually missing, the reconstruction cannot be expected to render the vertical structure.

Most reconstruction algorithms compensate for the missing information by the use of model ionospheres as a priori information. Essentially, these algorithms preset a vertical profile. It is no surprise that these algorithms produce reconstructions with predictable vertical profiles. This is not a very sound basis if we are going to use the reconstructions to improve our knwoledge of the ionosphere and develop better models. This thesis presents an algorithm that depends only very weakly on model information. The a priori knowledge is based on the following pieces of information: the ionosphere is basically smooth and stratified, electron density at the top and at the bottom of the ionosphere is low, and electron density cannot be negative. Tests demonstrate that this information is sufficient to compute reasonably reliable reconstructions. The horizontal structure is retrieved well and the vertical structure is recovered with moderate success. The height of the layer of maximum electron density, for example, is estimated to within an accuracy of 90 km.

An experiment with five receivers placed along a 1100 km long baseline in western Europe, indeed demonstrates both the feasibility and the weakness of the method. The campaign resulted in 539 reconstructions over 45 consecutive days in the spring of 1995. There is a fairly large agreement between the maximum electron density in these reconstructions and independent chirpsounder measurements. The mean difference is 18% and there is a systematic difference of 5%. The systematic difference can be explained by the imposed smoothness of the tomographic reconstruction, thereby underestimating the peak density.

The reconstructions show a clear daily pattern in electron density, that is high during the day and low during the night. More interesting is a daily variation in the height of the layer of maximum electron density: low during the day and high at night. This pattern is not as clear-cut as the pattern in electron density, but it undeniably exists, thereby proving the claim that the method can estimate the height of a layer. The height variation is consistent

with Chapman theory and with the notion of decreasing (dissociative) recombination speed with increasing altitude.

Other results of the campaign pertain to the irregular ionosphere and show trough depletion, weak TID manifestations and strong nighttime irregularities that cannot be categorized. A thorough analysis of these irregularities, their climatology and their correlation with other phenomena will need a campaign carried out over a period preferably longer than a year.

In the future, the uncertainties in the vertical structure could be removed by launching low orbiting satellites equipped with differential Doppler (or GPS) receivers. These would provide the horizontal line integrals that contain the information on the vertical profile. Only then, will tomography become a reliable tool for ionospheric imaging.

References

Afraimovich E.L., O.M. Pirog and A.I. Terekhov, 1992, 'Diagnostics of large-scale structures of the high-latitude ionosphere based on tomographic treatment of navigation-satellite signals and of data from ionospheric stations', Journal of Atmospheric and Terrestrial Physics **54**, 1265-1273

Andreeva E.S., A.V. Galinov, V.E. Kunitsyn, Yu.A. Mel'nichenko, E.D. Tereshchenko, M.A. Filimonov and S.M. Chernyakov, 1990, 'Radiotomographic reconstruction of ionization dip in the plasma near the earth', JETP Letters **52**, 145-148

Arfken G.B. and H.J. Weber, 1995, 'Mathematical methods for physicists', Academic Press, London

Austen J.R., S.J. Franke, C.H. Liu and K.C. Yeh, 1986, 'Application of computerized tomography techniques to ionospheric research', International Beacon Satellite Symposium June 9-14 1986, Oulu Finland, Proceedings part 1, 25-36

Austen J.R., S.J. Franke and C.H. Liu, 1988, 'Ionospheric imaging using computerized tomography', Radio Science **23**, 299-307

Austen J.R., T.D. Raymund, C.H. Liu, S.J. Franke, J.A. Klobuchar and J. Stalker, 1990, 'Computerized ionospheric tomography', Ionospheric Effects Symposium, June 1-3 1990

Bertero M., C. De Mol and G.A. Viano, 1980 'The stability of inverse problems', in *Inverse Scattering Problems*, ed. H.P. Baltes, Springer-Verlag, Berlin

Bertero M., C. De Mol and E.R. Pike, 1988 'Linear inverse problems with discrete data: II. Stability and regularization', Inverse Problems **4**, 573-594

Budden K.G., 1985, 'The propagation of radio waves', Cambridge University Press

Censor Y., 1981, 'Row-action methods for huge and sparse systems and their applications', Siam Review **23**, 444-466

Censor Y., P.P.B. Eggermont and D. Gordon, 1983, 'Strong underrelaxation in Kaczmarz's method for inconsistent systems', Numerische Mathematik **41**, 83-92

Censor Y., 1983, 'Finite series-expansion reconstruction methods', Proceedings of the IEEE **71**, 409-419

Cook J.A., S. Close, 1995, 'An investigation of TID evolution in MACE '93 data', Annales Geophysicae **13**, 1320-1324

Crane R.P., 1976, 'Refraction effects in the neutral atmosphere', in *Methods of experimental physics*, vol **12B**: Radio Telescopes, ed. M.L. Meekes, Academic Press, New York

Daly P., 1984, 'Cosmos revisited: the USSR VHF satellite navigation system', Space Communication and Broadcasting, bf 2, 129-142

Davies K., 1990, 'Ionospheric radio', IEE Electromagnetic waves series **31**, Peter Peregrinus Ltd., London

Devaney A.J., 1984, 'Geophysical diffraction tomography', IEEE Transactions on Geoscience and Remote Sensing, **GE-22**, 3-13

Erickson W.C., 1984, 'Ionospheric refraction in radio source observations at long radio wavelengths', Journal of Astrophysics and Astronomy **5**, 55-65

Fischer L., 1974, 'Probability and statistics', in *Handbook of applied mathemathics*, ed. C.E. Pearson, Van Nostrand Reinhold, New York

Fremouw E.J. and J.A. Secan, 1992, 'Application of stochastic inverse theory to ionospheric tomography', Radio Science **27**, 721-732

Fremouw E.J., J.A. Secan, R.M. Bussey and B.M. Howe, 1994, 'A status report on applying discrete inverse theory to ionospheric tomography', International Journal of Imaging Systems and Technology **5**, 97-105

Fougere P.F., 1995, 'Ionospheric radio tomography using maximum entropy 1. Theory and simulation studies', Radio Science **30**, 429-444

Gantmacher F.R., 1959, 'The theory of matrices', Chelsea, New York

Garriot O.K. and A.W. Nichol, 1961, 'Ionospheric information deduced from the Doppler shifts of harmonic frequencies from earth satellites', Journal of Atmospheric and Terrestrial Physics **22**, 50-63

Garriot O.K., A.V. da Rosa and W.J. Ross, 1970, 'Electron content from Faraday rotation and phase path length variations', Journal of Atmospheric and Terrestrial Physics **32**, 705-727

Georges T.M., 1968, 'HF Doppler studies of travelling ionospheric disturbances', Journal of Atmospheric and Terrestrial Physics **30**, 735-746

Giraud A. and M. Petit, 1978, 'Ionospheric techniques and phenomena', D. Reidel Publishing Company, Dordrecht, Holland

Golub G.H. and C.F. Van Loan, 1989, 'Matrix Computations', 2nd edition, Johns Hopkins University Press, London

Gull S.F. and G.J. Daniell, 1978, 'Image reconstruction from incomplete and noisy data', Nature **272**, 686-690

Hansen P.C., T. Sekii and H. Shibahashi, 1992, 'The modified truncated SVD method for regularization in general form', SIAM Journal Sci. Stat. Comput. **13**, 1142-1150

Hargreaves J.K., 1979, 'The upper atmosphere and solar-terrestrial relations, an introduction to the aerospace environment', Van Nostrand Reinhold Company

Heaton J.A.T., S.E. Pryse and L. Kersley, 1995, 'Improved background representation, ionosonde input and independent verification in experimental ionospheric tomography', Annales Geophysicae **13**, 1297-1302

Ingesson L.C., 1995, 'Visible-light tomography of tokamak plasmas', PhD thesis, Technische Universiteit Eindhoven

Jaynes E.T., 1968, 'Prior probabilities', IEEE Transactions on System Science and Cybernetics, **SSC-4**, 227-241

Junginger H.-G. and W. van Haeringen, 1972, 'Calculation of three -dimensional refractive-index field use phase integrals', Optics Communications **5**, 1-4

Kravtsov Yu.A. and Yu.I. Orlov, 1990, 'Geometrical optics of inhomogeneous media', Springer Verlag, Heidelberg

Kersley L., J.A.T. Heaton, S.E. Pryse and T.D. Raymund, 1993. 'Experimental ionospheric tomography with ionosonde input and Eiscat verification', Annales Geophysicae **11**, 1064-1074

Kunitake M., K. Ohtaka, T. Marayuma, M. Tokumaru, A. Morioka and S. Watanabe, 1995, 'Tomographic imaging of the ionosphere over Japan by the modified truncated SVD method', Annales Geophysicae **13**, 1303-1310

Kunitsyn V.E., and E.D. Tereshchenko, 1992, 'Radio tomography of the ionosphere', IEEE Antennas and Propagation Magazine **34**, 22-32. Also appeared in The Radioscientist **4**, 12-25

Kunitsyn V.E., E.S. Andreeva, E.D. Tereshchenko, B.Z. Khudukon and T. Nygrén, 1994, 'Investigations of the atmosphere by satellite radiotomography', International Journal of Imaging Systems and Technology **5**, 112-127

Kunitsyn V.E., E.D. Tereshchenko, E.S. Andreeva, B.Z. Khudukon and Y.A. Melnichenko, 1995, 'Radiotomographic investigations of ionospheric structures at auroral and middle latitudes', Annales Geophysicae **13**, 1242-1253

Kunitsyn V.E., E.S. Andreeva, A.Y. Popov and O.G. Razinkov, 1995, 'Methods and algorithms of ray radiotomography for ionospheric research', Annales Geophysicae **13**, 1263-1276

Leitinger R., 1974, 'Der Einfluß ionosphärischer Ausbreitungsfehler bei der geodätischen Anwendung von Navigationssatelliten', Kleinheubacher Berichte, 17, 321-332

Leitinger R., G. Schmidt und A. Tauriainen, 1975, 'An evaluation method combining the differential Doppler measurements from two stations that enables the calculation of the electron content of the ionosphere', Journal of Geophysics **41**, 201-213

Leitinger R. and E. Putz, 1978, 'Die Auswertung von Differenz-Doppler-Messungen an den Signalen von Navigationssatelliten', Technischer Bericht, Institut für Meteorologie und Geophysik der Universität Graz

Leitinger R., G.K. Hartmann, 1983, 'Entfernungsfehler bei geodätischen Meßsystemen aufgrund von Atmosphäreneinflüssen bei Signalfrequenzen größer als 100 MHz. Teil II: Einfluß der Ionosphäre', Kleinheubacher Berichte **26**, 129-137

Leitinger R., G.K. Hartmann, F.-J. Lohmar and E. Putz, 1984, 'Electron content measurements with geodetic Doppler receivers', Radio Science **19**, 789-797

Leitinger R., 1994, 'Data from orbiting navigation satellites for tomographic reconstruction', International Journal of Imaging Systems and Technology **5**, 86-96

Lewitt R.M., 1983, 'Reconstruction algorithms: transform methods', Proceedings of the IEEE **71**, 390-408

Markkanen M., M Lehtinen, T. Nygrén, J. Pirttilä, P. Helenius, E. Vilenius, E.D. Tereshchenko and B.Z. Khudokon, 1995, 'Bayesian approach to satellite radiotomography with applications in the Scandinavian sector', Annales Geophysicae **13**, 1277-1287

Mawira A., 1990, 'Slant path 30 to 12.5 GHz copolar phase difference, first results from measurements using the Olympus satellite', Electronics Letters **26**, 1138-1139

de Mendonça F., 1962, 'Ionospheric electron content and variations measured by Doppler shifts in satellite transmissions', Journal of Geophysical Research **67**, 2315-2337

Menke W., 1989, 'Geophysical data analysis: discrete inverse theory', revised edition, Academic Press, London

Mitchell C.N., D.G. Jones, L. Kersley, S.E. Pryse and I.K. Walker, 1995, 'Imaging of field-aligned structures in the auroral ionosphere', Annales Geophysicae **13**, 1311-1319

Na H., J. Shen and H. Lee: 1995, 'A Fourier domain technique for ionospheric tomography', Radio Science **30**, 747-754

Newton R.R., 1967, 'The Navy Navigation Satellite System', Space Research VII, 735-763

Parlett B.N., 1980, 'The symmetric eigenvalue problem', Prentice-Hall, Englewood Cliffs

Phillips D.L., 1962, 'A technique for the numerical solution of certain integral equations of the first kind', Journal of the Association for Computing Machinery **9**, 84-97

Pryse S.E. and L. Kersley, 1992, 'A preliminary experimental test of ionospheric tomography', Journal of Atmospheric and Terrestrial Physics **54**, 1007-1012

Pryse S.E., L. Kersley, D.L. Rice, C.D. Russel, and I.K. Walker, 1993, 'Tomographic imaging of the ionospheric mid-latitude trough', Annales Geophysicae **11**, 144-149

Pryse S.E., C.N. Mitchell, J.A.T. Heaton and L. Kersley, 1995, 'Travelling ionospheric disturbances imaged by tomographic techniques', Annales Geophysicae **13**, 1325-1330

Ratcliffe, J.A., 1972, 'An introduction to the ionosphere and magnetosphere', Cambridge University Press

Rawer K., 1993, 'Wave propagation in the ionosphere', Kluwer Academic Publishers, Dordrecht

Raymund T.D., J.R. Austen, S.J. Franke, C.H. Liu, J.A. Klobuchar and J. Stalker, 1990, 'Application of computerized tomography to the investigation of ionospheric structures', Radio Science **25**, 771-789

Raymund T.D., 1992, 'A review of various techniques for computerized tomographic imaging of the ionosphere', AGARD Conference Proceedings 502, 14-1

Raymund T.D., S.E. Pryse, L. Kersley and J.A.T. Heaton, 1993, 'Tomographic reconstruction of ionospheric electron density with European incoherent scatter verification', Radio Science **28**, 811-817

Raymund T.D., S.J. Franke and K.C. Yeh, 1994a, 'Ionospheric tomography: its limitations and reconstruction methods', Journal of Atmospheric and Terrestrial Physics **56**, 637-657

Raymund T.D., 1994, 'Ionospheric tomography algorithms', International Journal of Imaging Systems and Technology **5**, 75-85

Raymund T.D., Y. Bresler, D.N. Anderson and R.E. Daniell, 1994b, 'Model assisted ionospheric tomography: a new algorithm', Radio Science **29**, 1493-1512

Raymund T.D., 1995, 'Comparisons of several ionospheric tomography algorithms', Annales Geophysicae **13**, 1254-1262

Rees M.H., 1989, 'Physics and chemistry of the upper atmosphere' Cambridge University Press

Rogers G.L. and W. Ireland, 1980, 'Ionospheric holography – I. The holographic interpretation of ionospheric data – II. The analysis of a set of ionospheric holograms', Journal of Atmospheric and Terrestrial Physics **42**, 385-396 and 397-406

Rohlfs K., 1986, 'Tools of radio astronomy', Springer, Berlin

Ross W.J., 1960, 'The determination of ionospheric electron content from satellite Doppler measurements 1. Method of analysis', Journal of Geophysical Research **65**, 2601-2615

Rothleitner W., R. Leitinger and G. Kirchengast, 1994, 'Using the Fourier domain for reconstruction in ionospheric tomography: a discussion', International Beacon Satellite Symposium July 11-15 1994, Aberystwyth, Proceedings, 56-59

Spakman W., 1993, 'Iterative strategies for non-linear travel time tomography using global earthquake data', in *Seismic tomography: theory and practice*, Chapman & Hall, London

Spoelstra T.A.Th. and H. Kelder, 1984, 'Effects produced by the ionosphere on radio interferometry', Radio Science **19**, 779-788

Spoelstra T.A.Th., 1991, 'Ionosphere and troposphere seen through a radio interferometer', AGARD Conference Proceedings 502, 16-1

Spoelstra T.A.Th., 1992, 'Combining TID observations: NNSS and radio interferometry data', Journal of Atmospheric and Terrestrial Physics **54**, 1185-1195

Spoelstra, T.A.Th., 1996, 'A climatology of quiet/disturbed ionospheric conditions from 22 years of Westerbork interferometer observations', Journal of Atmospheric and Terrestrial Physics **58**, 1229-1258

Seddon J.C., 1953, 'Propagation measurements in the ionosphere with the aid of rockets', Journal of Geophysical Research **58**, 323-335

Sutton E. and H. Na, 1994, 'Orthogonal decomposition framework for ionospheric tomography algorithms', International Journal of Imaging Systems and Technology **5**, 106-111

Tauriainen A., 1982, 'Application of wave field reconstruction of VHF radio waves to investigate single, isolated ionospheric irregularities', Radio Science **17**, 684-692

Terekhov A.I., 1992, 'Reconstruction of travelling ionospheric disturbances parameters by a tomographic method', Journal of Atmospheric and Terrestrial Physics **54**, 1295-1302

Tikhonov A.N., 1963, 'Solution of incorrectly formulated and the regularization method', Soviet Mathemathics Doklady **4**, 1035-1038

Turchin V.F., V.P. Kozlov, M.S. Malkevich, 1971, 'The use of mathemathical-statistics methods in the solution of incorrectly posed problems, Soviet Physics Uspekhi **13**, 681-703

van Velthoven P.F.J., 1990, 'Medium scale irregularities in the ionospheric electron content', Ph.D. thesis T.U. Eindhoven

Weekes K., 1958, 'On the interpretation of the Doppler effect from senders in an artifical satellite', Journal of Atmospheric and Terrestrial Physics **12**, 335-338

Weenink M.P.H., 1987, 'A new method for the calculation of the phase path in the geometrical-optics approximation', Manuscripta Geodaetica **12**, 99-103

Yeh K.C. and T.D. Raymund, 1991, 'Limitations of ionospheric imaging by tomography', Radio Science **26**, 1361-1380

Dankwoord

Mijn buitengewone dank gaat uit naar

→ KLM Aerocarto, KNMI, Rijkswaterstaat en de heer Husti van de Faculteit der Geodesie van de T.U. Delft

voor schenking en ter bruikleenstelling van de geodetische Doppler ontvangers

→ Bertus Hüsken, Herman de Groot, Eur van Andel, Jan Millenaar en de heren van het natuurkundepracticum

voor hun hulp bij het versleutelen van de ontvangers

→ Tineke Stroucken en Anton Stoorvogel

voor hun hulp bij de ontwikkeling van het algoritme

→ Léon Kamp, Titus Spoelstra en Frans Sluijter

voor de begeleiding

→ Christian Ingesson en Wouter van Aken

voor het lezen en corrigeren

→ Ypke Boersma en de heer Schlosser van het Noordzee College te Harlingen

voor de plaatsing van een ontvanger op zolder en een antenne op het dak

→ M. Cartigny, Directeur des services techniques de la Ville de Saint-Mihiel,

Michel, le chef du Théâtre Municipal de Bourg-en-Bresse et

Chris Korthals Altes, Ciprian Acatrinei et M. Douchy de la CNRS et de la Faculté des Sciences de Luminy à Marseille

pour leurs efforts et leur aide à l'installation des récepteurs

→ Brigit Toebes

voor haar steun en voor haar deelname aan de eerste tocht van de campagne

→ allen die ons hebben bijgestaan tijdens de fatale tweede tocht

→ Jan-Willem van Empel en Michiel van Aken

voor hun deelname aan de derde en laatste tocht van de campagne

STELLINGEN

behorende bij het proefschrift 'Tomography of the ionosphere'
van Gijs Fehmers
Eindhoven, 16 september 1996

1

Tomografische reconstructies van de electronendichtheid in de ionosfeer, die zijn gebaseerd op metingen van satellietsignalen door ontvangers op aarde, kunnen een globaal beeld geven van de electronenverdeling van de ionosfeer. Het zijn echter geen gedetailleerde en nauwkeurige afbeeldingen. Zo is de hoogte van de laag van maximale electronendichtheid binnen een nauwkeurigheid van ongeveer 90 km te bepalen.

Dit proefschrift, hoofdstuk 4.

2

Alle methoden om informatie over de ionosfeer uit differentiële-Dopplermetingen te halen, zijn gebaseerd op de veronderstelling dat de ionosfeer oneindig dun is. Tomografie is hierop de enige uitzondering.

Dit proefschrift, hoofdstukken 2 en 4.

3

Het feit dat de ionosfeer een gelaagd medium is, verergert het probleem van de ontbrekende horizontale lijnintegralen in tomografie van de ionosfeer.

Dit proefschrift, hoofdstuk 4.

4

Ondanks de beperkte nauwkeurigheid in de hoogtebepaling, tonen de resultaten van de meetcampagne een geloofwaardige dagelijkse variatie in de hoogte van de laag van maximale electronendichtheid.

Dit proefschrift, hoofdstuk 6.

5

Ons begrip van de natuur zou groter zijn, als materie en antimaterie toch in gelijke mate in het heelal aanwezig zijn. Daarom is het jammer dat een verbazingwekkend en postuum verschenen artikel zo weinig aandacht krijgt. Hierin postuleert de auteur kometen van antimaterie om twee bizarre gebeurtenissen in de aardse atmosfeer te verklaren.

K. Bullough, 1995, 'Interactions of antimatter with the atmosphere',
Journal of Atmospheric and Terrestrial Physics **57**, 1533-1551

6

Shannon definieert een entropie en bewijst dat deze een maat is voor de hoeveelheid informatie per symbool. Jaynes gebruikt dezelfde entropie-uitdrukking om een informatiedichtheid aan een kansverdeling toe te kennen, maar hier duidt een grote entropie juist op weinig informatie. Toch zijn de veronderstellingen achter beide formuleringen dezelfde en geven zij uitdrukking aan hetzelfde idee.

C.E. Shannon, 1948, 'A mathematical theory of communication',
Bell System Technical Journal **27**, 379-423 en 623-656

E.T. Jaynes, 1957, 'Information theory and statistical mechanics',
Physical Review **106**, 620-630

7

Het gebruik om onderzoekers te beoordelen op het aantal publicaties en op de score op de citatie-index, veroorzaakt een wildgroei van artikelen. Slechts de uitgevers varen hier wel bij.

8

Het is jammer dat veel vaderlandse natuurkundigen het deftige woord 'fysica' gebruiken, terwijl het Nederlandse woord 'natuurkunde' zo mooi en helder is.

9

Het broeikaseffect wordt slechts uitgesteld als we de olieconsumptie minderen. Vloeibare fossiele brandstoffen zijn zo handig, dat we ze waarschijnlijk sneller verbranden dan de natuur de vrijgekomen kooldioxide kan binden.

10

Toen ik aan de Technische Universiteit Eindhoven mijn werkzaamheden begon, was het een 'high-tech' universiteit; inmiddels werkt de TUE aan een 'duurzaam perspectief'. Toch heeft zij in de tussenliggende vier jaar miljoenen plastic koffiebekertjes naar de vuilstort verwezen. De TUE had haar energie beter kunnen steken in een alternatief voor deze verspilling dan in het lanceren van loze kreten.

11

Vakantiegangers die thuis vertellen dat die arme mensen zo gelukkig zijn met hun eenvoudige, maar zonnige leven in de schaduw van kokospalmen en bananebomen, zouden zich moeten afvragen waarom ze zelf, in hun overvloed, niet even gelukkig zijn.

12

Om de overlast door drugstoeristen in de grenssteden te verlichten, kunnen we onze buren het best bedienen vanuit de leegstaande douanehuisjes.

Intrigued by the stars and planets since his early youth, Gijs Fehmers (Amsterdam, 1966) decided to study astronomy. From 1985, he spent six years in Leiden, years that were as intellectually stimulating as they were exhilarating. In 1991, he finished his studies with a specialization in active galaxies.

In spite of his down-to-earth character, Gijs' scientific interests have not yet descended from the skies. In 1992, he started a PhD research on the ionosphere at Eindhoven University of Technology. Part of his work was the installation of five satellite receivers between Harlingen and Marseille. In the picture above, he is busy with an antenna on the roof of the Physics Department at the campus in Eindhoven. -B.T.